

ABSTRACT

Title of Dissertation: A Numerical Study of Vortical Structure in a Turbulent Backward Facing Step Flow

Eric Shaun Leonard, Doctor of Philosophy, 2018

Dissertation directed by: Professor Peter Bernard
Department of Mechanical Engineering

A vortex filament scheme, termed the *GVFS* or *gridfree vortex filament scheme*, in which the vorticity field away from the immediate vicinity of solid boundaries was represented by convecting, gridfree vortex tubes, was used to simulate flow over a backward-facing step with curved edges. The backward-facing step geometry, which possesses a fixed separation point at the step edge, is largely used to study the physics of separation, reattachment, recirculation, and reattachment. Changes to the vortex filament scheme, termed the *vortex insertion scheme*, were added to the original vortex filament scheme which consisted of inserting vortex tubes into the flow immediately downstream of the step edge based on local vorticity. Running the vortex filament scheme in conjunction with the vortex insertion scheme produced a sepa-

rated region suitable for comparison to flow over a backward-facing step with straight edges. By utilizing an alternative definition of structure which considered the entirety of the vorticity field it was demonstrated that roller vortices which form in the separated region: (i) result from the roll-up of fluid induced by the shear layer in the separated region, (ii) extend across the span but possess spanwise gaps which underlie the extensions of furrows which convect into the separated region, and (iii) break up due to shearing motions generated by the shear layer in the separated region. It was also discovered that flapping of the shear layer in the separated region results from changes in the spanwise positions of the furrows. The results of the present thesis demonstrate that vortex filament schemes are useful tools to tie together the structure in the upstream boundary layer of a step flow with the structure present in the mixing layer that occurs downstream of the step edge. In addition, a tentative connection was found between the structural make-up of the fluid upstream of the step edge and reattachment. This potential link was used to suggest an area for future research.

A Numerical Study of Vortical Structure in a Turbulent Backward Facing Step Flow

by

Eric Shaun Leonard

Dissertation submitted to the Faculty of the Graduate School of the
University of Maryland, College Park in partial fulfillment
of the requirements for the degree of
Doctor of Philosophy

2018

Advisory Committee:

Professor Peter Bernard, Chair
Professor James Baeder, Dean's Representative
Professor James Duncan
Professor Kenneth Kiger
Professor Johan Larsson

Contents

Abstract	1
Contents	ii
List of Tables	v
List of Figures	vi
List of Symbols	xiii
List of Acronyms	xiv
1 Introduction	1
1.1 Step Flow and Flow Separation	1
1.2 Alternative Ideas About Vortical Structure	5
2 Step Flow Basics	8
2.1 Basic Flow Regions	8
2.2 Notable Attributes of the Step Flow	10
2.3 Details of the Individual Flow Regions	17
2.3.1 Upstream Boundary Layer	17
2.3.2 Free Shear Layer	17
2.3.3 Reattachment Region	20
2.3.4 Primary Recirculation Region	21
2.3.5 Secondary Recirculation Region	22
2.3.6 Recovery Region	22
2.3.7 Distribution of Structure in the Step Flow	24
2.4 Short Summary of the Step Flow	25

3	Mixing Layers	27
3.1	Basic and Statistical Characteristics of Mixing Layers	27
3.2	Distribution of Structure in Mixing Layers	30
4	Zero Pressure Gradient Turbulent Boundary Layers	35
4.1	Statistical Characteristics of ZPGTBLs	35
4.2	Coherent Fluid Motions in ZPGTBLs	39
5	Operating Principles of the Gridfree Vortex Filament Scheme (GVFS)	46
5.1	Flat Plate Geometry Utilized by the GVFS	46
5.2	Explanation of the Finite Volume/Finite Difference Scheme Adjacent to Solid Boundaries	50
5.3	Kelvin's Circulation Theorem and Helmholtz's Vortex Theorems	63
5.4	Velocity Field Calculation Utilized by the GVFS	69
5.4.1	The Helmholtz Decomposition in an Infinite Domain	69
5.4.2	The Helmholtz Decomposition in a Domain with a Solid Boundary	71
5.4.3	The Helmholtz Decomposition in a Domain with a Solid Boundary Extended to Incompressible Flow	73
5.5	Vortex Stretching and Reorientation	74
5.6	GVFS Calculation of Velocity	85
5.7	Violation of the Divergence-Free Condition of the Vorticity Field at the Vortex Filament Endpoints	91
5.8	Vortex Loop Formation	91
5.9	Vortex Filament Removal in the GVFS	93
5.10	Some Advantages of Vortex Filament Methods	94
5.11	Rough Flowchart of the GVFS	94
6	Structural Aspects of Transitioning Boundary Layers	96
6.1	Vortex Furrows	96
7	Step Flow Simulation	102
7.1	Layout of the Step Geometry	102
7.2	Implementation of the Vortex Insertion Scheme	107
7.3	Analysis of the Vortex Insertion Scheme	125
7.4	Time Development of the Step Flow Simulation	134
7.4.1	State of the Fluid at Reattachment	135

8	Structural Analysis of the Step Flow Simulation	137
8.1	Structural Evolution of the Fluid Into the Separated Region	137
8.2	Reattachment	152
9	Summary and Conclusions	157
10	Suggestions for Future Work	159
10.1	Effect of the Curved Step Edge on the Flow Pattern in the Present Simulation	159
10.2	Area for Future Research Involving Reattachment	165
	Appendixes	167
A	Adverse Pressure Gradient Turbulent Boundary Layers	167
A.1	Equilibrium and Similarity in TBLs with Pressure Gradients	168
A.2	Statistical Characteristics of APGTBLs	169
A.3	Coherent Fluid Motions in APGTBLs	171
B	Basic Operating Principles of GPUs	172
	Bibliography	178

List of Tables

2.1	Order of Magnitude Estimates for Parameters Relevant to the Step Flow; $St = fh/U_\infty$ with f standing for frequency; vs - vortex shedding; slf - shear layer flapping; Re_h - Reynolds number based on step height; X_R - reattachment length; h - step height	26
-----	------------------------------------------------------------------------------------------------------------------------------------------------------------------------------------------------------------------------------------------------------------------------------------------	----

List of Figures

1.1	Rough schematic of flow over a backward facing step with straight edges. Note that there is a third, spanwise dimension into the page.	2
1.2	Flow with separation in an expanding channel. Adapted from Figure 9.6 on pg. 410 of [1].	4
1.3	Illustration of a region of rotational motion: (a) Illustration of a streamwise-oriented region of rotational motion as viewed in the x-y plane (b) Illustration of the same region of rotational motion as viewed from the y-z plane	7
2.1	Schematic of Flow Over a Backward-Facing Step: I, Incoming Boundary Layer; II, Primary Recirculation Region; III, Secondary Recirculation Bubble; IV, Free Shear Layer; V, Reattachment Region; VI, Formation of New Boundary Layer; VII, Remains of Upstream Boundary Layer; VIII, Free-Stream Region; IX, Recovery Region; h , Step Height; X_R , Reattachment Length; δ , Thickness of Incoming Boundary Layer at Step Edge. Based upon Figure 2 in [8].	9
2.2	Rough outline of mass flow over a backward-facing step. Based upon the arguments in [11].	11
2.3	Flow in and around the recirculation regions; ● is the low pressure center in the primary recirculation region	13
2.4	Illustration of mixing layer present in the step flow	15
2.5	Shedding from the upper step corner	18
2.6	Material Volume Analysis of the Primary Recirculation Region	19
3.1	Generation of a mixing layer. Based upon [57, 1, 31].	28
3.2	Rollers in a mixing layer.	31

3.3	Generation of a temporally evolving mixing layer as suggested by Rogers and Moser [58]	33
4.1	Breakdowns of a ZPGTBL into different wall-normal regions. Adpated from and based upon [31].	37
4.2	Illustration of low-speed streaks in a turbulent boundary layer	40
4.3	Illustration of a hairpin. Adapted from Figure 10 in [40]. . . .	42
4.4	Illustration of a hairpin packet lifting a low-speed streak	44
5.1	Schematic of flat-plate geometry: (a) Component Patches (b) Flat-plate geometry used by the GVFS	49
5.2	Wall-adjacent mesh used in the finite volume/finite difference scheme: (a) Triangles covering a flat plate surface (b) Triangle demarcated with green dots in (a) built up into a mesh that extends into the flow	52
5.3	Illustration of a triangular prism in the mesh. Velocity is calculated at the points labeled with + and vorticity is calculated at the point labeled with *. Copied from Figure 1 of [62]. . . .	53
5.4	Illustration of prisms used in the linear least square fit of vorticity for a side face. The face upon which the vorticity is calculated is demarcated with green dots. The arrow in the figure represents the direction of the velocity at the side. Adapted from Figure 2 of [62].	55
5.5	Convective and diffusive flux of vorticity siphoned off into a vortex tube (vortex tube in green)	59
5.6	(a) Vortex Line (b) Vortex Tube	65
5.7	Closed curve C which follows the fluid's velocity	67
5.8	Peak wavenumbers at which turbulent kinetic energy and turbulent kinetic energy dissipation reside. Based upon [31]. . . .	76
5.9	A small fluid line element with material endpoints	78
5.10	A small fluid line element and local vorticity vector oriented in the positive x_1 direction	82
5.11	Shearing motions caused by velocity variations in the x_1 direction turning Ω_1 : (a) U_2 velocity variation along the x_1 direction turning Ω_1 toward the x_2 direction (b) U_3 velocity variation along the x_1 direction turning Ω_1 toward the x_3 direction	84
5.12	A graphical representation of Eq. 5.98.	86

5.13	Velocity field (indicated by blue vectors) induced by an isolated vortex tube (in red)	87
5.14	Evolution of a vortex filament in time	89
5.15	Vortex loop: (a) Vortex filament composed of tubes in the shape of a loop. ● denotes vortex tube endpoints. Arrow denotes orientation of vorticity along the vortex loop (b) Two vortex tubes opposite one another in (a) with orientation of vorticity along each tube indicated	92
5.16	Rough flowchart for the GVFS. This flowchart covers the activities of the GVFS during one large time step Δt^*	95
6.1	Vortex furrows in a transitioning boundary layer on top of low-speed streaks. The solid, thinner lines are vortex filaments.	97
6.2	Vortex filaments in slices through a furrow in z-y planes at different streamwise locations at a fixed time (a) Towards the upstream end of a furrow (b) Between the upstream and downstream ends of a furrow (c) Towards the downstream end of a furrow	98
6.3	Identification of mushroom lobes	99
6.4	A pair of streamwise-oriented vortex filaments (in green) in a furrow inducing oppositely-rotating motion (described using dotted arrows) which forms the stem of a mushroom and lifts a low-speed streak (demarcated by a dotted line) away from the solid boundary.	100
7.1	Illustration of the step geometry (figures (b)-(e) display the surface grid the step flow simulation utilizes): (a) Drawing of the coordinate system used in the step flow simulation along with an approximate outline of the upper portion of the step (b) Side view of the step (c) Front view of the step looking downstream (d) Back view of the step looking upstream (e) View of the step at an angle which shows the vertical step wall	104
7.2	Illustration of the top half of the step along with its important dimensions and positioning	106
7.3	Display of the step surface grid at and around the curved step edges	108
7.4	2D illustration of the step mesh	109

7.5	Instantaneous, 2D streamlines in the plane $z = 0$ generated by the original version of the GVFS	110
7.6	Top half of the step along with an outline in green of relevant part of the mesh where the vortex insertion scheme applies . .	112
7.7	Instantaneous, 2D streamlines in the plane $z = 0$: (a) without the vortex insertion scheme (b) with the vortex insertion scheme (c) Mean streamlines in a DNS of flow over a backward-facing step with straight edges [13]	114
7.8	(a) Instantaneous isosurfaces of $\Omega_z = -55$ generated by the GVFS's simulation of the step flow with the vortex insertion scheme (b) Figure 7a from Silveira Neto et. al. [94] with isosurfaces of the magnitude of vorticity in blue, isosurfaces of streamwise vorticity at a positive level in yellow, and isosurfaces of streamwise vorticity at a negative level in green	116
7.9	(a) Instantaneous, 2D streamlines in the plane $z = 0$ with the red streamline marking the approximate reattaching streamline (b) Instantaneous contour plot of streamwise velocity in the plane $y = 0.03$ (lower plate lies at $y = 0.025$) at the same time as the plot in (a)	118
7.10	(a) Illustration of the <i>Ahmed</i> model, Figure 1a of Choi et. al. [133] (b) Separated flow over the <i>Ahmed</i> model, part of Figure 2b of Choi et. al. [133]	120
7.11	Ahmed models with straight or curved edges between the top plate and slanted plate, Figure 2 of Thacker et. al. [134] . . .	121
7.12	Flow past the two configurations illustrated in Figure 7.11 (Figure 7 of Thacker et. al. [134])	122
7.13	Contour plots of W in the planes: (a) $y = 0.026$ (b) $y = 0.076$	124
7.14	Instantaneous, 2D streamlines in the plane $z = 0$: (a) without the vortex insertion scheme (same plot as Figure 7.7a) (b) with the vortex insertion scheme (same plot as Figure 7.7b) .	125
7.15	Line plots of spanwise vorticity:  , $x = 2.425$, with vortex insertion scheme;  , $x = 2.425$, without vortex insertion scheme;  , $x = 2.45$, with vortex insertion scheme;  , $x = 2.45$, without vortex insertion scheme . .	126
7.16	Instantaneous, 2D streamlines from the plane $z = 0$ from the simulation with the vortex insertion scheme with the green line representing the pathline (flow from left to right) of a particle projected onto the $z = 0$ plane	127

7.17	Contour plot of spanwise vorticity in the plane $z = 0$: (a) without the vortex insertion scheme (b) with the vortex insertion scheme	129
7.18	Plot of tubes in the plane $z = 0$: (a) without the vortex insertion scheme (b) with the vortex insertion scheme	130
7.19	Contour plot of wall-normal velocity in the plane $z = 0$ from the simulation with the vortex insertion scheme	131
7.20	All plots in this figure taken from the simulation with the vortex insertion scheme: (a) Instantaneous, 3D streamlines emanating from points in the plane $z = 0$ (b) Contour plot of streamwise velocity in the plane $z = 0$ (c) Streamwise velocity line plot at $x = 2.43$ (d) Contour plot of streamwise velocity in the plane $x = 2.43$	133
7.21	(a) Time development of the step flow simulation:  , number of tubes (N_V);  , number of filaments (N_F) (b) View from overhead of the tubes in the upstream boundary layer which lie between $x = 1.2$ and $x = 2.4$ (the step edge is located at $x = 2.4$) at time $t = 5.44$	135
7.22	Contour plots of instantaneous C_f : (a) Upstream of the step edge (b) Downstream of the step edge	136
8.1	Isosurfaces of $\Omega_z = -55$ at time $t = 5.82$	138
8.2	Isosurfaces of $\Omega_z = -55$ along with plots of the vortex tubes from time $t = 5.82$ located within: (a) $z = -0.1275 \pm 0.005$ (b) $z = 0.0 \pm 0.005$ (c) $z = 0.125 \pm 0.005$	139
8.3	(a) Initial particle positions placed to approximately coincide with part of a roller vortex (b) Same particle positions as (a) along with the positions of those particles tracked backward in time, the particles in this figure are color-coded so that they are easier to keep track of and the dotted black line describes the approximate trend the particles display when they are tracked backward in time (c) Initial particle positions projected onto a contour plot of streamwise velocity, these particle positions are placed above the heart of the shear layer (d) Same particle positions as (c) along with the positions of those particles tracked backward in time, the particles in this figure are also color-coded	141

8.4	(a) Isosurfaces of spanwise vorticity revealing the presence of roller vortices (b) Same plot as (a), with the endpoints of vortex tubes which surround part of a roller vortex with gaps, plotted as particles (c) Plot of vortex tubes in a $z - y$ plane in the upstream boundary layer (d) Same plot as (c) with positions of a slice through the particles from (b) tracked backward in time superimposed	143
8.5	Isosurfaces of spanwise vorticity with vortex tubes above these isosurfaces superimposed	144
8.6	Contour plots of U at: (a) time t_1 in the plane $z = 0$ (b) time t_1 in the plane $y = 0.127$; $\cdots\cdots\cdots$ runs through $z = 0$ (c) later time t_2 in the plane $z = 0$ (d) time t_2 in the plane $y = 0.127$; $\cdots\cdots\cdots$ runs through $z = 0$	146
8.7	Demonstration of how the shear layer breaks up a roller vortex: (a) Particles covering part of a roller vortex (b)-(d) Subsequent evolution of the particles in (a) projected onto 2D streamlines and contour plots of streamwise velocity of nearby planes	148
8.8	Same plots as Figure 8.7 except that the particles in this figure cover a different part of the roller vortex than in Figure 8.7	149
8.9	Isosurfaces of $\Omega_z = -55$ (red), $\Omega_x = -30$ (blue), $\Omega_x = 30$ (yellow) in the separated region	151
8.10	Particles inserted into the flow in the vicinity of reattachment (the lower plate lies at $y = 0.025$) and advected backward in time and projected onto contour plots of streamwise velocity from $y=\text{constant}$ planes near to the particles; the particles are color-coded according to their spanwise positions in the first plot	153
8.11	All images in this figure taken from the same time as in Figure 8.10e, $t = 5.98$: (a) Contour plot of streamwise velocity in the plane $y = 0.175$ with the particles from Figure 8.10e which lie upstream of the step edge superimposed (b) Vortex tubes from the plane $x = 2.35$ (c) Contour plot of streamwise velocity in the plane $x = 2.35$ with the same particles from (a) superimposed (d) Contour plot of spanwise vorticity in the plane $x = 2.35$; $\cdots\cdots\cdots$ connects the $y=\text{constant}$ plane in (a) with the $x=\text{constant}$ planes in (b), (c), (d)	156

10.1	All plots taken from time $t = 6.46$: (a) 2D streamlines from the plane $z = 0$ with the approximate reattaching streamline highlighted in red which emanates from a wall-normal height in the upstream boundary layer of $y = 0.161$ (b) Contour plot of streamwise velocity in the plane $y = 0.161$ (c) Contour plot of streamwise velocity from the plane $y = 0.1275$. . .	160
10.2	(a) Contour plot of streamwise velocity at time $t = 6.46$ in the plane $y = 0.03$ with a line of particles superimposed at $x = 2.7$, $y = 0.03$ (b) Result of tracking the particles in (a) backward in time to $t = 6.02$ (c) Contour plot of streamwise velocity in the plane $y = 0.1763$ at time $t = 6.02$ with the particles from (b) which tracked back upstream of the step edge superimposed	162
10.3	(a) 2D streamlines from the plane $z = 0$ with the approximate reattaching streamline highlighted in red (same plot as Figure 10.1a) (b) Mean streamlines in a DNS of flow over a backward-facing step with straight edges [13] (same plot as Figure 7.7c)	164
10.4	Schematic of what a possible connection between the low-speed streaks in the upstream boundary layer and reattachment might look like in a flow over a backward-facing step with straight edges	166
B.1	Sample GPU grid containing two blocks where each block contains two threads	173
B.2	Visualization of the data transfer process between the computer memory and the GPU utilized by the earlier versions of CUDA. The steps in this process are numbered 1.) - 4.) . . .	175
B.3	Allocation and operations on an array, A, in unified memory. Changes to A on the GPU are automatically updated on the computer's memory and vice versa.	177

List of Symbols

Roman Letters:

h	Step Height
\mathbf{U}	Fluid Velocity Vector
U	Streamwise Component of Velocity
V	Wall-Normal Component of Velocity
W	Spanwise Component of Velocity
X_R	Reattachment Length
C_f	Skin Friction Coefficient
x	Streamwise Coordinate
y	Wall-Normal Coordinate
z	Spanwise Coordinate
Re_h	Reynolds number based on step height
Re_θ	Reynolds number based on momentum thickness
U_∞	Free-Stream Velocity
L	Length Scale

Greek Letters:

δ	Boundary Layer Thickness
$\mathbf{\Omega}$	Fluid Vorticity Vector
Ω_x	Streamwise Component of Vorticity
Ω_y	Wall-Normal Component of Vorticity
Ω_z	Spanwise Component of Vorticity
θ	Momentum Thickness
ν	Kinematic Viscosity

List of Acronyms

TBL	Turbulent Boundary Layer
APGTBL	Adverse-Pressure Gradient Turbulent Boundary Layer
ZPGTBL	Zero-Pressure Gradient Turbulent Boundary Layer
GVFS	Gridfree Vortex Filament Scheme

Chapter 1

Introduction

1.1 Step Flow and Flow Separation

The step flow geometry, displayed in Figure 1.1, is largely an artificial tool used to study flow separation, reattachment, recirculation, and redevelopment. The step geometry pictured in Figure 1.1 has straight edges, which is the traditional arrangement for the step flows examined in most of the literature [13, 94, 8, 14, 25]. The step geometry utilized in this thesis (discussed more thoroughly in Chapter 7) possesses rounded edges. Although this difference in arrangements of the step produces a shorter reattachment length for the step with rounded edges, it will be seen in Chapter 7 that flow over a step with rounded edges still produces similar vortical dynamics to flow over a step with straight edges in key regions of the flow pattern. With this in mind, the present chapter and Chapter 2 describe and review flow over a backward-facing step with straight edges, while Chapters 7 and 8 describe the results generated from the simulation used in this thesis, i.e. flow over a backward-facing step with rounded edges.

Although the step flow is largely an artificial tool, it is worth noting that the step flow does appear in engineering applications, including flow over weirs [6]. By examining the geometry of flow over buildings one can imagine that flow over a backward-facing step is relevant to this configuration as well [7]. In addition, a number of researchers have performed experiments [78, 82] or simulations [84] on the step flow in which the fluid was affected by external means at the upper step edge where separation occurs. One can imagine that these results could be put towards efforts to control certain

aspects of separation and/or reattachment. It also noteworthy that the step flow has been used to test turbulence models [89, 90, 91, 92, 93].

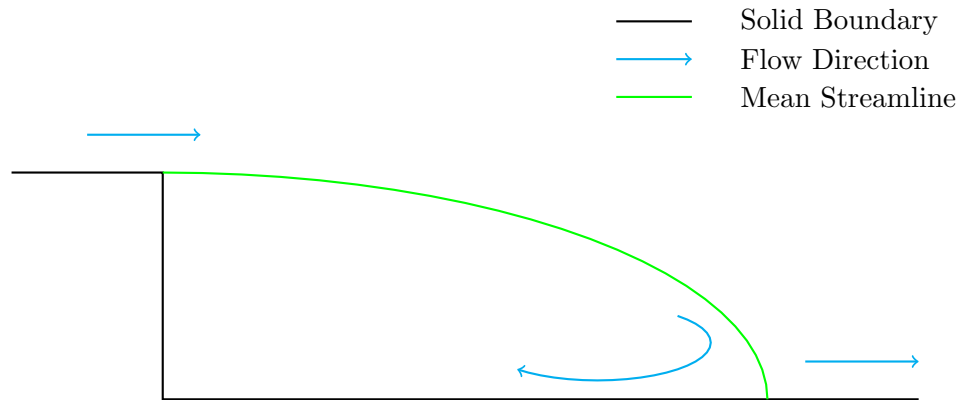


Figure 1.1: Rough schematic of flow over a backward facing step with straight edges. Note that there is a third, spanwise dimension into the page.

Flow separation, in turn, is an important dynamical behavior exhibited by fluid flowing in a number of different configurations, including flow over airfoils [2], flow in diverging pipes [3], air flow in the throat [4], and flow around turbines [5]. The phenomenon of flow separation often occurs when fluid flowing over a solid boundary is forced to separate from the solid boundary due the retarding effects of viscous forces and adverse pressure gradients. One can imagine fluid flowing over a solid boundary such that it is subject to an adverse pressure gradient. For example, the adverse pressure gradient could be due to flow in an expanding channel or around a curved object. Figure 1.2 displays flow in an expanding channel.

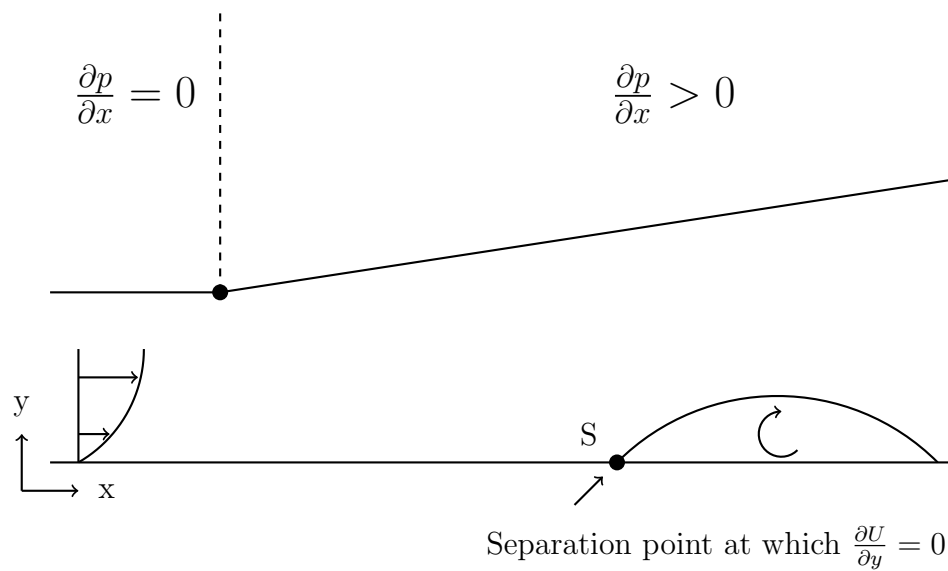


Figure 1.2: Flow with separation in an expanding channel. Adapted from Figure 9.6 on pg. 410 of [1].

In Figure 1.2, as the flow progresses through the expanding part of the channel it is subject to an adverse pressure gradient which reduces its momentum. At a certain streamwise distance the fluid will have slowed to such a degree that the layer of fluid immediately adjacent to the solid surface will be brought to a standstill, yielding $\frac{\partial U}{\partial y} = 0$, and forcing this parcel of fluid off of the solid boundary. This is the separation point S . The separated fluid will at some point reattach to the solid boundary and create a reverse flow region.

Studying flow separation through the use of a geometry in which the separation point is known (this occurs at the edge of the step in the step flow geometry) helps to simplify the analysis of this phenomenon because the separation point is clearly defined, thereby providing a firm framework in which to study separation.

The objectives of the present thesis are to use a vortex filament scheme to highlight novel insights into the vortical dynamics in the separated region of the step flow and discuss the reattachment of the fluid to the lower plate of the step geometry. Before reviewing the step flow in further detail, the next section discusses some alternative ideas about vortical structure.

1.2 Alternative Ideas About Vortical Structure

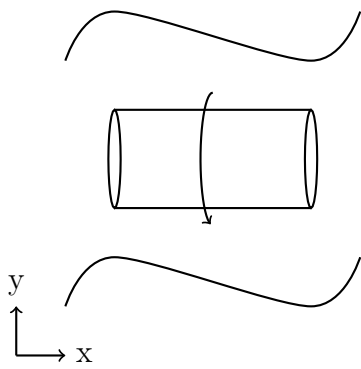
An important thrust of turbulence research concerns its structural makeup. Adrian [37] describes coherent structures as fluid motions that exist for long times (temporal coherence) and exhibit spatial coherence. These coherent structures can be considered to be vortices [98], and vortices, in turn, are usually associated with regions of approximately circular or spiraled streamlines when viewed in an appropriate reference frame [99, 100], although it is noteworthy that there are different ways of illuminating vortices in a moving fluid based on different definitions [98, 101]. In addition, the traditional idea of structure can encompass more than just the traditional idea of a vortex to include fluid motions such as low-speed streaks [38] (Chapter 4 will talk more about low-speed streaks).

In this thesis, the traditional view of what constitute coherent structures and vortices will not hold. Instead, *vortices*, *structure*, and *vortical structure*, terms which will be considered to be largely synonymous in this thesis, are

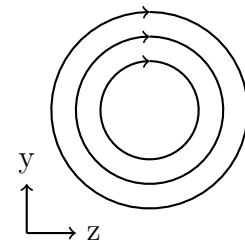
identified by considering the entire vorticity field, not just that part of the vorticity field responsible for regions of rotational motion [63]. For instance, spanwise-oriented vorticity created at the plate in a boundary layer might not generate rotational motion, but still contribute to the dynamics of the fluid nonetheless [63].

In this thesis, the traditional idea of a vortex will be referred to as a *region of rotational motion* [63]. Figure 1.3 illustrates a streamwise-oriented region of rotational motion as viewed in both the $x - y$ and $y - z$ planes.

The subsequent chapters in this thesis, Chapters 2-4, covering the step flow, mixing layers, and zero pressure gradient turbulent boundary layers (ZPGTBLs), will focus more on regions of rotational motion and traditional definitions of structure. The idea of *vortical structure*, as detailed by Bernard [63] and applied to the transitioning boundary layer [63], will be discussed further in Chapter 6. Then, in Chapter 8, this new definition of vortical structure will be utilized when examining the vortical content of the step flow.



(a)



(b)

Figure 1.3: Illustration of a region of rotational motion: (a) Illustration of a streamwise-oriented region of rotational motion as viewed in the x-y plane (b) Illustration of the same region of rotational motion as viewed from the y-z plane

Chapter 2

Step Flow Basics

Flow over a backward-facing step works primarily as follows: fluid flowing over a flat plate is subject to a sudden expansion (the step edge) which forces the fluid to separate from the solid surface and reattach further downstream. The reattached flow provides the fluid for a region of backflow upstream of reattachment [79] and the fluid for a recovery region downstream of reattachment in which the fluid recovers slowly towards a canonical flow over a flat plate¹. It is also important to note the effects of the pressure distribution in flow over a backward-facing step. The sudden expansion at the step edge leads to a significant adverse pressure gradient (APG) that extends from roughly three step heights downstream of the step edge, through reattachment, to roughly ten step heights downstream of the step edge [13]. In addition, Le, Moin, and Kim [13], in their paper, which utilized a DNS to compile various statistics about the step flow, attributed the momentum deficit seen in certain parts of the recovering boundary layer to the APG caused by the sudden expansion.

2.1 Basic Flow Regions

Flow over a backward-facing step can be broken down into different ‘regions’ and Figure 2.1 illustrates these regions along with a basic schematic of the

¹Although the flow over a backward-facing step is a three-dimensional geometry with a spanwise dimension, some researchers have simulated flow over a backward facing step with only two dimensions using direct numerical simulations [71] and vortex methods [72, 73, 74]

step flow.

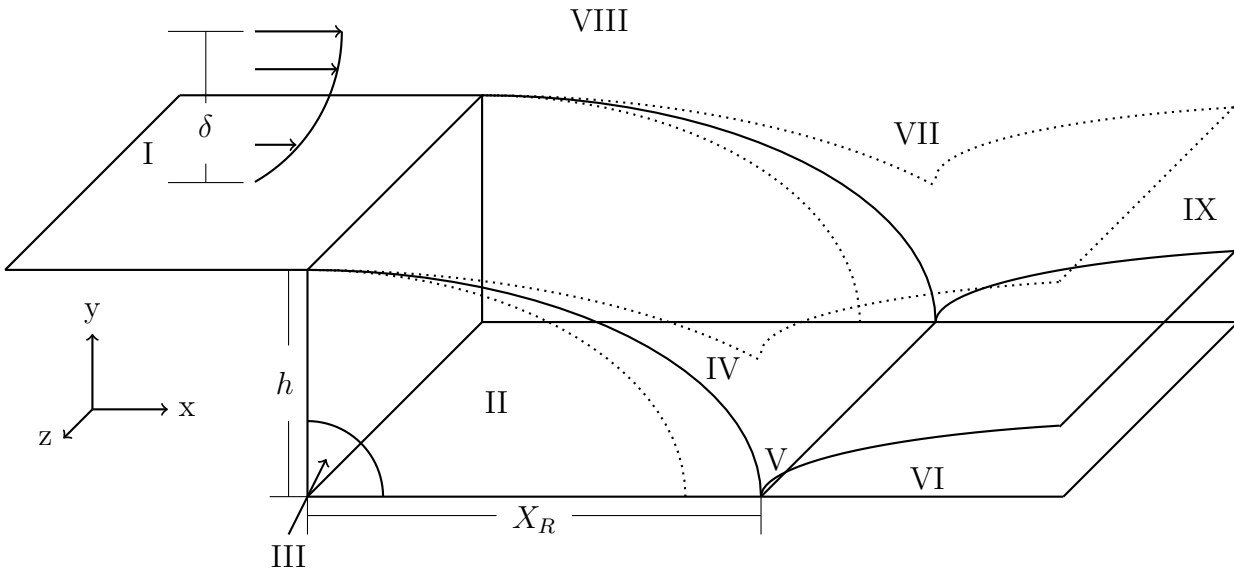


Figure 2.1: Schematic of Flow Over a Backward-Facing Step: I, Incoming Boundary Layer; II, Primary Recirculation Region; III, Secondary Recirculation Bubble; IV, Free Shear Layer; V, Reattachment Region; VI, Formation of New Boundary Layer; VII, Remains of Upstream Boundary Layer; VIII, Free-Stream Region; IX, Recovery Region; h , Step Height; X_R , Reattachment Length; δ , Thickness of Incoming Boundary Layer at Step Edge. Based upon Figure 2 in [8].

It is also noteworthy that many researchers who study the step flow do so with a geometry that includes a top wall where the fluid’s velocity goes to zero [77, 85, 106]. In this case, one can describe the flow geometry as a suddenly-expanded channel². Although the geometry is slightly different, the physics of flow in a suddenly-expanded channel is similar to that of flow without a top wall. In particular, flow in suddenly-expanded channels still exhibits reattachment [10, 80, 81, 86] and streamwise adverse pressure gradients [10, 80].

2.2 Notable Attributes of the Step Flow

This section seeks to describe the basic workings and statistical characteristics of flow over a backward facing step.

Huang and Fiedler [9] examined the initial developments of the step flow through experimental tests. In their experiments, the fluid in the channel was quiescent until a pump was turned on and the flow was allowed to evolve. These researchers found that a start-up concentration of vorticity existed in the recirculation region and then subsequently ceased to exist.

One can analyze the mass flow of the problem when the step flow reaches its final state (fully-formed recirculation region, reattachment region, recovery region, etc.). Spazzini, Iuso, Onorato, Zurlo, and Di Cicca [11] detailed the mass flow over a backward-facing step and Figure 2.2 provides a rough outline of their arguments.

²In this chapter, the term ‘backward-facing step flow’ will be used at times to refer to flow with a top wall and at times to refer to flow without a top wall, while the term ‘suddenly-expanded channel’ will be used to refer only to flow with a top wall.

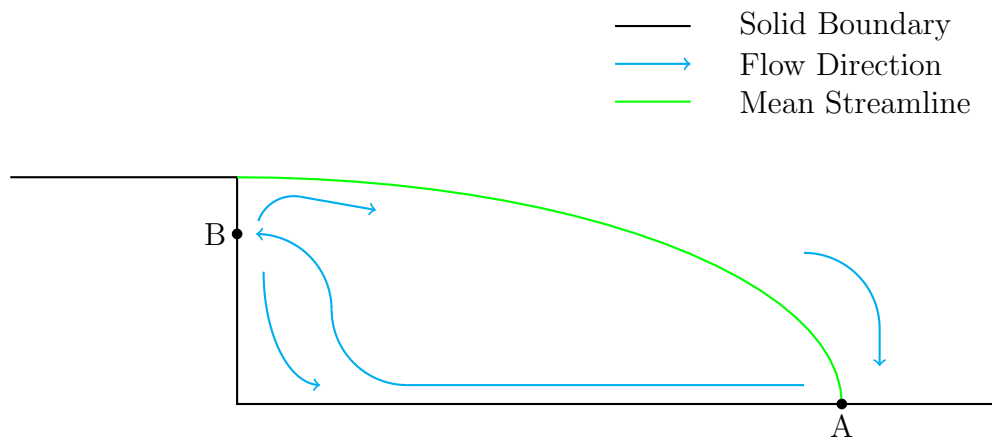


Figure 2.2: Rough outline of mass flow over a backward-facing step. Based upon the arguments in [11].

According to the arguments described in Spazzini et. al., the fluid touching down at reattachment provides fluid for the primary recirculation region (point A in Figure 2.2), with upstream motion induced by the adverse pressure gradient [15]. Once the upstream-moving fluid hits the vertical step wall it splits (point B), with part of this fluid forming the secondary recirculation region and part of this fluid moving upwards to be entrained by the free shear layer. The upstream-moving fluid does not reach all the way to the lower step corner due to inertial effects [12].

Another significant pressure effect which occurs in flow over a backward-facing step is the downward curvature of the free shear layer caused by the low pressure region at the center of the primary recirculation region [12]. This low pressure center and circulating fluid patterns are illustrated in Figure 2.3.

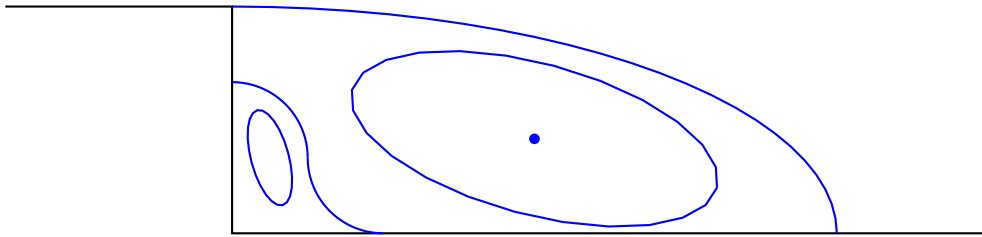


Figure 2.3: Flow in and around the recirculation regions; ● is the low pressure center in the primary recirculation region

It is also noteworthy that part of the free shear layer continues into the recovery region, spreading into the vestiges of the top part of the boundary layer generated upstream of the step edge. An additional component of the recovery region is the new boundary layer that begins to develop at the wall downstream of reattachment [8]. And throughout the entire flow domain, there is a free-stream with uniform velocity above the part of the flow consisting of velocity gradients.

The streamwise mean velocities in flow over a backward-facing step exhibit certain characteristics. In particular, backflow is evident in the primary recirculation region and there is a persistent velocity deficit below the log law in the recovery region downstream of reattachment [13], although the fluid adjacent to the solid boundary recovers more quickly to that of a zero pressure gradient turbulent boundary layer (ZPGTBL) [14]. In addition, the u_{rms} and v_{rms} turbulent velocity wall-normal profiles, as well as the Reynolds shear stress wall-normal profile ($-\overline{u'v'}$), tend to peak before the step edge in the recirculation and reattachment regions [13].

The skin friction upon the lower step wall changes sign roughly on the boundary between regions with different flow directions (e.g. at reattachment and between the primary and secondary recirculation regions). In addition, the skin friction increases after reattachment and appears to asymptote to a final value [13].

Another important aspect of the step flow is the similarity that flow downstream of the step edge bears to a mixing layer [15, 94], given that the relatively lower-speed fluid of the clockwise-rotating recirculation region borders the relatively higher-speed fluid of the free shear layer emanating off of the step edge. Figure 2.4 illustrates this configuration. In addition, roller vortices develop in the fluid which separates from the step and moves out over the step edge [94].

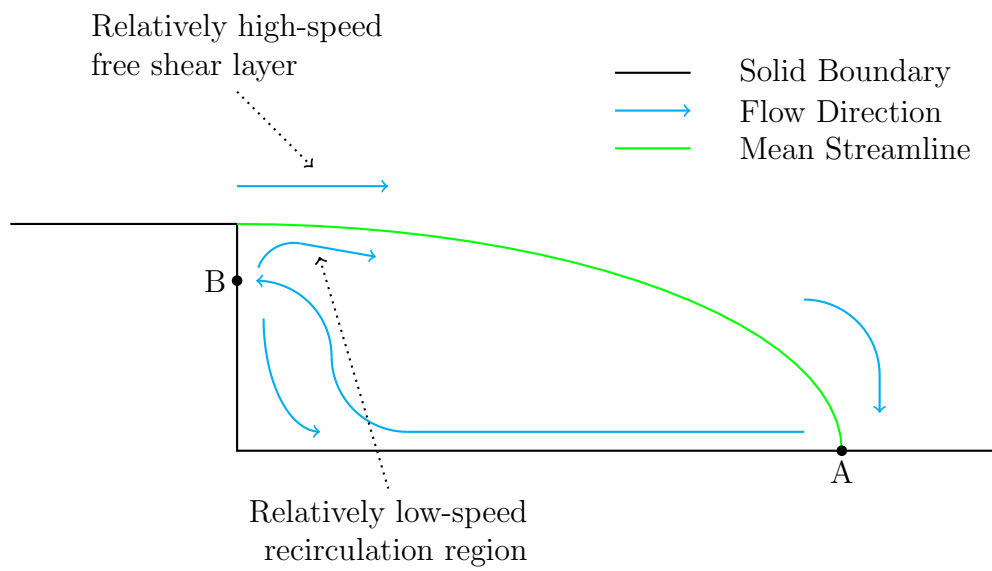


Figure 2.4: Illustration of mixing layer present in the step flow

Eaton [15] asserted that “the reattaching shear layer is indeed very similar to a plane-mixing layer upstream of the reattachment zone.” And Bradshaw and Wong [8] maintained that for geometries in which $h/\delta \gg 1$, the fluid separating from the step edge transitions immediately to a fully-developed mixing layer. It is noteworthy that Eaton asserted that the free shear layer cannot achieve a fully-developed state prior to reattachment. Bradshaw and Wong also maintained that the shear layer transitions back to a boundary layer after reattachment.

It is worth noting that investigations of the stability of the step flow and/or its transition to turbulence have been conducted [87, 20]. Barkley, Gomes, and Henderson [20] investigated flow in a suddenly-expanded channel by utilizing a computational linear stability analysis. By adding perturbations oscillating sinusoidally in the spanwise directions to the base flow, these authors characterized the secondary flow occurring at the smallest Reynolds number-wavenumber perturbation where the flow becomes neutrally stable “as a flat roll lying within the primary recirculation zone.” These authors argued that the source of instability is due to an unfavorable gradient of the magnitude of angular momentum - moving out in the radial direction near the step edge, it is argued that the magnitude of angular momentum decreases. In this model, the combination of a “centrifugal instability” near the step edge and the step wall itself create a three-dimensional instability.

Another important aspect of the step flow which is relevant to its analysis concerns the different scales used to describe the dynamics of the fluid flowing over the step. A few important length scales include: the step height, h , the reattachment length, X_R , the boundary layer thickness at separation, δ , and the momentum thickness at separation, θ . An important velocity scale is the free-stream velocity, U_∞ , and an important pressure scale is $\frac{1}{2}\rho U_\infty^2$ [13]. Time scales can be formed through *Length Scale/Velocity Scale*, so that an important time scale is $\frac{h}{U_\infty}$ [13].

There are two Reynolds numbers of importance in flow over a backward facing step. The first is Re_θ , the Reynolds number based on free-stream velocity and momentum thickness at the step edge, which characterizes the state of the separating boundary layer. The second is Re_h , the Reynolds number based on the step height h and an upstream velocity (two possible choices for this upstream velocity are the free-stream velocity in flow without a top wall [13] or maximum upstream channel velocity for flow with a top wall [21]).

Nadge and Govardhan [21] summarized previous experiments (both phys-

ical and numerical) performed on the step in a table. One column of this table listed the Reynolds number based on step height, Re_h , at which these experiments were conducted. Based on this table, it is evident that a large range of Re_h numbers have been studied (this table lists Re_h numbers spanning at least one order of magnitude). Based on their own experiments of flow in a suddenly-expanded channel, Nadge and Govardhan concluded that once the separating boundary layer is turbulent or is close to turbulence the structure of the recirculation region (which includes mean streamlines and Reynolds stress contours) changes little with increases in Re_h .

Jovic and Driver [22], in an experimental study of flow over a backward-facing step, noted that the magnitude of the skin-friction coefficient decreases with increasing Reynolds number based on step height (however, judging from Nadge and Govardhan [21], this effect might be due to low Reynolds numbers).

2.3 Details of the Individual Flow Regions

This section seeks to provide more detailed descriptions about some of the flow regions outlined in Figure 2.1.

2.3.1 Upstream Boundary Layer

In step flow geometries without a top wall, the upstream boundary layer is a typical canonical flow over a flat plate. Different researchers have analyzed backward-facing step flow with different flow regimes existing at the step edge, that is, laminar [8], transitional [29], or turbulent [14] boundary layers at the step edge. And for the entire step flow when it is modeled without a top wall, there is a region on top of the flow areas where there are no velocity gradients where the fluid flows simply with the free-stream velocity, U_∞ .

2.3.2 Free Shear Layer

The free shear layer emanates from the step edge where the boundary layer separates. As mentioned previously, the free shear layer, along with the top part of the primary recirculation region, display characteristics similar to a mixing layer and roller vortices along with streamwise-oriented vortices have been observed in this region [94]. In addition, Le, Moin, and Kim [13] suggest

that vortices are shed from the step itself, an assertion based partly on the results contained in [102]. Figure 2.5 illustrates a possible visualization of shedding from the upper step corner.

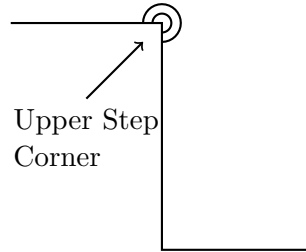


Figure 2.5: Shedding from the upper step corner

The results of previous researchers suggest that shedding of vortices from the upper step corner in the step flow is plausible. As noted by Williamson [119], Roshko [120] showed that the shedding of vortices occurs in turbulent flow around a circular cylinder. In addition, Bruno et. al. [121] hypothesized the existence of shedding of vortices from the trailing edge of turbulent flow around a rectangular cylinder and Okajima [122] presented evidence from experimental tests indicating the existence of shedding of vortices in flow over square cylinders. Whatever their origin, it is clear that spanwise-oriented vortices exist in the free shear layer emanating from the step edge [17, 16, 18, 19].

It is also noteworthy that the free shear layer entrains the recirculation region as it moves toward reattachment [15] and that part of the free shear layer continues into the recovery region [8].

In addition, “flapping” of the shear layer has been observed [18]. Driver et. al. [18] do not state outright, but mention that a small peak in one of their spectral plots might be due to shear layer flapping. This peak corresponds to a Strouhal number of 0.06, or $\frac{fb}{U_{sl}} = 0.06$, where f is the frequency of the shear layer flapping, b is the width of the shear layer or vorticity thickness, and U_{sl} is the shear layer velocity or the average of the top and bottom velocities of the shear layer. Le, Moin, and Kim [13] reported that the reattachment length in their simulation oscillated up- and downstream with a Strouhal number based on free-stream velocity and step height, $St = fh/U_\infty = 0.06$. Le, Moin, and Kim also found a peak in frequency of the streamwise and wall-normal velocity at a dimensionless Strouhal number of $St = fh/U_\infty = 0.06$

at different points in the step flow. Based on these numbers, one may surmise that the flapping of the shear layer occurs at a Strouhal number on the order of 0.06, although there is not a universal consensus as to the validity of this number [11]. In addition, it is worthwhile to point out that the shedding of vortices in the shear layer occurs at a frequency about one order of magnitude greater than that of the flapping of the shear layer [11].

In addition, there isn't a universal consensus as to the cause of shear layer flapping, but explanations have been provided [11]. After reading Eaton [15], Eaton and Johnston [26], Driver et. al. [18], and Spazzini et. al. [11] one can surmise a possible explanation as to the cause of shear layer flapping. According to this explanation, the flapping of the shear layer is due to an instantaneous mass flow/material volume imbalance in the primary recirculation region. Figure 2.6 displays the instantaneous position of a material volume, denoted by MV, surrounding fluid in the recirculation region (a material volume is taken to be a region space that adjusts so as to encompass a fixed mass of fluid [33]), along with the mean recirculation bubble.

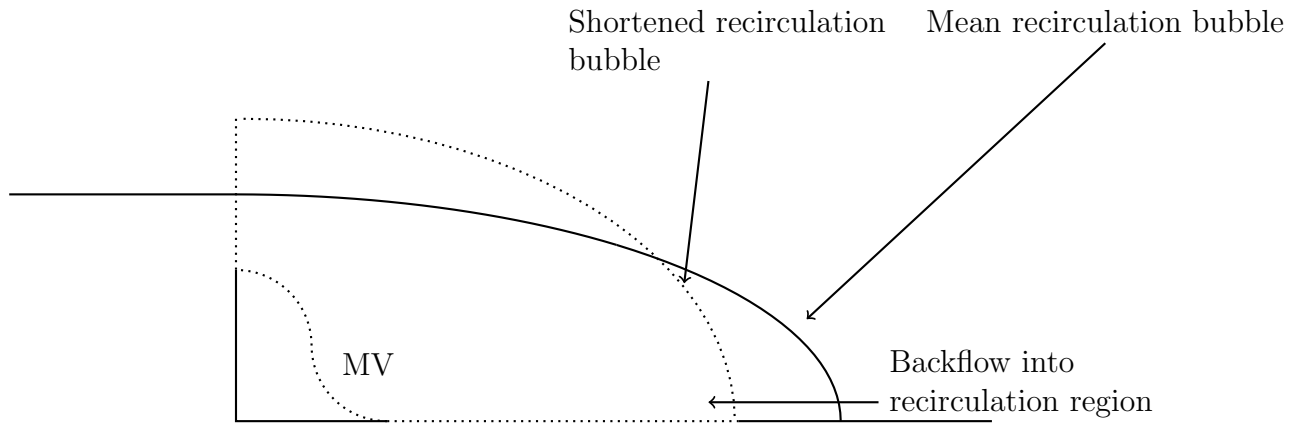


Figure 2.6: Material Volume Analysis of the Primary Recirculation Region

For incompressible flow, conservation of mass holds that for a material volume V [33]:

$$\frac{dV}{dt} = 0 \quad (2.1)$$

When the instantaneous reattachment length is shorter than the mean reattachment length (which could potentially be due to the shear layer entrainment rate) as in Figure 2.6, the recirculation bubble is smaller in the streamwise direction along the lower step wall, shrinking V . But because $\frac{dV}{dt}$ must equal zero, to compensate for this effect the fluid in the recirculation region expands in the wall-normal direction along the side-wall, pushing the free shear layer upwards. The opposite happens when the instantaneous reattachment length is greater than the mean reattachment length so that the free shear layer moves downward in this case. Therefore, according to the argument just presented, the expanding and shrinking motions of the recirculation region near reattachment are responsible for the flapping of the shear layer.

2.3.3 Reattachment Region

The reattachment region encloses the area in which the shear layer reattaches to the lower step wall. Reattachment occurs as a result of entrainment of the primary recirculation region and wall-normal pressure gradients [15]. One way to measure the reattachment point is to determine the location where the mean wall shear stress goes to zero [13]. Another way to measure the reattachment point is to determine where the mean streamline which emanates off of the step edge reattaches to the lower step wall [83]. One way to estimate the bounds of the reattachment region is to examine a plot of the percentage of time the fluid adjacent to the lower step wall has a positive mean streamwise velocity versus streamwise distance [23]. At reattachment, part of the shear layer moves upstream to provide the fluid for the recirculation region [11] and part of the shear layer continues downstream into the recovery region [8]. It is also noteworthy that the reattachment point oscillates upstream and downstream in time with a Strouhal number based on the maximum mean inlet velocity and step height of approximately 0.06 [13]. Le, Moin, and Kim [13], in their direct numerical simulation of the step flow, offer an explanation as to why the reattachment length oscillates. According to their argument, increases in the reattachment length are due to the appearance and subsequent growth of structures past the step edge.

As a structure passes through the reattachment region, according to this argument, the reattachment length abruptly decreases.

From a review of the literature, it seems that the development of the turbulence in the reattachment region is not a completely settled matter. Eaton [15] asserted that the turbulence often decreases near the reattachment region in two stages, with the first stage occurring approximately $1.5h$ upstream of reattachment and the second stage occurring slightly downstream of reattachment. It is noteworthy that Yoo and Baik [29] found that the Reynolds stresses started to decrease just before reattachment. Eaton mentions that the first stage could be due to the stabilizing effects of mean streamline curvature [24]. But Le, Moin, and Kim [13], in their numerical simulation, do not observe a prominent decrease of the turbulent fluctuating velocities close to reattachment. Another unresolved aspect of the reattachment region concerns its vortical dynamics. Bradshaw and Wong [8] supported the idea that the shear layer and eddies split at reattachment while Kim, Kline, and Johnston [14] cast doubt upon the proposition that splitting of the eddies is the sole behavior that occurs at reattachment, instead providing evidence to possibly support the idea that the eddies in the shear layer alternate between moving off in the upstream direction and moving off in the downstream direction at reattachment. Chandrsuda and Bradshaw [25], however, argued against the hypothesis of alternating eddies at reattachment.

2.3.4 Primary Recirculation Region

The mass flow for the primary recirculation region is provided by the shear layer at reattachment [11], while the primary recirculation region's inertia prevents it from moving all the way into the lower step corner, paving the way for the secondary recirculation region [12]. The fluid in the primary recirculation region rotates in the clockwise direction [95]. Some researchers have noted that the recirculation region may be closer to a laminar flow [22, 27]. Although the turbulent fluctuations may be significant in the recirculation region, the correlation between streamwise and wall-normal turbulent velocity fluctuations may not exist as it does in wall-influenced turbulence [27]. In fact, prior to reattachment the turbulent transport term in the turbulent kinetic energy equation transports turbulent kinetic energy downward from the free shear layer to the primary recirculation region [13]. In addition, the primary recirculation region possesses a large degree of three-dimensionality [76].

2.3.5 Secondary Recirculation Region

The secondary recirculation region is formed because the fluid moving upstream in the primary recirculation region cannot reach the lower step corner due to its own inertia [12]. Consequently, the fluid in the secondary recirculation region rotates in the counterclockwise direction [12, 95]. The secondary recirculation region has a well-defined center [12] and spans the step [13]. A plot of mean streamlines presented in Le, Moin, and Kim [13] reveals that the secondary recirculation region covers 80% of the step height in the wall-normal direction. Le, Moin, and Kim [13] reported the existence of a third, smaller recirculation region in the lower step corner of their direct numerical simulation, although Hall et. al. [12], in their experimental study, did not find this third recirculation region. It is noteworthy that analytical arguments predict the existence of a third recirculation region [28].

2.3.6 Recovery Region

The recovery region consists of the area downstream of the reattachment region. In this region the shear layer, after it has reattached to the lower step wall, begins to recover back towards a canonical turbulent boundary layer over a flat plate. This suggests that, if one were to analyze the recovery region, it would be helpful to be familiar with the characteristics of ZPG (zero pressure gradient) TBLs (turbulent boundary layers) in order to compare the recovery region to ZPGTBLs at various streamwise distances. It is also important to note that there is an adverse pressure gradient that occurs through the reattachment point [13] and downstream of the reattachment point [14, 29] and so it is also important to be familiar with the characteristics of APG (adverse pressure gradient) TBLs to see if the TBL in the recovery region bears similarities to APGTBLs.

One way to think of the recovery region was suggested by Bradshaw and Wong [8]. According to these researchers, the recovery region can be thought of as a mixing layer (consisting of the free shear layer and primary recirculation region) ‘transforming’ back into an ordinary TBL. In fact, Yoo and Baik [29] state, “In the redeveloping boundary layer after reattachment, the flow near the wall displays the characteristics of the boundary layer while the flow away from the wall displays the characteristics of the mixing layer developed in the separated flow region.” In addition, it is important to recognize that a new boundary layer is formed downstream of reattachment

[8] as a result of the fluid’s interaction with the lower step wall and that the reattached shear layer spreads into the vestiges of the boundary layer (generated upstream of the step edge) downstream of reattachment [8] (see Figure 2.1).

Perhaps the most significant feature of the recovery region is that the velocity profile in wall coordinates displays a deficit relative to ZPGTBLs in the log region for many step heights downstream of reattachment [13]. In the direct numerical simulation of Le, Moin, and Kim [13] the velocity profile had not fully recovered to the log law even 20 step heights downstream of the step edge, with mean reattachment occurring at 6.28 step heights downstream of the step edge. Le, Moin, and Kim [13] attribute this velocity deficit partly to the effects of the APG caused by the sudden expansion at the step edge. But, the velocity of the fluid closer to the lower step wall in the recovery region requires a shorter distance to recover than does the velocity of the fluid further from the wall [14, 29]. According to Kim, Kline, and Johnston [14], this discrepancy decreases $\frac{\partial \bar{U}}{\partial y}$ above $y^+ \approx 100$, which then decreases the mean streamwise velocity below the log law. Kim, Kline, and Johnston took this to mean that the fluid is not in local equilibrium in this region and these researchers suggested that the wall shear velocity $U_\tau = (\tau_w/\rho)^{1/2}$, where τ_w is the wall shear stress and ρ the fluid density, might not be the best velocity scale to use throughout the entirety of the region near the wall.

Kim, Kline, and Johnston also observed in their experiments that the maximum turbulent intensities and Reynolds shear stress for a given streamwise location decrease in a significant fashion downstream of reattachment. This trend, in general, seems to be confirmed by the simulations of Le, Moin, and Kim. In addition, Kim, Kline, and Johnston displayed data for profiles of intermittency at two streamwise distances downstream of reattachment and compared these results to intermittency profiles for a mixing layer and a boundary layer. For the most part, the intermittency profiles of the step flow lay between that of the mixing layer and boundary layer. Based on analysis of this data, Kim, Kline, and Johnston concluded that the fluid in the recovery region transitions from mixing layer to boundary layer, but that full recovery takes a long streamwise distance.

Yoo and Baik [29] conducted an experimental investigation of the recovery region of flow over a backward-facing step. Their paper contained a number of noteworthy conclusions. In their experiments, the boundary layer was transitional at the step edge, but turbulent at reattachment. These re-

searchers noted that, in addition to the velocity deficit in the log region, there is a velocity deficit in the outer region which takes a long distance to recover. In addition, these researchers noted that the Clauser parameter does not asymptote to the value of the Clauser parameter in a regular TBL. It is noteworthy that Bradshaw and Wong's [8] results at the last downstream distance measured show a value for the Clauser parameter that is below that of a regular TBL. Yoo and Baik also noted that the Clauser parameter, although it does not asymptote to the value for a regular TBL, does reach a constant value. Yoo and Baik take this to mean "that the ratio of the pressure force in the boundary layer to the friction force on the wall is constant and that a balance is maintained between these two forces."

Yoo and Baik also observed that eventually the Reynolds shear stress distribution in the recovery region reaches a point at which it decreases monotonically from the lower step wall going out in the wall-normal direction. This distribution occurs in equilibrium ZPG TBLs [29]. In addition, Yoo and Baik noted that intermittency profiles in the recovery region begin close to that of a mixing layer and then approach that of a boundary layer 50 step heights downstream of the step edge. In addition, these researchers noted that the distribution of turbulent kinetic energy in the initial stages of the recovery region/edge of the reattachment region bears similarities to that of a mixing layer, but by 50 step heights downstream of the step edge the distribution of turbulent kinetic energy is similar to that of an equilibrium TBL. They also found that the Reynolds shear stress distribution 50 step heights downstream of the step edge is close to that of an equilibrium turbulent boundary layer.

2.3.7 Distribution of Structure in the Step Flow

This section describes the makeup of the step flow when analyzed in terms of its structural composition as detailed by the work of other researchers. Scarano, Benocci, and Riethmuller [96] investigated the structures in flow over a backward-facing step. These researchers identified the positions and sizes of the structures obtained from experimental investigations of the step flow. The results of these researchers displayed a general trend in which relatively smaller structures more densely populated the step flow downstream of the step edge than did relatively larger structures. Their results also indicated that the step flow is populated by structures in the free shear layer and reattachment region, but much less so in the recirculation regions, although these researchers found the lower step corner to contain some structures

which mostly possessed positive spanwise vorticity. Schram, Rambaud, and Riethmuller [97] utilized a different technique to elucidate the distribution of structures in their step flow experiments. Based on their results, one can observe that the free shear layer is densely populated with structures, and that the density of the structures in the step flow tends to decrease as one moves downstream into the reattachment region. Their results also indicate that the recirculation regions are much less densely populated by structures than the other regions of the step flow.

Kostas, Soria, and Chong [83] also conducted experiments on the step flow. These researchers found that, in the free shear layer, the spanwise vorticity, which is negative, starts out as a narrow band near the step edge which spreads out in the wall-normal direction as the downstream distance from the step edge grows. In addition, they also found that the spanwise vorticity decreases in magnitude moving into the reattachment and recovery regions. Furthermore, these researchers found that positive spanwise vorticity existed in the secondary recirculation region. Kostas, Soria, and Chong also found evidence of vortex pairing in the free shear layer. In addition, Kostas, Soria, and Chong mention that their instantaneous experimental data “show the presence of relatively large-scale hairpin-like structures” past reattachment.

Yoo and Baik [29] conducted a spectral analysis of their step flow data. These researchers found that the one-dimensional energy spectra they generated in the recovery region displayed streamwise wavenumber ranges in the inertial subrange with approximately $-5/3$ slope when plotted in log-log form versus streamwise wavenumber.

It also worth noting that Le, Moin, and Kim [13], in their DNS of the step flow, did not observe full-blown near-wall low-speed streaks in the recovering boundary layer even 20 step heights downstream of the step edge, although they did observe neighboring contours of low- and high- streamwise velocity fluctuations stretched out in the streamwise direction which occurred towards the downstream edge of their computational domain (20 step heights past the step edge) in the recovery region.

2.4 Short Summary of the Step Flow

Some of the prominent features of the step flow include: a free shear layer emanating off of the step edge which touches down in the reattachment region, a primary recirculation region with fluid rotating in the clockwise direction, a

secondary recirculation region in the lower step corner with fluid rotating in the counterclockwise direction, and a recovering boundary layer which takes a long distance to return to a regular ZPGTBL.

Some other noteworthy aspects of the step flow include: a dense composition of structures in the free shear layer, and the lack of full-blown near-wall low-speed streaks well into the recovery region.

To close this chapter, Table 2.1 displays representative values for some relevant numerical parameters which describe the step flow. These numbers are largely meant to be order of magnitude estimates.

Parameter	Numerical Value	References
St_{vs}	0.6	[11, 13]
St_{slf}	0.06	[13]
Upper limit of Re_h seen in literature	1×10^5	[21, 25]
X_R/h	6.28	[13]

Table 2.1: Order of Magnitude Estimates for Parameters Relevant to the Step Flow; $St = fh/U_\infty$ with f standing for frequency; vs - vortex shedding; slf - shear layer flapping; Re_h - Reynolds number based on step height; X_R - reattachment length; h - step height

Chapter 3

Mixing Layers

The step flow contains within it a fluid pattern which is similar to a mixing layer [15]. This fluid pattern occurs downstream of the step edge when relatively low-speed fluid from the primary recirculation region moves downstream along with the relatively high-speed fluid from the boundary layer emanating off of the step edge (see Figure 2.4). As an indication that this area of the step flow behaves like a mixing layer, Kelvin-Helmholtz vortices have been observed in this region downstream of the step edge [17, 16]. In addition, some researchers analyze the recovery region of the step flow as a reattached mixing layer transforming back into an ordinary turbulent boundary layer [29, 14, 8]. Given this overlap, it is helpful, when analyzing the step flow, to possess some level of familiarity with the different characteristics of mixing layers.

3.1 Basic and Statistical Characteristics of Mixing Layers

Bell and Mehta [57] conducted an experimental investigation into mixing layers. In their experiments, mixing layers were generated through the use of a splitter plate, in which boundary layers with two different free-stream velocities developed on either side of the plate. After the splitter plate ended, the two streams of fluid flowed downstream adjacent to one another as a mixing layer in which the fluid from the two different streams interacted. A diagram of a possible experimental setup, similar to Bell and Mehta's, for generating a mixing layer is illustrated in Figure 3.1.

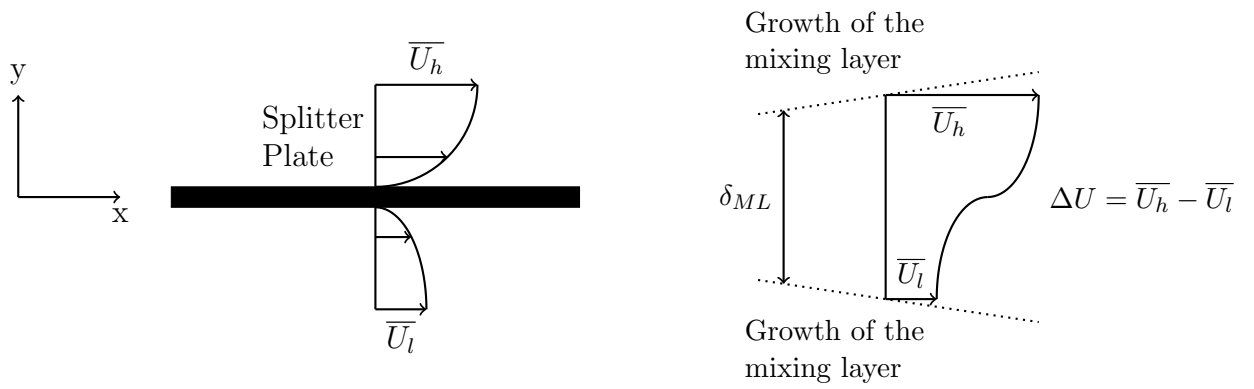


Figure 3.1: Generation of a mixing layer. Based upon [57, 1, 31].

At a certain distance downstream of the edge of the splitter plate, it is believed that mixing layers become self-similar. Bell and Mehta listed the conditions for self-similarity in a mixing layer as: (1) The width of the mixing layer (δ_{ML} in Figure 3.1) grows linearly with streamwise distance, i.e. $\frac{d\delta_{ML}}{dx} = Constant$, (2) The cross-stream mean streamwise deficit velocity profiles, with cross-stream distance measured relative to the mixing layer centerline¹ and scaled by local mixing layer width, $(y - y_{center})/\delta_{ML}(x)$, and mean streamwise velocity deficit scaled by the difference between the high- and low-speed free-stream velocities², $(\bar{U}(y) - \bar{U}_l)/\Delta U$ where $\Delta U = \bar{U}_h - \bar{U}_l$, remain constant with increasing streamwise distance, (3) The cross-stream turbulence profiles, with cross-stream distance measured relative to the mixing layer centerline and scaled by $\delta_{ML}(x)$ and the turbulence scaled by ΔU , remain constant with increasing streamwise distance, and (4) The peak cross-stream turbulence statistics remain constant with downstream distance. According to Bell and Mehta, all mixing layers become self-similar at some point downstream of the edge of the splitter plate. And according to theoretical arguments [31] combined with the scalings in Bell and Mehta, a theoretical, self-similar, cross-stream mean-streamwise velocity profile is:

$$\frac{\bar{U}(x, y) - \bar{U}_l}{\bar{U}_h - \bar{U}_l} = \frac{1 + erf\left(\frac{y - y_{center}}{\delta_{ML}(x)}\right)}{2} \quad (3.1)$$

where erf is the error function defined as [31]:

$$erf(z) = \frac{2}{\sqrt{\pi}} \int_0^z e^{-r^2} dr \quad (3.2)$$

Bell and Mehta presented mean streamwise velocity profiles scaled as in Eq. 3.1 and, after a certain distance downstream of the edge of the splitter plate (dependent upon the experimentally imposed initial conditions upstream of the splitter plate edge), the mean velocity profiles collapse with increasing downstream distance as in Eq. 3.1. These researchers also presented plots of the three normal Reynolds stresses and the Reynolds shear stress scaled by $(\Delta U)^2$ versus $(y - y_{center})/\delta_{ML}(x)$. The profiles showed that

¹It is difficult to discern exactly what Bell and Mehta meant by the mixing layer centerline, but from its name, it is reasonable to assume that the mixing layer centerline occurs at a cross-stream coordinate close to that of the splitter plate

²The high- and low-speed free-stream velocities should remain constant with streamwise distance [31].

the turbulence statistics achieved a self-similar state as well, with these profiles peaking around the center of the mixing layer and decreasing moving out towards the free-stream sides of the mixing layer, although it took a longer distance for the turbulence to reach self-similarity than for the mean velocity to reach self-similarity. In addition, Bell and Mehta also displayed plots of the cross-stream maximums of the Reynolds stresses versus streamwise distance. With enough downstream distance, all of these profiles reached an approximately constant value.

3.2 Distribution of Structure in Mixing Layers

Mixing layers are known to develop spanwise-oriented vortices called *rollers*, with volumes of fluid in between these vortices, called *braids*, which are devoid of rollers [58]. Figure 3.2 provides a rough sketch of rollers in a mixing layer.

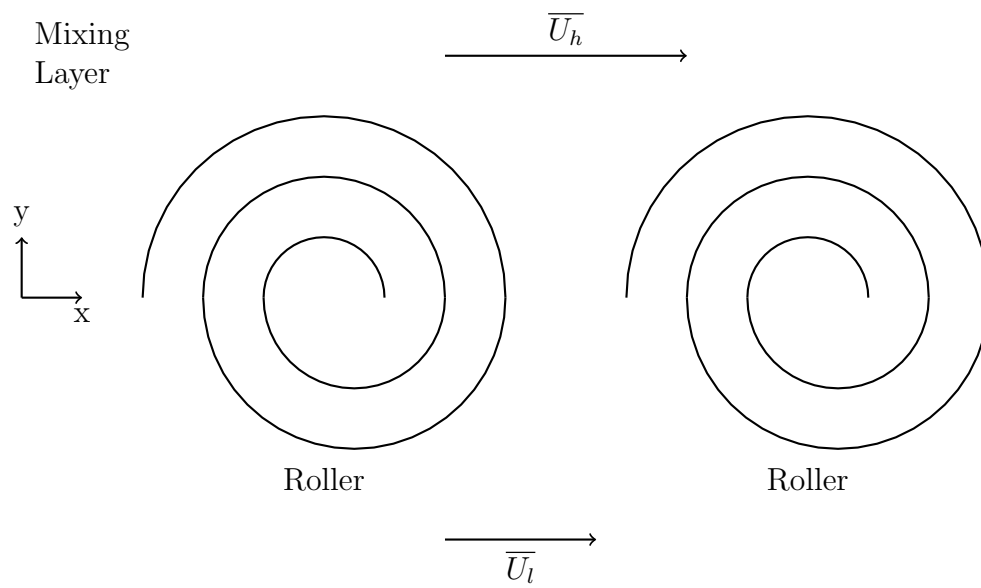


Figure 3.2: Rollers in a mixing layer.

Winant and Browand [59] proposed a model of mixing layer growth in which pairing of the rollers leads to increases in the cross-stream width of turbulent mixing layers. In addition, Rogers and Moser [58] stated that in laminar and transitional mixing layers, streamwise-oriented vortices, which can be called *ribs*, occur in the braid regions between the rollers and Bernard [60] observed these ribs in transitional mixing layers.

The work by Rogers and Moser [58], which was just alluded to, will now be described in greater detail, so that the results of this article can be better understood. Rogers and Moser conducted direct numerical simulations of temporally evolving, turbulent mixing layers. To simulate a temporally evolving mixing layer, Rogers and Moser took pre-existing data from simulated turbulent boundary layers and set them one on top of the other moving in opposite directions. Figure 3.3 illustrates how one might interpret a suggestion Rogers and Moser give for thinking about their simulations.

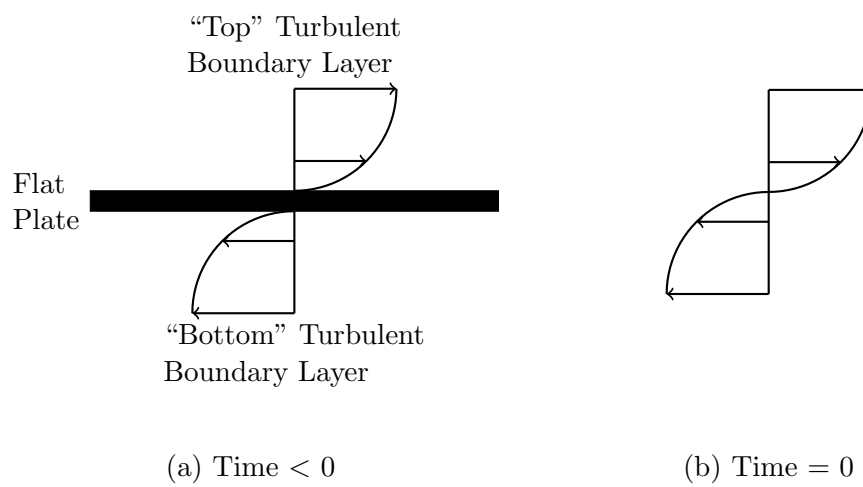


Figure 3.3: Generation of a temporally evolving mixing layer as suggested by Rogers and Moser [58]

Figure 3.3 suggests a scenario in which turbulent boundary layers develop on the two sides of a flat plate for $t < 0$. At $t = 0$, the plate is removed and the flow allowed to evolve from there. Rogers and Moser presented data from this simulation showing collapse of the mean velocity and streamwise normal Reynolds stress profiles when scaled by appropriate parameters. These researchers identified a time period in which the mixing layer was self-similar.

Rogers and Moser's simulations of a temporally evolving turbulent mixing layer [58] seemed to show that pairings of vortices and ribs are dependent upon initial conditions. Rogers and Moser conducted a baseline simulation which utilized pre-existing turbulent boundary layer data without any additional disturbances. In this baseline simulation, during the time period in which the mixing layer achieved self-similarity, the mixing layer contained rollers, but did not contain ribs or demonstrate evidence of vortex pairing. They also conducted two other simulations which utilized the same initial boundary layer data, but with added disturbances. One simulation contained disturbances of greater magnitude than the other. Rogers and Moser observed rollers in both of these simulations during self-similarity or approximate self-similarity. They also observed, during approximate self-similarity, the phenomenon of vortex pairing and the existence of ribs in the simulation with the largest initial disturbance. Based on these and other results, Rogers and Moser concluded that "coherent rib vortices can not survive unless there are well-formed braid regions." In addition, these results can lead one to wonder whether the existence of vortex pairing and ribs in turbulent mixing layers depend upon the initial or incoming conditions of the mixing layer [31].

Chapter 4

Zero Pressure Gradient Turbulent Boundary Layers

The step flow contains within it a number of different regions which are, or are similar to, flat plate boundary layers. In particular, prior to separation, flow over the upstream part of the step (prior to the step edge) is merely flow over a flat plate. In addition, due to the sudden expansion at the step edge for flow over a backward-facing step, there is a significant streamwise adverse pressure gradient that extends through the reattachment region [13, 14, 29]. But then, after a certain distance downstream of reattachment, the pressure gradient ‘levels-off’ and its impact upon the flow is not significant [29]. Given this overlap, the present chapter describes some of the characteristics of zero pressure gradient turbulent boundary layers while Appendix A describes some of the characteristics of adverse pressure gradient boundary layers.

4.1 Statistical Characteristics of ZPGTBLs

In ZPGTBLs the fluid’s velocity is zero at the solid boundary due to the no-slip condition and the mean streamwise velocity monotonically increases from zero at the solid boundary to the free-stream velocity at the edge of the boundary layer [30]. It is noteworthy that the Reynolds number which is often used to help describe boundary layers is $Re_\theta = \frac{\theta U_\infty}{\nu}$ [36].

One helpful set of scales with which to analyze TBLs is the set of wall scales [31]. This set includes the friction velocity, U_τ and a length scale,

defined below, along with the shear stress at the wall, τ_w [31]:

$$\tau_w \equiv \mu \frac{d\bar{U}}{dy}(0) \quad (4.1)$$

$$U_\tau \equiv \left(\frac{\tau_w}{\rho}\right)^{1/2} \quad (4.2)$$

$$y^+ \equiv \frac{U_\tau y}{\nu} \quad (4.3)$$

The fact that the mean streamwise velocity of a ZPGTBL increases from zero at the boundary to the free-stream velocity at the edge of the boundary layer, combined with the use of wall scaling makes it possible to split ZPGTBLs into different wall-normal regions. This breakdown is illustrated in Figure 4.1 (adapted from and based upon [31]).

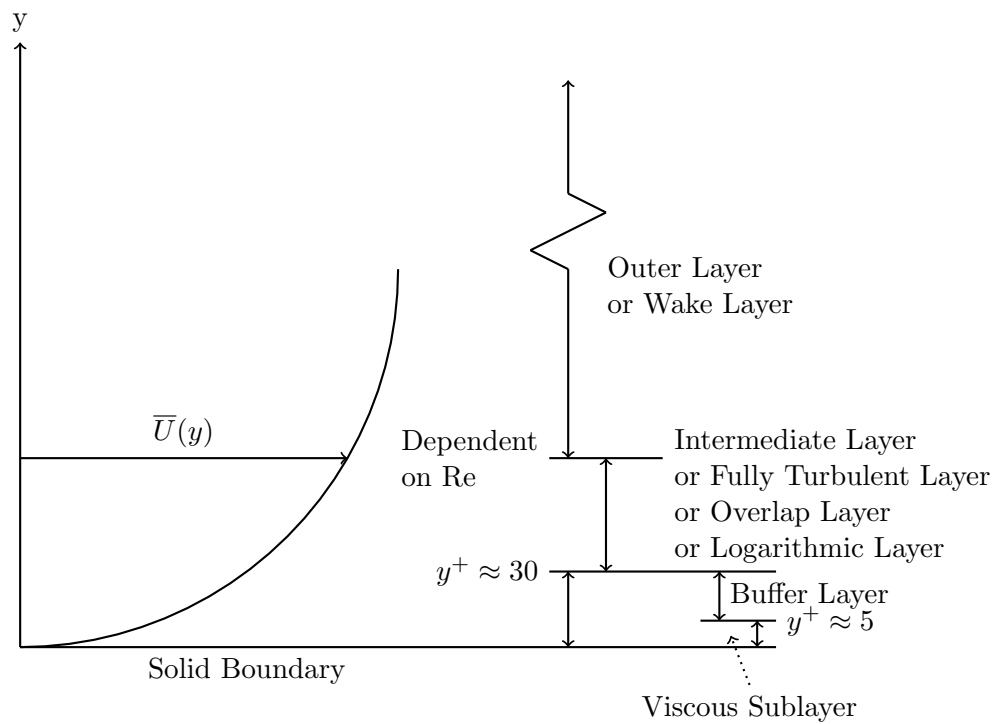


Figure 4.1: Breakdowns of a ZPGTBL into different wall-normal regions. Adpated from and based upon [31].

It is important to note that Figure 4.1 is not drawn to scale. The outer layer is, in fact, much larger than the logarithmic (log) layer or the viscous layer in that it extends over an approximate region $0.1 \leq y/\delta \leq 1$ [31].

The traditional understanding of the mean velocity profile in ZPGTBLs scaled by wall variables can be broken down into a few different wall-normal regions. In the viscous sublayer, traditional understanding dictates [31, 32]:

$$\bar{U}^+(y^+) = y^+, \quad 0 \leq y^+ \leq 5 \quad (4.4)$$

In the logarithmic layer, traditional understanding has dictated the existence of a logarithmic law [31] given by:

$$\bar{U}^+(y^+) = \frac{1}{\kappa} \ln y^+ + B \quad (4.5)$$

where $\kappa = 0.41$ and $B = 5.0$ have been used to match data from a ZPGTBL [34].

Past the log layer in the outer layer, the mean streamwise velocity profile in wall variables may be represented by Coles' law of the wake [32, 31]:

$$\bar{U}^+(y^+) = \frac{1}{\kappa} \ln y^+ + B + \frac{\Pi}{\kappa} W\left(\frac{y}{\delta}\right) \quad (4.6)$$

Coles offered the following approximation for $W\left(\frac{y}{\delta}\right)$ [32, 31]:

$$W\left(\frac{y}{\delta}\right) \approx 2 \sin\left(\frac{\pi y}{2\delta}\right) \quad (4.7)$$

Usually, the streamwise dependence of Π is ignored, and the value of Π is approximated as $\Pi = 0.55$ [32, 31].

Turning to other statistical measures, Wu and Moin [35] conducted a direct numerical simulation of a spatially-developing boundary layer over a flat plate. The flow developed from laminar to transitional to turbulent flow under a “nominal” zero pressure gradient. These researchers presented wall-normal profiles of the rms velocities in the turbulent region of their simulation at $Re_\theta = 900$. Their Figure 14 plotted $u'_{rms}, v'_{rms}, w'_{rms}$ versus y/δ . By observing this figure one can estimate that $u'_{rms,max} > v'_{rms,max} > w'_{rms,max}$ and that $u'_{rms,max}$ occurs at $y/\delta \approx 0.05$, $v'_{rms,max}$ occurs at $y/\delta \approx 0.2$, and $w'_{rms,max}$ occurs at $y/\delta \approx 0.1$. Their Figure 15 plotted u'^+, v'^+, w'^+ versus y^+ . By observing this figure one can estimate that, for wall scalings, $u'^+,_{rms,max}$

occurs at $y^+ \approx 15$, and that $v_{rms,max}^+$ and $w_{rms,max}^+$ do not exhibit a significant peak.

In addition, Wu and Moin provided plots of the wall-normal distribution of $-\overline{u'v'}^+$ in the turbulent region of their simulation at $Re_\theta = 900$. By observing these plots, one can estimate that $-\overline{u'v'}_{max}^+$ occurs at $y/\delta \approx 0.1$ or $y^+ \approx 40$.

Wu and Moin also plotted mean skin friction coefficient versus Re_θ . In the turbulent region for the Re_θ numbers plotted (from $Re_\theta \approx 750$ to $Re_\theta = 940$), one can estimate that the skin friction coefficient is around 0.0045.

4.2 Coherent Fluid Motions in ZPGTBLs

One prominent feature of turbulent boundary layers are low-speed streaks. Low-speed streaks are regions of low-momentum fluid that exist within turbulent boundary layers [38]. Kline et. al. [38] conducted an experimental investigation into turbulent boundary layers. These researchers provided hydrogen bubble visualizations of a turbulent boundary layer. By observing their visualizations one may observe that streaks are prominent in the boundary up until at least the region $y^+ \leq 9.6$. Kline et. al. classify these streaks as low-speed streaks. These researchers also stated that, based on one particular method of analysis, the mean spanwise spacing of the low-speed streaks is about 100 wall units. Based on these observations, one can draw the following illustration of low-speed streaks in a turbulent boundary layer.

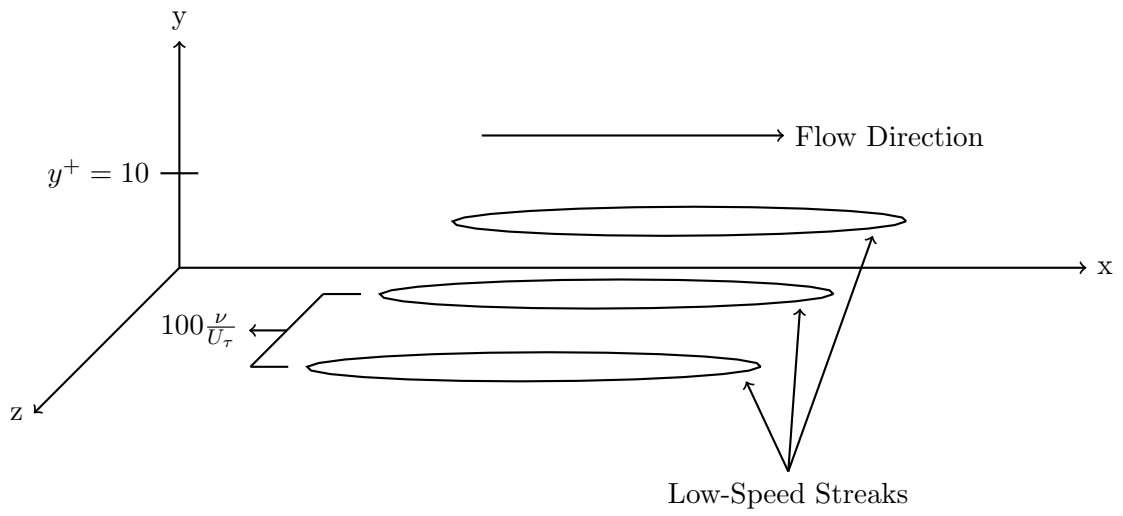


Figure 4.2: Illustration of low-speed streaks in a turbulent boundary layer

In addition to the existence of low-speed streaks, researchers have observed the existence of *ejections*, fluid motions in which low-speed fluid moves away from the boundary ($u' < 0, v' > 0$) and *sweeps*, fluid motions in which high-speed fluid moves toward the boundary ($u' > 0, v' < 0$) [37, 42].

Furthermore, there is a process called *bursting* which the streaks undergo. Kim, Kline, and Reynolds [39] break this bursting process into three stages. In the first stage, the low-speed streak moves outward from the wall. In the second stage, the streak oscillates. And in the third stage, the oscillatory movement ends and the streak moves back toward the boundary. These researchers also concluded that “essentially” all production of turbulence in the region $0 < y^+ < 100$ is generated during times in which bursts are happening. It is noteworthy that Kline et. al. [38] described a process in which streaks move away from the wall and then oscillate in the region $8 \leq y^+ \leq 12$ and breakup in the region $10 < y^+ < 30$. Kline et. al. also classified at least part of this series of events as a “bursting process.” It is also noteworthy that Willmarth and Lu [104] found that the greatest additions to the turbulent energy in a turbulent boundary layer takes place during bursting. Tardu [41] demonstrated that the bursting process consists of a series of ejections [37].

Another entity that exists in wall-influenced turbulence is the *hairpin* (or the *horseshoe* [40]). After reading Adrian’s [37] summary regarding coherent fluid motions in canonical wall turbulence, one may form an understanding of hairpins and the role they play in turbulent boundary layers. Figure 4.3 illustrates what a hairpin would look like in general, including the axis of the hairpin and the fluid motion it would induce.

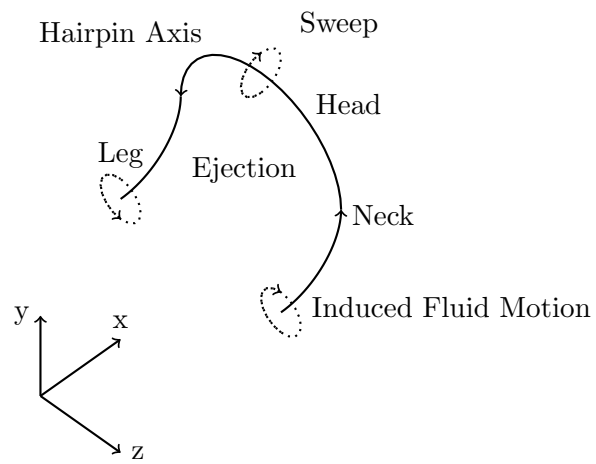


Figure 4.3: Illustration of a hairpin. Adapted from Figure 10 in [40].

This model of a hairpin utilizes an axis in the shape of a horseshoe. Head and Bandyopadhyay [75], in their experiments with ZPGTBLs, also found evidence for the existence of similarly shaped entities, with the ‘thickness’ of these entities dependent upon Re_θ . By observing Figure 4.3, it can be seen that the hairpin induces an ejection in the middle of the hairpin and a sweep immediately downstream of the hairpin. While Figure 4.3 displays a single hairpin, it is noteworthy that hairpins usually occur in *packets*, which consist of a series of hairpins progressing in the streamwise direction [37, 40], with hairpins created by a process called autogeneration [37, 43, 44]. Hairpin packets have been observed in the log region of a turbulent boundary layer¹ and hairpin packets have been observed extending into the outer region of a turbulent boundary layer [40].

With a model in which hairpins occur in packets, one may construct an argument in which these packets are responsible for the creation and ejection of low-speed streaks [37, 40]. According to this model, the hairpins within a packet induce low-speed fluid in their middle section as a result of the induced motion of the hairpin head and then eject this low-speed fluid as a result of the induced motion of the head and legs. Figure 4.4 illustrates this model.

¹Adrian and Liu [88], utilizing the results garnered from direct numerical simulations, presented evidence arguing for the existence of hairpin packets in fully-developed, turbulent channel flow and Christensen and Adrian [103] displayed experimental evidence which argued for the existence of hairpin packets in turbulent channel flow.

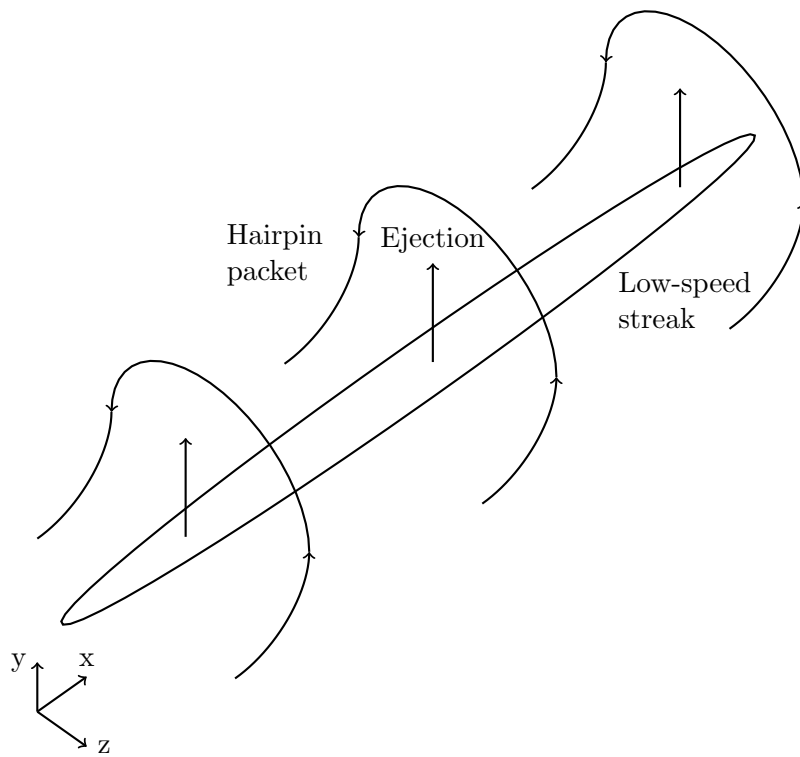


Figure 4.4: Illustration of a hairpin packet lifting a low-speed streak

Another entity present in wall-influenced turbulence is a *superstructure* [45]. Superstructures are usually associated with external geometries [45]. It is noteworthy that Hutchins and Marusic [46] used the results of experiments and a model to analyze turbulent boundary layers and found evidence of the existence of *superstructures* in the log layer and lower wake layer of turbulent boundary layers. Superstructures consist of spanwise-alternating areas of low and high-momentum fluid elongated in the streamwise direction that, according to Hutchins and Marusic, “meander” into and out of the spanwise direction. According to the analysis of Hutchins and Marusic, the length of the superstructures in the streamwise direction can extend past 20δ .

Chapter 5

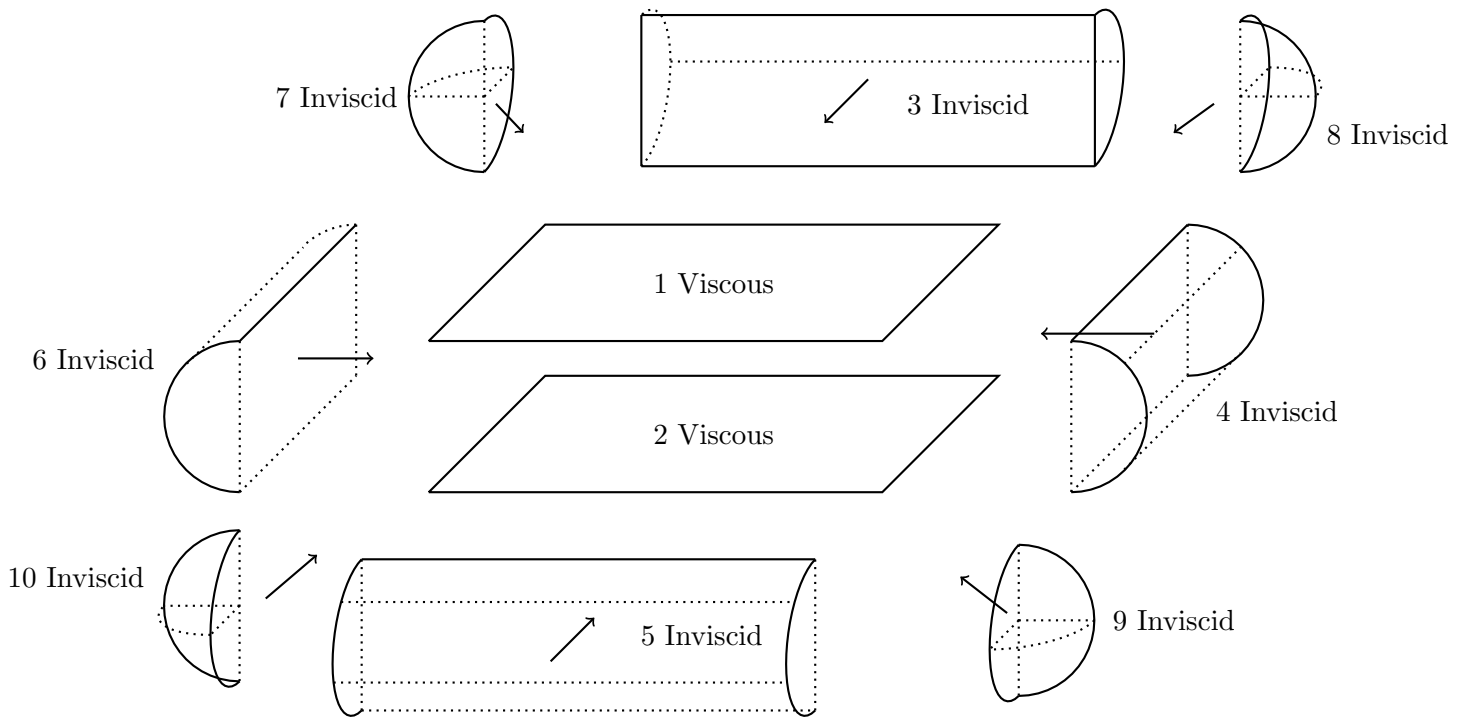
Operating Principles of the Gridfree Vortex Filament Scheme (GVFS)

This chapter explains how the gridfree vortex filament scheme, used in this thesis to simulate the step flow, works. To make things simpler, this chapter will describe how the gridfree vortex filament scheme simulates incompressible fluid flow over a flat plate. Chapter 7 will describe how the gridfree vortex filament scheme simulates incompressible flow over the backward facing step. Also, in the rest of this thesis, the gridfree vortex filament scheme will often be referred to by the acronym GVFS. Perhaps the most fundamental idea behind the GVFS, and vortex methods in general [61], is that, instead of directly calculating for the fluid's velocity at specified points in space, it calculates and tracks the movement of vorticity through the fluid. In the GVFS, the motion of vorticity away from solid boundaries is tracked by following the dynamics of vortex tubes in the flow [62].

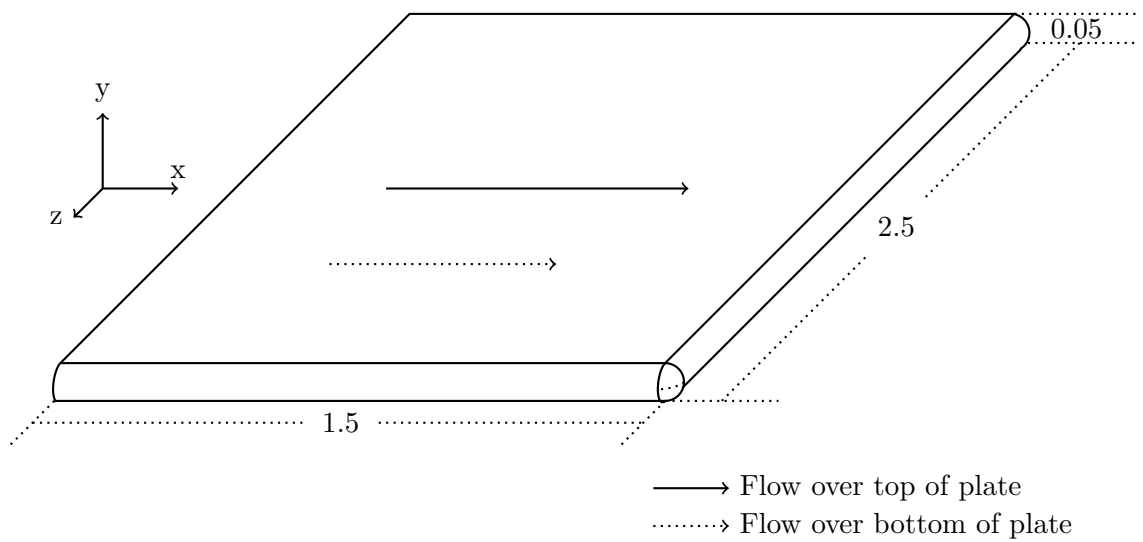
5.1 Flat Plate Geometry Utilized by the GVFS

This section describes the geometry used by the GVFS to simulate fluid flow over a flat plate. Unless otherwise noted, this section is based upon [62]. The GVFS needs rounded corners and a symmetric geometry (so that means that in the case of a flat plate, the fluid must be simulated as flowing over the top and bottom of the plate) in order to run. In addition, the surface of

the solid object over which the fluid is flowing (in this case a flat plate) can be composed of several *patches*. Each patch is designated as either viscous or inviscid. This designation affects the boundary conditions used for the surface area covering the patch so that vorticity is introduced into the flow where viscous patches are located but not where inviscid patches are located. Figure 5.1 illustrates a sample flat-plate geometry.



(a)



(b)

Figure 5.1: Schematic of flat-plate geometry: (a) Component Patches
 (b) Flat-plate geometry used by the GVFS

Figure 5.1a illustrates the component patches that make up the flat-plate geometry and notes whether these patches are viscous or inviscid. Figure 5.1b illustrates the entire flat-plate geometry including the coordinate system and the dimensions of the plate. The lengths in the figure are non-dimensionalized by the length scale L . The origin of the coordinate system (although it's not depicted at exactly this position in the figure) is actually at the upstream end of the plate halfway in between the top and bottom of the plate and halfway in between the largest and smallest spanwise (z-direction) coordinate of the plate. So that means that, with the origin at $(x = 0, y = 0, z = 0)$ the top plate is located at $y = 0.025$, the bottom plate is located at $y = -0.025$, the spanwise ends of the plate are located at $z = 1.25$ and $z = -1.25$, and the downstream end of the plate is located at $x = 1.5$. And, because the GVFS needs a symmetric geometry to run, fluid flows over the top and bottom of the plate as illustrated in the figure.

In addition, the simulation is scaled as follows: the 'global' Re number is $Re = U_\infty L / \nu$, where U_∞ is the free-stream velocity, L is a length scale, and ν is the kinematic viscosity. Prior to the start of the simulation, the Re number, U_∞ , and L are chosen. This then determines ν . Unless otherwise noted, for the rest of this thesis, the quantities (vorticity, velocity, etc.) simulated by the GVFS are non-dimensionalized by the appropriate combination of L , U_∞ , and/or ν .

5.2 Explanation of the Finite Volume/Finite Difference Scheme Adjacent to Solid Boundaries

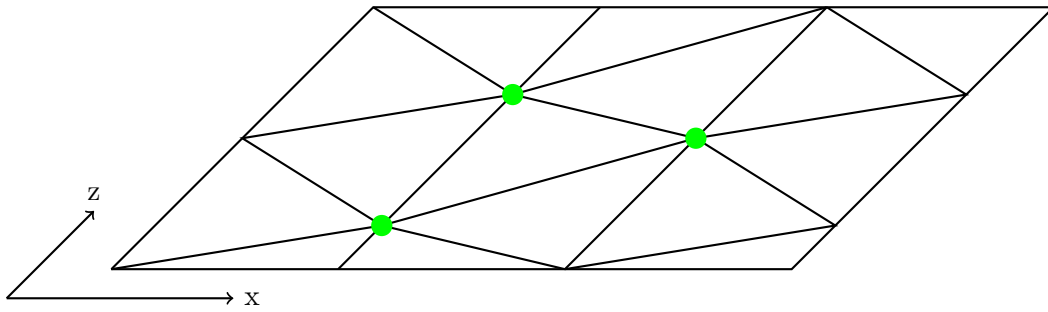
The simulation technique of using vortex tubes to track the movement of vorticity through a flow, which the GVFS does, can be categorized as a large eddy simulation (LES), in which the effects of the smaller scales of the flow upon the larger scales of the flow are modeled [31]. Although effective away from the immediate vicinity of solid boundaries, tracking the motion of vortex tubes adjacent to solid boundaries fails to capture much of the 'activity' that occurs in this region. For instance, gradients of vorticity in conjunction with viscosity produce vorticity at the solid boundary and it is not safe to assume that vortex tubes can adequately simulate this phenomenon [62]. In addition, there is a lot of turbulent activity that takes place in the near-wall region.

For instance, in a turbulent boundary layer, both the production of turbulent kinetic energy and Reynolds shear stress peak for $y^+ < 20$ [30]. Because there is so much ‘activity’ near the wall for fluid flowing over a solid boundary, it is necessary to use direct numerical simulations (DNS) for this region [62]. In this vein, the GVFS uses a finite volume/finite difference solver to solve for the fluid’s vorticity in a region that usually extends from the solid boundary to about $y^+ \approx 25$ [62]. This section of the thesis explains how this finite volume/finite difference scheme works. Unless otherwise noted, this section is based upon [62] and examination of the GVFS’s code.

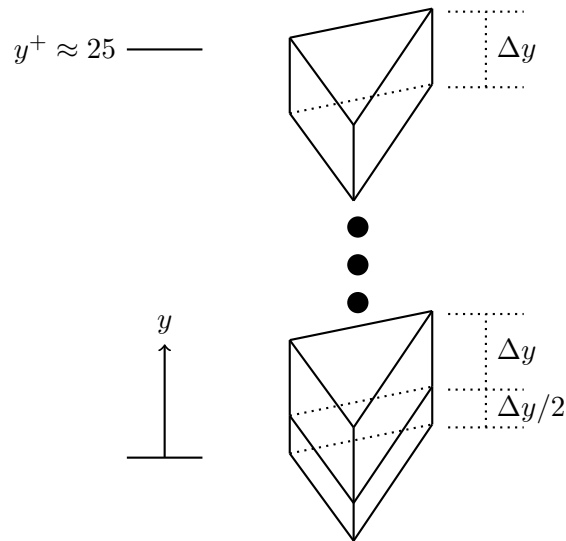
To start out, the finite volume/finite difference scheme solves the non-dimensionalized vorticity equation. In index notation, the non-dimensionalized vorticity equation is:

$$\frac{\partial \Omega_i}{\partial t} + U_j \frac{\partial \Omega_i}{\partial x_j} = \Omega_j \frac{\partial U_i}{\partial x_j} + \frac{1}{Re} \nabla^2 \Omega_i \quad (5.1)$$

The finite volume/finite difference scheme utilizes a mesh composed of triangular prisms. First, the solid surfaces are covered with contiguous triangles. The mesh is built up in the wall-normal (y) direction by constructing normals to the surface triangle. The first layer of the mesh is of half-thickness $\Delta y/2$ and the layers on top of that are all of thickness Δy . As mentioned before, the mesh usually extends from the solid boundary to about $y^+ \approx 25$. The surface mesh and the resulting mesh built from it are illustrated in Figure 5.2 for a flat plate. Figure 5.2a illustrates a sample flat surface covered with triangles and Figure 5.2b illustrates the triangle demarcated with green dots built up into the flow with the layer closest to the surface of thickness $\Delta y/2$.



(a)



(b)

Figure 5.2: Wall-adjacent mesh used in the finite volume/finite difference scheme: (a) Triangles covering a flat plate surface (b) Triangle demarcated with green dots in (a) built up into a mesh that extends into the flow

For each triangular prism, the vorticity is considered to be constant within the prism and equal to its value at the center of the prism while the velocity is determined at the top and bottom triangles of the prism. This is illustrated in Figure 5.3.

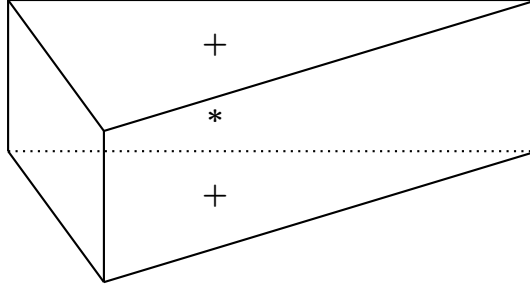


Figure 5.3: Illustration of a triangular prism in the mesh. Velocity is calculated at the points labeled with + and vorticity is calculated at the point labeled with *. Copied from Figure 1 of [62].

Turning back to the solution of the vorticity equation, Eq. 5.1, in this mesh, each term is treated differently. It's worthwhile to keep in mind that although the numerical scheme which solves the vorticity equation is referred to as a finite volume/finite difference scheme, it is solving for the vorticity at the center of the prisms and the velocities on the tops and bottoms of the prisms as is illustrated in Figure 5.3. To determine the value of the convection term, $U_j \partial \Omega_i / \partial x_j$, at the center of the prism, the continuity equation is invoked, and then its value is averaged over the prism and the divergence theorem is invoked leading to:

$$U_j \frac{\partial \Omega_i}{\partial x_j} = \frac{\partial U_j \Omega_i}{\partial x_j} \approx \frac{1}{V_T} \int_{V_T} \frac{\partial U_j \Omega_i}{\partial x_j} dV = \frac{1}{V_T} \sum_k A^k \Omega_i^k (U_j^k n_j^k) \quad (5.2)$$

where V_T is the volume of the prism and the discrete sum is over the sides of the prism with A^k the area of side k and n_j^k the j th component of the outward-facing unit normal of side k . The velocities on the triangular faces are used as in Figure 5.3. The velocities on the rectangular faces are calculated from a compilation of averages of the velocities on the triangular faces. In addition, the vorticity on the triangular sides of the prism are taken from the upwind

prism. For instance, if the velocity on the top triangle in Figure 5.3 points up, then the vorticity on the top triangle in Eq. 5.2 is considered to be the vorticity from the prism pictured in Figure 5.3. If not, the vorticity is considered to be that from the prism directly above the prism pictured in Figure 5.3. The reasoning behind this methodology is that the convection term represents the velocity transporting the vorticity through the fluid and if the velocity on the top face in Figure 5.3 is up then that represents the velocity convecting the vorticity in the prism pictured in Figure 5.3 upward. The opposite occurs if the velocity on the top face is down. To evaluate the vorticity on the rectangular faces of the prism in Eq. 5.2 the following process is used: given a rectangular side, the upwind prism of the side as well as the immediately adjacent prisms to the upwind prism of the side in the same wall-normal layer as the face along with the layers above and below this layer, and the one prism on the downstream side of the face are used to create a linear least squares fit of the vorticity. The vorticity on the side of the prism is determined from this linear least square fit. This process is illustrated with a picture, Figure 5.4.

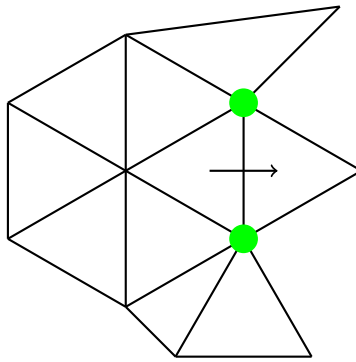


Figure 5.4: Illustration of prisms used in the linear least square fit of vorticity for a side face. The face upon which the vorticity is calculated is demarcated with green dots. The arrow in the figure represents the direction of the velocity at the side. Adapted from Figure 2 of [62].

It is important to note that Figure 5.4 is a view of the prisms “looking down” and that the linear least squares fit incorporates the upwind prisms from the same wall-normal layer as the side as well as the layers above and below this layer and the downwind prism from just the same layer as the side.

To evaluate the vortex stretching term, $\Omega_j \partial U_i / \partial x_j$, in Eq. 5.1 at the center of the prism, the vorticity is taken from the center of the prism, while $\partial U_i / \partial x_j$ is evaluated in a manner similar to the convection term. Specifically, $\partial U_i / \partial x_j$ is evaluated at the center of the prism by first averaging it over the prism and then utilizing the divergence theorem:

$$\frac{\partial U_i}{\partial x_j} \approx \frac{1}{V_T} \int_{V_T} \frac{\partial U_i}{\partial x_j} dV = \sum_k A^k U_i^k n_j^k \quad (5.3)$$

The evaluation of the velocities in Eq. 5.3 is achieved in a manner similar to the convection term.

To evaluate the Laplacian in the diffusion term, $\nabla^2 \Omega_i$, in Eq. 5.1, the Laplacian is expressed in a coordinate system which consists of a wall-normal direction, n , and two tangential directions, t_1 and t_2 which are at right angles to the wall-normal direction. The Laplacian in the diffusion term can then be written as:

$$\nabla^2 \Omega_i = \frac{\partial^2 \Omega_i}{\partial n^2} + \frac{\partial^2 \Omega_i}{\partial t_1^2} + \frac{\partial^2 \Omega_i}{\partial t_2^2} \quad (5.4)$$

The $\partial^2 \Omega_i / \partial n^2$ term is calculated using a second-order finite difference scheme. If, for instance, $\Omega_1(n_i)$ is the value of Ω_1 in the prism with wall-normal height n_i and $\Omega_1(n_{i+1})$ is the value of Ω_1 in the prism immediately above that prism and $\Omega_1(n_{i-1})$ is the value of Ω_1 immediately below it, then:

$$\frac{\partial^2 \Omega_1}{\partial n^2}(n_i) \approx \frac{1}{\Delta n^2} \left(\Omega_1(n_{i+1}) - 2 * \Omega_1(n_i) + \Omega_1(n_{i-1}) \right) \quad (5.5)$$

To calculate the $\partial^2 \Omega_i / \partial t_1^2$ and $\partial^2 \Omega_i / \partial t_2^2$ terms, the GVFS differentiates a polynomial created by a second-order least-squares fit of the vorticities in the prisms contained within a radius from the center of the prism where the Laplacian is being calculated at the same wall-normal layer as the prism where the Laplacian is being calculated as well as the layers above and below this layer. The radius within which prisms are included for the second-order least-squares fit is $1.2e_{max}$, where e_{max} is the maximum edge length of the triangle from the prism where the Laplacian is being calculated.

The finite volume/finite difference solver is moved forward in time by Δt using the standard explicit Euler scheme. Δt is controlled by CFL limits as well as the presence of the viscous diffusion term in the non-dimensionalized vorticity equation. With L_T as the average edge length of the triangles in the mesh, C_{CFL} as a parameter that generally is 0.3, U_{\max} as the greatest tangential velocity in the wall-adjacent mesh, and V_{\max} as the greatest normal velocity in the wall-adjacent mesh, these conditions come out to be:

$$\Delta t \leq \min(C_{CFL}\Delta y/V_{\max}, C_{CFL}L_T/U_{\max}) \quad (5.6)$$

$$\Delta t \leq \frac{Re}{8}L_T^2 \quad (5.7)$$

The GVFS generally uses triangles whose dimensions are about ten times that of the wall-normal height of the prisms. Because of this, the most restrictive condition in Eqs. 5.6 and 5.7 is usually the one involving Δy .

The vortex tubes in the GVFS can be moved forward in time using a larger time step than Δt . Because of this, N_S time steps of the finite volume/finite difference scheme, with each time step of duration Δt , are calculated before the vortex tubes are moved forward in time. The vortex tubes are therefore moved forward in time using a time step of duration $\Delta t^* = N_S\Delta t$. Runge-Kutta schemes are utilized to move the vortex tubes forward in time.

The finite volume/finite difference solver also employs boundary conditions at the top and bottom layers of the mesh. For the bottom layer of the mesh (which has thickness $\Delta y/2$ as in Figure 5.2b), the boundary condition utilized is obtained by a combination of the no-slip condition and an appropriate form of the divergence theorem as follows: One form of the divergence theorem has, for an arbitrary vector function \mathbf{G} in a volume of space V enclosed by surface S :

$$\int_V \nabla \times \mathbf{G} dV = \int_S \mathbf{dS} \times \mathbf{G} \quad (5.8)$$

Setting $\mathbf{G} = \mathbf{U}$ in Eq. 5.8 and noting the definition $\boldsymbol{\Omega} = \nabla \times \mathbf{U}$ yields:

$$\int_V \boldsymbol{\Omega} dV = \int_S \mathbf{dS} \times \mathbf{U} \quad (5.9)$$

Assuming that the vorticity at the center of a prism is an average of its value over the prism and taking the volume of integration in Eq. 5.9 to be a prism adjacent to the solid boundary of volume V_T bounded by surface S_T yields an

approximation for the value of the vorticity at the center of a prism adjacent to the solid boundary, Ω_{V_T} :

$$\Omega_{V_T} \approx \frac{1}{V_T} \int_{V_T} \Omega dV = \frac{1}{V_T} \int_{S_T} \mathbf{dS} \times \mathbf{U} \quad (5.10)$$

Breaking up the surface integral in Eq. 5.10 into a discrete sum over the faces of the prism yields:

$$\Omega_{V_T} \approx \frac{1}{V_T} \sum_{k=0}^4 A^k (\mathbf{n}^k \times \mathbf{U}^k) \quad (5.11)$$

where A^k is the area of side k , \mathbf{n}^k is the outward facing normal to side k , and \mathbf{U}^k is the velocity on side k . In Eq. 5.11, the sum only goes over four of the five faces of the prism, because on the face which lies on the solid boundary, the velocity is zero due to the no-slip condition. If a bottom prism is at an angle to the coordinate system employed in the simulation, then the vorticity expressed in terms of this coordinate system is determined through projections.

The boundary conditions that the finite volume/finite difference solver utilizes at the top layer of the mesh furthest away from the solid boundary has to do with the creation of vortex tubes based upon vorticity that is being transported away from the solid boundary through convection and viscous diffusion. The idea behind the creation of vortex tubes in the GFVS is that the flux of vorticity outward from the wall due to convection and viscous diffusion between the top two layers in the mesh gets siphoned off into a new vortex tube, as opposed to moving into the top layer of the mesh. This is illustrated in Figure 5.5.

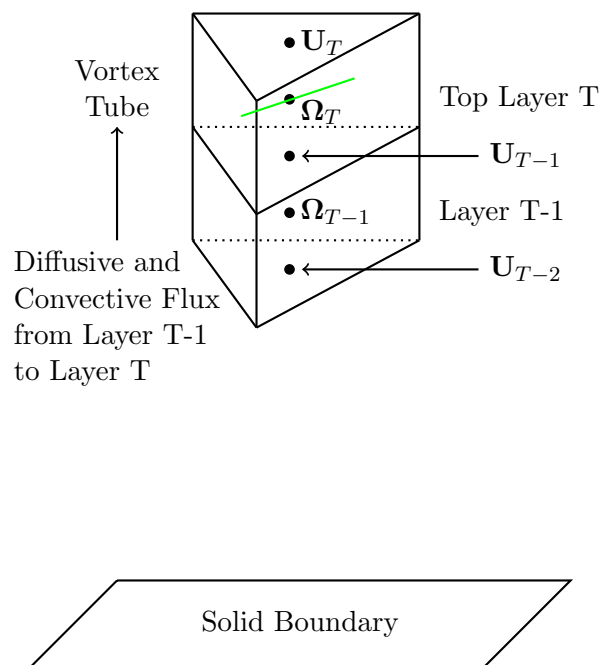


Figure 5.5: Convective and diffusive flux of vorticity siphoned off into a vortex tube (vortex tube in green)

This vortex tube creation process leads to boundary conditions for the vorticity in the top layer of the mesh (Ω_T in Figure 5.5). With regard to the convection of vorticity between the top two prism layers, if the velocity \mathbf{U}_{T-1} (using the notation of Figure 5.5) points away from the solid boundary, that is indicative of the vorticity in layer $T - 1$, Ω_{T-1} , convecting into layer T , so that the vorticity in the top layer T , Ω_T , does not play a role in the finite volume/finite difference solver (see Figure 5.4). If, on the other hand, \mathbf{U}_{T-1} points toward the solid boundary and vorticity is being convected from layer T to layer $T - 1$, Ω_T is considered to be zero, because the transport of vorticity between layer T and layer $T - 1$ is accounted for using vortex tubes, not the vorticity in the prisms in the mesh.

With regard to the diffusion of vorticity between the top two layers of the mesh, one can account for the net diffusive flux between the top two layers of the mesh going towards a vortex tube by implementing the boundary condition:

$$\left. \frac{\partial^2 \Omega}{\partial n^2} \right|_{T-1} = 0 \quad (5.12)$$

In this equation, the derivative is evaluated at the layer $T - 1$. Eq. 5.12 can be understood by approximating it as:

$$\left. \frac{\partial^2 \Omega}{\partial n^2} \right|_{T-1} \approx \frac{1}{\Delta n} \left(\left. \frac{\partial \Omega}{\partial n} \right|_{T-\frac{1}{2}} - \left. \frac{\partial \Omega}{\partial n} \right|_{T-\frac{3}{2}} \right) \quad (5.13)$$

where $T - \frac{1}{2}$ and $T - \frac{3}{2}$ represent values from the top and bottom triangle faces, respectively, of the prism layer right below the top prism layer. By examining the Laplacian term of the non-dimensionalized vorticity equation integrated over a prism volume V_T and applying the divergence theorem, meaning may be given to the derivatives on the right-hand side of Eq. 5.13:

$$\frac{1}{Re} \int_{V_T} \frac{\partial}{\partial x_j} \frac{\partial}{\partial x_j} \Omega_i dV = \frac{1}{Re} \int_{S_T} n_j \frac{\partial \Omega_i}{\partial x_j} dS = \frac{1}{Re} \sum_k A^k n_j^k \frac{\partial \Omega_i^k}{\partial x_j} \quad (5.14)$$

Eq. 5.14 can be interpreted to mean that the volume integral of the diffusive term in the vorticity equation over a prism volume is equal to the net flux of gradients of vorticity over the surface of the prism volume. The first and second terms on the right-hand side of Eq. 5.13 can then be interpreted as proportional to the net diffusive flux of vorticity through the top and bottom

triangular faces of the prism layer $T - 1$ respectively. Combining Eqs. 5.12 and 5.13 and multiplying through by Δn one obtains:

$$\frac{\partial \Omega}{\partial n} \Big|_{T-\frac{1}{2}} - \frac{\partial \Omega}{\partial n} \Big|_{T-\frac{3}{2}} = 0 \quad (5.15)$$

Eq. 5.15 expresses the idea that the net diffusive flux between the top two prism layers is balanced by the net diffusive flux between the prism layers second and third from the top prism layer. This allows the net diffusive flux between the top two prism layers to be put towards a new vortex tube.

Figure 5.5 can be used to illustrate how the vortex tube creation process works in the GFVS. As time advances, the net vorticity due to convection and viscous diffusion that moves upward from Layer $T - 1$ to Layer T is recorded. When the magnitude of this net vorticity for a given prism, $|\Omega|$, is greater than a pre-determined threshold, $|\Omega|_{\max}$, a vortex tube is created¹ with circulation Γ given by,

$$\Gamma |\mathbf{s}| = |\Omega| V_T \quad (5.16)$$

where \mathbf{s} is the length of the new vortex tube and V_T is the volume of the top prism, Layer T in Figure 5.5. The midpoint of this new vortex tube is located at the center of the top prism, Layer T and oriented in a direction parallel to the net convected and diffused vorticity that has built-up over time. The length of the new vortex tube is set to approximately intersect the sides of the prism. Eq. 5.16 insures that the velocity induced by the new vortex tube far away from its initial location is equivalent to the velocity induced by the vorticity in the prism where it is initially located.

The GVFS first determines how much convected vorticity between the top two prism layers will go towards a new vortex tube and then determines how much diffused vorticity between the top two layers will go towards a new vortex tube. The GVFS determines an expression for the convection of vorticity between the top two prism layers that will go towards a new vortex tube through the following methodology: start out with Eq. 5.2, which approximates the convection term in the vorticity equation within a prism as the sum of effects over the surface of the prism. In this equation, select

¹The vorticity is allowed to build-up over time because, if it weren't and vortex tubes were released into the flow at every time step, many weak vortex tubes would enter the flow and that would make the actual computations less efficient.

the triangular face between the top two prism layers and say that it has area A , vorticity Ω_i (in index notation), velocity U_i (also in index notation), and upward-pointing unit normal n_i (also in index notation). If U_i points up then it is assumed that the vorticity from the prism layer right below the top prism layer is being convected upward, but if U_i points downward then no convected vorticity is put towards a new vortex tube in accordance with the boundary conditions described earlier in this section. It is also important to note that the build-up of vorticity by convection that is to be turned into a new vortex tube occurs over a number of time steps.

The GVFS determines an expression for the viscous diffusion of vorticity between the top two prism layers that will go towards a new vortex tube through the following methodology: Eq. 5.12 is first approximated using a three-point centered difference approximation with the resulting equation solved for Ω_T . This yields

$$\Omega_T = 2\Omega_{T-1} - \Omega_{T-2} \quad (5.17)$$

Then, along the lines of Eq. 5.14, the net diffusive flux between the top two prism layers is considered to be proportional to $-\frac{\partial\Omega}{\partial n}\Big|_{T-\frac{1}{2}}$, which is approximated as

$$-\frac{\partial\Omega}{\partial n}\Big|_{T-\frac{1}{2}} \approx \frac{\Omega\Big|_{T-1} - \Omega\Big|_T}{\Delta n} \quad (5.18)$$

The minus sign in Eq. 5.18 is a result of the fact that if $\Omega_T > \Omega_{T-1}$ the net diffusion of vorticity is downward whereas the vorticity that goes towards a new vortex tube is that which moves upward.

As the finite volume/finite difference solver moves forward in time by time step Δt , the convected vorticity between the top two prism layers that moves upward and the net, upward-moving vorticity due to diffusion is accumulated in a variable Ω_{bin} . Using approximations based upon Eqs. 5.2 and 5.14, the GVFS calculates the Ω_{bin} which accumulates over a series of time steps of duration Δt in a prism of volume V_T as

$$\Omega_{\text{bin}} = \sum_j \left\{ \frac{A}{V_T} \Omega^j (\mathbf{U}^j \cdot \hat{\mathbf{n}}) (1_{\mathbf{U}^j \cdot \hat{\mathbf{n}} > 0}) \Delta t + \frac{1}{\Delta n} \frac{1}{Re} \frac{\Omega_{T-1}^j - \Omega_T^j}{\Delta n} \Delta t \right\} \quad (5.19)$$

In Eq. 5.19, the first term on the right-hand side is due to convection while the second term on the right-hand side is due to diffusion, the discrete sum

is over a series of time steps, the vorticity $\boldsymbol{\Omega}^j$ is from the prism from layer $T - 1$, the velocity \mathbf{U}^j is on the bottom triangular face of layer T , the unit normal vector \mathbf{n} points upward, and the expression $1_{\mathbf{U}^j \cdot \hat{\mathbf{n}} > 0}$ is the indicator function:

$$1_{\mathbf{U}^j \cdot \hat{\mathbf{n}} > 0} = \begin{cases} 1, & \mathbf{U}^j \cdot \hat{\mathbf{n}} > 0 \\ 0, & \mathbf{U}^j \cdot \hat{\mathbf{n}} \leq 0 \end{cases} \quad (5.20)$$

In addition, one of the factors of $1/\Delta n$ in the second term on the right-hand side of Eq. 5.19 is due to the finite volume/finite difference solver making the simplification $A/V_T = 1/\Delta n$. The expression for $\boldsymbol{\Omega}_{\text{bin}}$ in Eq. 5.19 is what is used on the right-hand side of Eq. 5.16 to calculate the circulation of a new vortex tube.

The initial condition that the GVFS employs has the interior of the fluid started off with unit velocity in the streamwise direction with the other velocity components started off with zero velocity. The solid surfaces designated as viscous patches start out with, and maintain, zero velocity on the boundary (no-slip), while the solid surfaces designated as inviscid patches start out with, and maintain, only that the velocity component normal to the boundary is zero. Vorticity enters the flow at the viscous patches on the solid surface through the no-slip condition and in the laminar regime for flow over a flat plate, the GVFS generates a Blasius boundary layer. For flow over a flat plate, the flow undergoes transition toward a turbulent boundary layer downstream of the leading edge of the plate due to perturbations that result from the use of vortex filaments in simulating the dynamics of the fluid [63]. Downstream of the transition region for flow over a flat plate, the fluid becomes completely turbulent and a plot of averaged \bar{U}^+ versus y^+ achieves “qualitative agreement with a log-type law and $\bar{U}^+ = y^+$ trend near the wall” [62].

5.3 Kelvin’s Circulation Theorem and Helmholtz’s Vortex Theorems

Before discussing how the GVFS calculates the fluid’s velocity and how the motions of the vortex tubes are computed, it is worthwhile to discuss some of the theoretical underpinnings upon which the GVFS operates. In that vein, this section discusses Kelvin’s Circulation Theorem and states Helmholtz’s vortex theorems. Section 5.4 discusses the velocity field calculation utilized

by the GVFS and Section 5.5 discusses the phenomenon of vortex stretching and reorientation. Unless otherwise noted, this section is based upon [33].

Before discussing Kelvin's circulation theorem and stating Helmholtz's vortex theorems it is worthwhile to describe what vortex lines and vortex tubes are. A vortex line is a line through a fluid that is tangent to the vorticity of the fluid and a vortex tube is the set of vortex lines that pass through a given closed curve. Figure 5.6 illustrates a vortex line and tube.

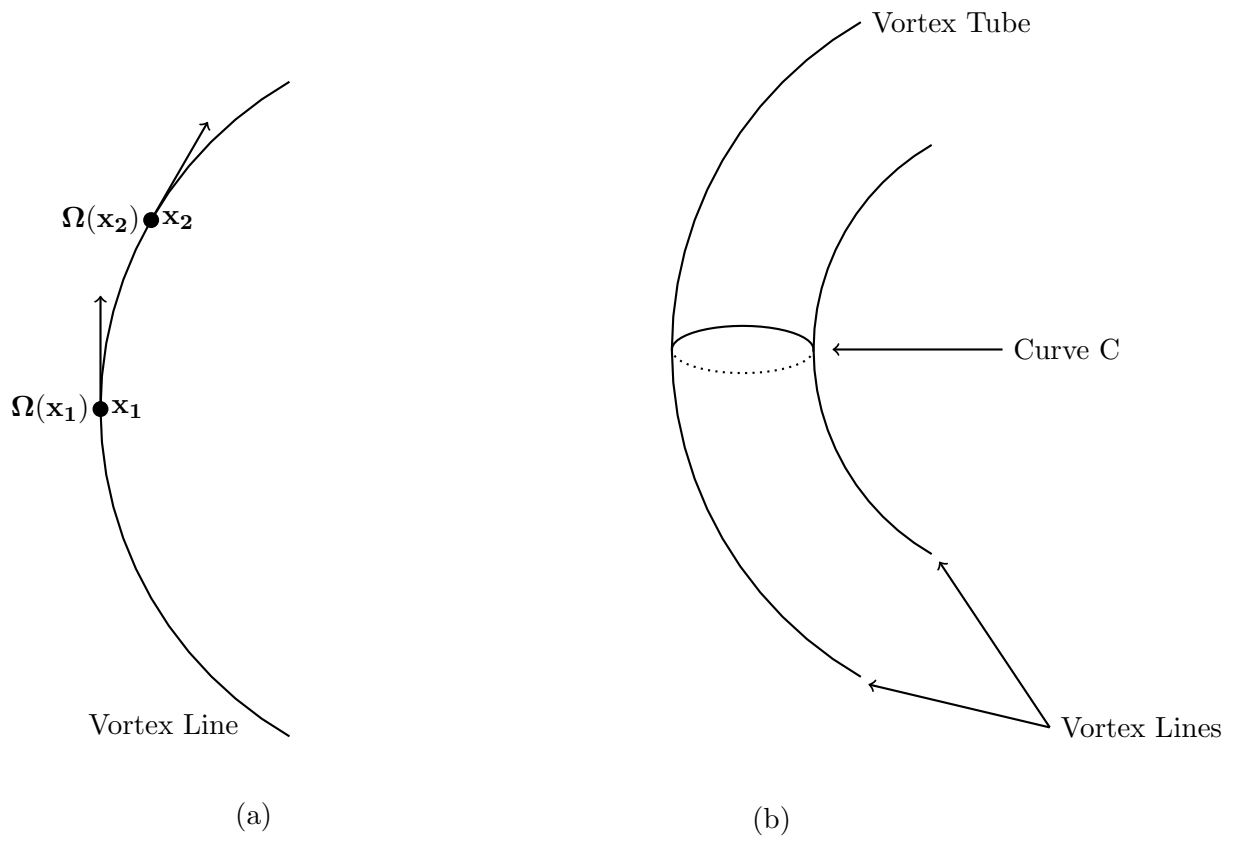


Figure 5.6: (a) Vortex Line (b) Vortex Tube

The strength, Γ of a vortex tube is the circulation of a closed curve that goes around its surface, such as curve C in Figure 5.6b:

$$\Gamma = \int_C \mathbf{U} \cdot d\mathbf{s} = \int_A \boldsymbol{\Omega} \cdot d\mathbf{S} \quad (5.21)$$

where A is a surface area bounded by curve C and the second equality is generated from Stokes' Theorem and the definition $\boldsymbol{\Omega} = \nabla \times \mathbf{U}$.

With these definitions, Kelvin's circulation theorem can now be stated subject to the following four conditions:

1. The region of fluid where Kelvin's circulation theorem is applied is not subject to net viscous forces.
2. The body forces in the region of fluid where Kelvin's circulation theorem is applied are conservative.
3. The density of the fluid in the region where Kelvin's circulation theorem is applied is a function of pressure alone.
4. The frame of reference in which the fluid is described is inertial.

Given these four conditions, Kelvin's circulation theorem is: the circulation generated from a closed curve which convects with the fluid does not change in time or:

$$\frac{D\Gamma}{Dt} = 0 \quad (5.22)$$

A short proof of Kelvin's circulation theorem will now be given. Expanding Eq. 5.22 yields:

$$\frac{D\Gamma}{Dt} = \frac{D}{Dt} \int_C U_i dx_i = \int_C \frac{Du_i}{Dt} dx_i + \int_C U_i \frac{D}{Dt}(dx_i) \quad (5.23)$$

The term $\int_C Du_i/Dt dx_i$ in Eq. 5.23 can be expanded using the Navier-Stokes equation with g_i as the body force and σ_{ij} as the deviatoric stress tensor:

$$\int_C \frac{Du_i}{Dt} dx_i = \int_C \left(-\frac{1}{\rho} \frac{\partial p}{\partial x_i} + g_i + \frac{1}{\rho} \frac{\partial \sigma_{ij}}{\partial x_j} \right) dx_i \quad (5.24)$$

By expressing the body force as the gradient of a potential function Φ , one can transform Eq. 5.24 into:

$$\int_C \frac{Du_i}{Dt} dx_i = - \int_C \frac{1}{\rho} dp - \int_C d\Phi + \int_C \frac{1}{\rho} \frac{\partial \sigma_{ij}}{\partial x_j} dx_i \quad (5.25)$$

Given that the curve C is closed, the first term on the right-hand side of Eq. 5.25 is zero when the density is a function of pressure only. The second term on the right hand side of Eq. 5.25 is also zero. This leads to:

$$\int_C \frac{Du_i}{Dt} dx_i = \int_C \frac{1}{\rho} \frac{\partial \sigma_{ij}}{\partial x_j} dx_i \quad (5.26)$$

Next, attention is turned to the term $\int_C U_i \frac{D}{Dt}(dx_i)$ in Eq. 5.23. Figure 5.7 will help in the evaluation of this term.

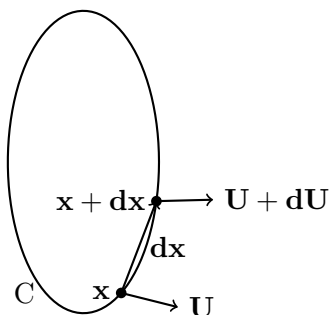


Figure 5.7: Closed curve C which follows the fluid's velocity

Because the curve C in Figure 5.7 follows the fluid's velocity, one may express the velocity, $\mathbf{U} + d\mathbf{U}$, at $\mathbf{x} + d\mathbf{x}$ as the material derivative of $\mathbf{x} + d\mathbf{x}$:

$$\mathbf{U} + d\mathbf{U} = \frac{D}{Dt}(\mathbf{x} + d\mathbf{x}) = \frac{D\mathbf{x}}{Dt} + \frac{D}{Dt}(d\mathbf{x}) \quad (5.27)$$

By the same logic one has:

$$\mathbf{U} = \frac{D}{Dt}(\mathbf{x}) \quad (5.28)$$

Eqs. 5.27 and 5.28 can be combined to yield, in index notation:

$$dU_i = \frac{D}{Dt}(dx_i) \quad (5.29)$$

Eq. 5.29 can be substituted into the expression on the right-hand side of Eq. 5.23 to yield:

$$\int_C U_i \frac{D}{Dt}(dx_i) = \int_C U_i dU_i = \int_C d\left(\frac{1}{2}U_i^2\right) = 0 \quad (5.30)$$

The last equality in Eq. 5.30 follows because C is a closed curve.

At this point, Eq. 5.23 has been reduced to:

$$\frac{D\Gamma}{Dt} = \int_C \left(\frac{1}{\rho} \frac{\partial \sigma_{ij}}{\partial x_j} \right) \quad (5.31)$$

The term $\partial \sigma_{ij} / \partial x_j$ can be thought of as the net viscous force, and because one of the conditions for Kelvin's circulation theorem is that the fluid is not subject to net viscous forces, this term is also zero, leading to:

$$\frac{D\Gamma}{Dt} = 0 \quad (5.32)$$

Attention can now be turned to Helmholtz's vortex theorems. Given the same four conditions as for Kelvin's circulation theorem, Helmholtz's vortex theorems are:

1. The motion of the fluid's vortex lines follows the fluid's local velocity.
2. A vortex tube's strength remains the same as one traverses the length of the vortex tube.
3. Vortex tubes don't end in the interior of a fluid.
4. A vortex tube's strength does not change with time.

Discussions and/or proofs of Helmholtz’s Vortex Theorem #1 can be found in [33, 124, 125]. A proof of Helmholtz’s Vortex Theorem #2 can be found in [125]. A discussion about Helmholtz’s Vortex Theorem #3 can be found in [125]. A discussion of Helmholtz’s Vortex Theorem #4 can be found in [124] and a proof of Helmholtz’s Vortex Theorem #4 can be found in [125].

It will be seen that Helmholtz’s vortex theorems provide theoretical justification for the way in which the GFVS computes the motion of vortex tubes.

5.4 Velocity Field Calculation Utilized by the GVFS

Vortex methods, which are based upon the vorticity field, necessitate the use of a methodology which can reconstruct the velocity field from the vorticity field. The Helmholtz decomposition can accomplish just that and this section is devoted to first explaining the Helmholtz decomposition in an infinite domain and next detailing the Helmholtz decomposition for a simply connected domain which contains a solid boundary. Finally, this section extends the Helmholtz decomposition to incompressible flow. Unless otherwise noted, this section is based upon Bernard [107].

5.4.1 The Helmholtz Decomposition in an Infinite Domain

A discussion of the Helmholtz decomposition begins by expressing the negative of the velocity field $-\mathbf{U}(\mathbf{x})$ as the vector Laplacian of a vector field $\mathbf{B}(\mathbf{x})$ as in the following equation:

$$\nabla^2 \mathbf{B} = -\mathbf{U} \tag{5.33}$$

The unique solution to the Poisson equation² in Eq. 5.33 is given by

$$\mathbf{B}(\mathbf{x}) = \frac{1}{4\pi} \int_{\mathbb{R}^3} \frac{\mathbf{U}(\mathbf{y})}{|\mathbf{x} - \mathbf{y}|} d\mathbf{y} \tag{5.34}$$

²For a discussion relevant to the solution of Eq. 5.33 see Carrier and Pearson’s [118] chapter on Green’s Functions, Chapter 9.

Based upon \mathbf{B} , a scalar potential, Φ , and a vector potential $\mathbf{\Pi}$, can be defined as follows:

$$\Phi = -\nabla \cdot \mathbf{B} \quad (5.35)$$

$$\mathbf{\Pi} = \nabla \times \mathbf{B} \quad (5.36)$$

An expression of \mathbf{U} in terms of Φ and $\mathbf{\Pi}$ can be obtained by first starting with the identity:

$$\nabla^2 \mathbf{B} = \nabla(\nabla \cdot \mathbf{B}) - \nabla \times (\nabla \times \mathbf{B}) \quad (5.37)$$

Substituting Eqs. 5.33, 5.35, and 5.36 into Eq. 5.37 yields the desired expression for \mathbf{U} in terms of Φ and $\mathbf{\Pi}$:

$$\mathbf{U} = \nabla\Phi + \nabla \times \mathbf{\Pi} \quad (5.38)$$

It is worth noting that because \mathbf{B} is unique, so too are Φ and $\mathbf{\Pi}$. Eq. 5.38 can also be used to derive equations which involve $\nabla \cdot \mathbf{U}$ and the vorticity $\mathbf{\Omega}$ in the following way. Applying the divergence operator to Eq. 5.38 and using the vector identity $\nabla \cdot (\nabla \times \mathbf{F}) = 0$ for any generic vector, \mathbf{F} , one obtains:

$$\nabla^2 \Phi = \nabla \cdot \mathbf{U} \quad (5.39)$$

An expression relating $\mathbf{\Pi}$ to $\mathbf{\Omega}$ can be derived by first noting that, because $\mathbf{\Pi} = \nabla \times \mathbf{B}$ and $\nabla \cdot (\nabla \times \mathbf{F}) = 0$ for any generic vector, \mathbf{F} , $\nabla \cdot \mathbf{\Pi} = 0$. In addition, Eq. 5.37 applies with $\mathbf{\Pi}$ substituted for \mathbf{B} . Furthermore, the identity $\nabla \times \nabla S = 0$ is valid for any generic scalar, S . Using these ideas and taking the curl of Eq. 5.38 and applying the definition $\mathbf{\Omega} = \nabla \times \mathbf{U}$ one obtains:

$$\nabla^2 \mathbf{\Pi} = -\mathbf{\Omega} \quad (5.40)$$

Defining $\theta = \nabla \cdot \mathbf{U}$, the solution to Eq. 5.39 is:

$$\Phi(\mathbf{x}) = -\frac{1}{4\pi} \int_{\mathbb{R}^3} \frac{\theta(\mathbf{y})}{|\mathbf{x} - \mathbf{y}|} d\mathbf{y} \quad (5.41)$$

And, similarly, the solution to Eq.5.40 is:

$$\mathbf{\Pi}(\mathbf{x}) = \frac{1}{4\pi} \int_{\mathbb{R}^3} \frac{\mathbf{\Omega}(\mathbf{y})}{|\mathbf{x} - \mathbf{y}|} d\mathbf{y} \quad (5.42)$$

Finally, plugging Eqs. 5.41 and 5.42 into Eq. 5.38 and carrying out the appropriate derivatives on the right-hand side of this equation yields the expression for \mathbf{U} in terms of $\nabla \cdot \mathbf{U}$ and $\mathbf{\Omega}$ in an infinite domain:

$$\mathbf{U}(\mathbf{x}) = \frac{1}{4\pi} \int_{\mathbb{R}^3} \frac{\theta(\mathbf{y})(\mathbf{x} - \mathbf{y})}{|\mathbf{x} - \mathbf{y}|^3} d\mathbf{y} + \frac{1}{4\pi} \int_{\mathbb{R}^3} \frac{\mathbf{\Omega}(\mathbf{y}) \times (\mathbf{x} - \mathbf{y})}{|\mathbf{x} - \mathbf{y}|^3} d\mathbf{y} \quad (5.43)$$

5.4.2 The Helmholtz Decomposition in a Domain with a Solid Boundary

In a flow domain that borders on a solid boundary the Helmholtz decomposition as described in Eq. 5.43 in the previous section has to be altered in order to account for the fact that the component of the velocity normal to the boundary at the boundary must be zero (this condition can be referred to as the *non-penetration boundary condition* [62]). In addition, the following alterations to the Helmholtz decomposition apply to simply connected flow domains. For a domain to be classified as simply connected, it must be the case that any closed curve which lies within the domain can be shrunk to a point while continuing to remain within the domain. In the case of the step geometry in the present simulation, the domain surrounding the step is simply connected due to the fact that the dimensions of the step are finite in all directions, including the spanwise direction. With this arrangement, a closed curve which surrounds the step can still be shrunk to a point while remaining within the flow domain.

With these preliminaries spelled out, assume that the flow domain, D , contains a solid object (like, for instance, the step) with boundary ∂D . In addition, assume that $\theta = \nabla \cdot \mathbf{U}$ and $\boldsymbol{\Omega}$ are known within the domain D and that the velocity normal to boundary on ∂D :

$$U_n = \mathbf{U} \cdot \hat{\mathbf{n}}|_{\partial D} \quad (5.44)$$

is known (if the non-penetration boundary condition holds, as is the case in the present step flow simulation, then $U_n = 0$). If the flow domain D , which partly borders on a solid boundary, extends out to infinity, then the integrals in Eqs. 5.41 and 5.42 are still well-defined if the region of integration is changed to D and the integrand goes to zero at infinity, as would be the case in incompressible flow over a step because $\theta = \nabla \cdot \mathbf{U} = 0$ (incompressibility) and the spatial gradients in velocity go to zero far removed from the influence of a solid boundary, $\boldsymbol{\Omega}(\mathbf{x} \rightarrow \infty) = 0$. If the integrals in Eqs. 5.41 and 5.42 are still well-defined when their regions of integration are changed to D , then Eq. 5.43 remains valid if the region of integration is changed from \mathfrak{R}^3 to D . However, the velocity field in Eq. 5.43 (with the region of integration changed from \mathfrak{R}^3 to D) will not conform to the boundary condition which specifies the normal velocity on the solid boundary, Eq. 5.44. In order to account for the boundary condition in Eq. 5.44 an extra term, $\boldsymbol{\Gamma}$ can be added to Eq. 5.38,

as follows:

$$\mathbf{U} = \nabla\Phi + \nabla \times \mathbf{\Pi} + \mathbf{\Gamma} \quad (5.45)$$

Applying the divergence operator to Eq. 5.45, using the fact that $\nabla^2\Phi = \nabla \cdot \mathbf{U}$ and $\nabla \cdot (\nabla \times \mathbf{F}) = 0$ for any generic vector, \mathbf{F} , and rearranging yields:

$$\nabla \cdot \mathbf{\Gamma} = 0 \quad (5.46)$$

Applying the curl operator to Eq. 5.45 and using the fact that $\nabla \times \nabla S = 0$, for any generic scalar, S , yields:

$$\nabla \times \mathbf{U} = \nabla \times (\nabla \times \mathbf{\Pi}) + \nabla \times \mathbf{\Gamma} \quad (5.47)$$

Then, using Eq. 5.37 with \mathbf{B} replaced by $\mathbf{\Pi}$ along with the fact that $\nabla \cdot \mathbf{\Pi} = 0$, and Eq. 5.40 along with the fact that $\mathbf{\Omega} = \nabla \times \mathbf{U}$, in Eq. 5.47 and rearranging yields:

$$\nabla \times \mathbf{\Gamma} = 0 \quad (5.48)$$

It is important to keep in mind that $\mathbf{\Gamma}$ must conform to the boundary condition on U_n , namely Eq. 5.44. In order to achieve this requirement, substitute Eq. 5.45 into Eq. 5.44 and rearrange to yield another condition on $\mathbf{\Gamma}$:

$$(\mathbf{\Gamma} \cdot \hat{\mathbf{n}})|_{\partial D} = (U_n - \nabla\Phi \cdot \hat{\mathbf{n}} - (\nabla \times \mathbf{\Pi}) \cdot \hat{\mathbf{n}})|_{\partial D} \quad (5.49)$$

Because $\mathbf{\Gamma}$ satisfies Eq. 5.48, there exists a scalar function, ϕ , such that

$$\mathbf{\Gamma} = \nabla\phi \quad (5.50)$$

Plugging Eq. 5.50 into Eq. 5.46 yields the Laplace equation for ϕ :

$$\nabla^2\phi = 0 \quad (5.51)$$

Plugging Eq. 5.50 into Eq. 5.49 and defining the directional derivative on the boundary ∂D as $\frac{d\phi}{dn} = (\nabla\phi \cdot \hat{\mathbf{n}})|_{\partial D}$, yields a boundary condition for ϕ on ∂D :

$$\frac{d\phi}{dn} = U_n - \frac{d\Phi}{dn} - (\nabla \times \mathbf{\Pi}) \cdot \hat{\mathbf{n}} \quad (5.52)$$

Putting together the above discussion, the velocity field in a domain D with a solid boundary ∂D can be expressed as

$$\mathbf{U} = \nabla\Phi + \nabla \times \mathbf{\Pi} + \nabla\phi \quad (5.53)$$

in D , with Φ and $\mathbf{\Pi}$ given by:

$$\Phi(\mathbf{x}) = -\frac{1}{4\pi} \int_D \frac{\theta(\mathbf{y})}{|\mathbf{x} - \mathbf{y}|} d\mathbf{y} \quad (5.54)$$

$$\mathbf{\Pi}(\mathbf{x}) = \frac{1}{4\pi} \int_D \frac{\mathbf{\Omega}(\mathbf{y})}{|\mathbf{x} - \mathbf{y}|} d\mathbf{y} \quad (5.55)$$

and ϕ given by the solution to:

$$\nabla^2 \phi = 0 \quad (5.56)$$

in D subject to the following boundary condition on ∂D :

$$\frac{d\phi}{dn} = U_n - \frac{d\Phi}{dn} - (\nabla \times \mathbf{\Pi}) \cdot \hat{\mathbf{n}} \quad (5.57)$$

5.4.3 The Helmholtz Decomposition in a Domain with a Solid Boundary Extended to Incompressible Flow

Eqs. 5.53-5.57 provide a means for expressing the velocity field in a flow domain with a solid boundary (e.g. flow over a step) in terms of the divergence of the velocity field, θ , the vorticity field, $\mathbf{\Omega}$, and a scalar potential, ϕ . In incompressible flow $\nabla \cdot \mathbf{U} = 0$, in which case, from Eq. 5.54, $\Phi = 0$. Eqs. 5.53-5.57 then reduce to

$$\mathbf{U} = \nabla \times \mathbf{\Pi} + \nabla \phi \quad (5.58)$$

in D , with $\mathbf{\Pi}$ given by

$$\mathbf{\Pi}(\mathbf{x}) = \frac{1}{4\pi} \int_D \frac{\mathbf{\Omega}(\mathbf{y})}{|\mathbf{x} - \mathbf{y}|} d\mathbf{y} \quad (5.59)$$

and ϕ given by the solution to:

$$\nabla^2 \phi = 0 \quad (5.60)$$

in D subject to the following boundary condition on ∂D :

$$\frac{d\phi}{dn} = U_n - (\nabla \times \mathbf{\Pi}) \cdot \hat{\mathbf{n}} \quad (5.61)$$

With a given vorticity field, $\mathbf{\Pi}$ can be evaluated on the boundary ∂D through the use of Eq. 5.59. In this way the velocity field can be reconstructed from a known vorticity field and a scalar potential ϕ which satisfies the Laplace equation subject to the boundary condition in Eq. 5.61.

Section 5.6 details the computations involved in the calculation of the velocity and as a first step in this direction it is helpful to define:

$$\mathbf{U}_{\Pi} = \nabla \times \mathbf{\Pi} \quad (5.62)$$

$$\mathbf{U}_{\phi} = \nabla \phi \quad (5.63)$$

so that Eq. 5.58 can be written as:

$$\mathbf{U} = \mathbf{U}_{\Pi} + \mathbf{U}_{\phi} \quad (5.64)$$

Taking the curl in Eq. 5.62 by utilizing Eq. 5.59 yields:

$$\mathbf{U}_{\Pi} = -\frac{1}{4\pi} \int_D \frac{(\mathbf{x} - \mathbf{y}) \times \mathbf{\Omega}(\mathbf{y})}{|\mathbf{x} - \mathbf{y}|^3} d\mathbf{y} \quad (5.65)$$

Eq. 5.65 is a form of the *Biot-Savart Law*.

5.5 Vortex Stretching and Reorientation

This section discusses the phenomenon of vortex stretching and reorientation, a process which is intertwined with vortex methods. Unless otherwise noted, this section is based upon [31].

To start out the discussion in this section, it is helpful to define turbulent kinetic energy. Breaking up the velocity field, \mathbf{U} , into an average, $\overline{\mathbf{U}}$, and fluctuating, \mathbf{u}' , component as in:

$$\mathbf{U} = \overline{\mathbf{U}} + \mathbf{u}' \quad (5.66)$$

the turbulent kinetic energy, K , is

$$K = \frac{1}{2} \overline{\rho u'_i u'_i} \quad (5.67)$$

In addition, it is helpful to realize that a spectral analysis of a fluid's dynamics can yield valuable insights into how the turbulent kinetic energy of a fluid is distributed throughout different length scales and how this distribution

changes in time. In order to expand upon this statement, it is necessary to first define some quantities related to the turbulent kinetic energy in spectral space. Defining $E_{ii}(\mathbf{k}, t)$ as the turbulent kinetic energy density in wavenumber space as:

$$E_{ii}(\mathbf{k}, t) = \frac{1}{(2\pi)^3} \int_{\mathbb{R}^3} e^{i\mathbf{r}\cdot\mathbf{k}} \overline{u'_i(\mathbf{x}, t) u'_i(\mathbf{x} + \mathbf{r}, t)} d\mathbf{r} \quad (5.68)$$

with \mathbf{k} the wavenumber vector, t time, \mathbf{x} a point in physical space, and \mathbf{r} a displacement in physical space, can lead to an expression of the turbulent kinetic energy as:

$$K(t) = \frac{1}{2} \int_{\mathbb{R}^3} E_{ii}(\mathbf{k}, t) d\mathbf{k} = \int_0^\infty dk \left[\frac{1}{2} \int_{|\mathbf{k}|=k} d\Omega E_{ii}(\mathbf{k}, t) \right] \quad (5.69)$$

with $k = |\mathbf{k}|$, and $d\Omega$ a solid angle in \mathbf{k} -space such that $d\mathbf{k} = d\Omega dk$. $E_{ii}(\mathbf{k}, t)$ can also be used to define the energy spectrum, $E(k, t)$, as:

$$E(k, t) = \frac{1}{2} \int_{|\mathbf{k}|=k} E_{ii}(\mathbf{k}, t) d\Omega \quad (5.70)$$

so that

$$K(t) = \int_0^\infty E(k, t) dk \quad (5.71)$$

and $E(k, t)$ describes how the turbulent kinetic energy varies over the different length scales in a fluid.

With these definitions in mind, it is the case that the turbulent kinetic energy of a fluid tends to reside in length scales larger than the length scales at which the fluid's turbulent kinetic energy is dissipated by the action of viscosity. This is illustrated in Figure 5.8.

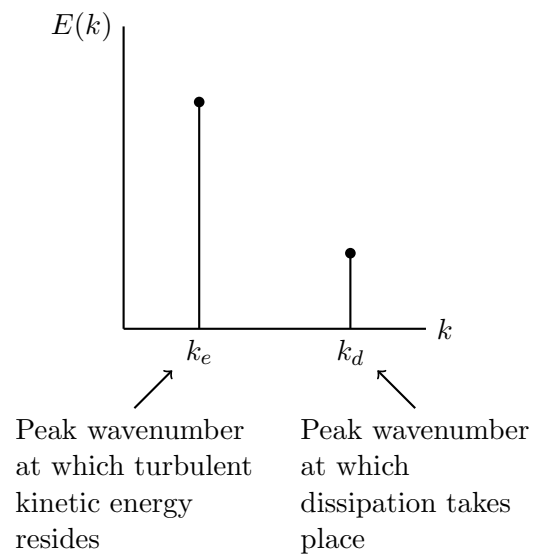


Figure 5.8: Peak wavenumbers at which turbulent kinetic energy and turbulent kinetic energy dissipation reside. Based upon [31].

In Figure 5.8, one may think of the wavenumbers k_e and k_d as representative of regions of rotational fluid motion of length scales $l_e = 1/k_e$ and $l_d = 1/k_d$ respectively. Given that $k_d > k_e$, that implies that $l_e > l_d$, which says that the turbulent kinetic energy of a fluid tends to reside in regions of rotational motion of a length scale larger than the length scale of the regions of rotational motion at which turbulent kinetic energy is dissipated by viscosity. It is also noteworthy that if the Reynolds number of a flow is large enough, there exists a range of wavenumbers between k_e and k_d at which turbulent kinetic energy tends not to reside or be dissipated. This range of wavenumbers is called the inertial subrange.

Given that the wavenumber at which turbulent kinetic energy tends to reside is different than the wavenumber at which dissipation tends to take place, one may wonder how turbulent kinetic energy is transported from the larger, turbulent kinetic energy-containing length scales to the smaller, turbulent kinetic energy-dissipating length scales. This process of the transport of turbulent kinetic energy to smaller length scales is accomplished through vortex stretching and reorientation. It is important to note that, while the net movement of energy is to the smaller length scales, there is movement of energy in the opposite direction, that is, from smaller to larger length scales. The movement of energy from smaller to larger length scales is called backscatter.

The phenomenon of vortex stretching and reorientation may be explained by analyzing the vorticity equation. The vorticity equation in dimensional form is:

$$\frac{\partial \Omega_i}{\partial t} + U_j \frac{\partial \Omega_i}{\partial x_j} = \Omega_j \frac{\partial U_i}{\partial x_j} + \nu \nabla^2 \Omega_i \quad (5.72)$$

Eq. 5.72 may be re-stated using the material derivative as:

$$\frac{D\Omega_i}{Dt} = \Omega_j \frac{\partial U_i}{\partial x_j} + \nu \nabla^2 \Omega_i \quad (5.73)$$

Eq. 5.73 may be interpreted to mean that the rate of change of the vorticity of a fluid particle as it moves is governed by vortex stretching and reorientation, as given by the first term on the right-hand side of Eq. 5.73, and the diffusion of vorticity by viscosity, as given by the second term on the right-hand side of Eq. 5.73.

It is instructive to examine the vortex stretching term, $\Omega_j \partial U_i / \partial x_j$, in more detail. To do this, it is helpful to start out by examining a fluid line

element of small length with two material endpoints. This is illustrated in Figure 5.9.

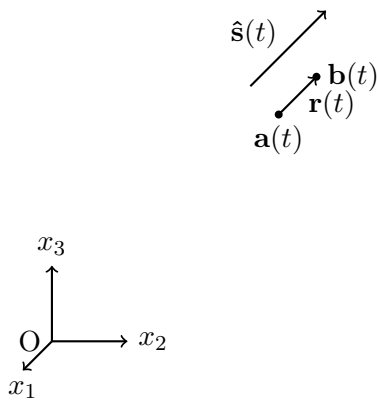


Figure 5.9: A small fluid line element with material endpoints

In Figure 5.9, the material endpoints $\mathbf{a}(t)$ and $\mathbf{b}(t)$ are separated by the vector $\mathbf{r}(t)$ so that

$$\mathbf{r}(t) = \mathbf{b}(t) - \mathbf{a}(t) \quad (5.74)$$

If $l(t) = |\mathbf{r}(t)|$, then a unit vector in the direction of $\mathbf{r}(t)$ is

$$\hat{\mathbf{s}}(t) = \frac{\mathbf{r}(t)}{|\mathbf{r}(t)|} \quad (5.75)$$

With these definitions, one has

$$\mathbf{r}(t) = l(t)\hat{\mathbf{s}}(t) \quad (5.76)$$

Because \mathbf{a} is a material point, one can obtain the differential equation

$$\frac{d\mathbf{a}}{dt} = \mathbf{U}(\mathbf{a}(t), t) \quad (5.77)$$

One may solve Eq. 5.77 for $\mathbf{a}(t)$ as

$$\mathbf{a}(t) = \mathbf{a}(0) + \int_0^t \mathbf{U}(\mathbf{a}(t'), t') dt' \quad (5.78)$$

By examining the movement of \mathbf{a} in a small time Δt , one can approximately say

$$\mathbf{a}(\Delta t) = \mathbf{a}(0) + \mathbf{U}(\mathbf{a}(0), 0)\Delta t \quad (5.79)$$

In the same vein, one may write for \mathbf{b}

$$\mathbf{b}(\Delta t) = \mathbf{b}(0) + \mathbf{U}(\mathbf{b}(0), 0)\Delta t \quad (5.80)$$

One may also derive from Eq. 5.74 evaluated at $t = 0$ that

$$\mathbf{b}(0) = \mathbf{a}(0) + \mathbf{r}(0) \quad (5.81)$$

In addition, because $l(0)$ is a small number, one may use a Taylor series expansion to obtain an expression for $\mathbf{U}(\mathbf{b}(0), 0)$ as

$$\mathbf{U}(\mathbf{b}(0), 0) = \mathbf{U}(\mathbf{a}(0), 0) + (\nabla\mathbf{U})\mathbf{r}(0) \quad (5.82)$$

Putting Eq. 5.82 into Eq. 5.80 yields

$$\mathbf{b}(\Delta t) = \mathbf{b}(0) + \left(\mathbf{U}(\mathbf{a}(0), 0) + (\nabla\mathbf{U})\mathbf{r}(0) \right) \Delta t \quad (5.83)$$

Subtracting Eq. 5.79 from Eq. 5.83 and simplifying and rearranging yields

$$\mathbf{b}(\Delta t) - \mathbf{a}(\Delta t) = \mathbf{b}(0) - \mathbf{a}(0) + (\nabla \mathbf{U})\mathbf{r}(0)\Delta t \quad (5.84)$$

Using Eq. 5.74, Eq. 5.84 may be re-written as

$$\mathbf{r}(\Delta t) = \mathbf{r}(0) + (\nabla \mathbf{U})\mathbf{r}(0)\Delta t \quad (5.85)$$

Using Eq. 5.76 in Eq. 5.85 yields

$$l(\Delta t)\hat{\mathbf{s}}(\Delta t) = l(0)\hat{\mathbf{s}}(0) + (\nabla \mathbf{U})l(0)\hat{\mathbf{s}}(0)\Delta t \quad (5.86)$$

Dividing Eq. 5.86 by $l(\Delta t)\Delta t$ [107] yields

$$\frac{\hat{\mathbf{s}}(\Delta t)}{\Delta t} = \frac{l(0)}{l(\Delta t)} \frac{\hat{\mathbf{s}}(0)}{\Delta t} + \frac{l(0)}{l(\Delta t)} (\nabla \mathbf{U})\hat{\mathbf{s}}(0) \quad (5.87)$$

Adding $-\hat{\mathbf{s}}(0)/\Delta t$ to both sides of Eq. 5.87 [107] yields

$$\frac{\hat{\mathbf{s}}(\Delta t)}{\Delta t} - \frac{\hat{\mathbf{s}}(0)}{\Delta t} = \frac{l(0)}{l(\Delta t)} \frac{\hat{\mathbf{s}}(0)}{\Delta t} - \frac{\hat{\mathbf{s}}(0)}{\Delta t} + \frac{l(0)}{l(\Delta t)} (\nabla \mathbf{U})\hat{\mathbf{s}}(0) \quad (5.88)$$

Rearranging the terms in Eq. 5.88 [107] yields

$$\frac{\hat{\mathbf{s}}(\Delta t) - \hat{\mathbf{s}}(0)}{\Delta t} = -\frac{\hat{\mathbf{s}}(0)}{l(\Delta t)} \left(\frac{l(\Delta t) - l(0)}{\Delta t} \right) + \frac{l(0)}{l(\Delta t)} (\nabla \mathbf{U})\hat{\mathbf{s}}(0) \quad (5.89)$$

Taking the limit of Eq. 5.89 as $\Delta t \rightarrow 0$ and rearranging yields

$$\frac{d\hat{\mathbf{s}}}{dt} + \frac{1}{l} \frac{dl}{dt} \hat{\mathbf{s}} = (\nabla \mathbf{U})\hat{\mathbf{s}} \quad (5.90)$$

Eq. 5.90 can be used to understand the vortex stretching term.

First, note that, because $\hat{\mathbf{s}}$ is a unit vector, which means that $\hat{\mathbf{s}} \cdot \hat{\mathbf{s}} = 1$, one may form the following equation

$$\hat{\mathbf{s}} \cdot \frac{d\hat{\mathbf{s}}}{dt} = \frac{1}{2} \frac{d(\hat{\mathbf{s}} \cdot \hat{\mathbf{s}})}{dt} = \frac{1}{2} \frac{d(1)}{dt} = 0 \quad (5.91)$$

Eq. 5.91 means that $d\hat{\mathbf{s}}/dt$, which signifies how the direction of \mathbf{r} changes in time, lies perpendicular to the direction of \mathbf{r} . To see how the above derivations lead to an understanding of the vortex stretching term, $\Omega_j \frac{\partial U_i}{\partial x_j}$, consider

a case in which \mathbf{s} lies in the same direction as the local vorticity vector, $\boldsymbol{\Omega}$, in which case

$$\hat{\mathbf{s}} = \boldsymbol{\Omega}/|\boldsymbol{\Omega}| \quad (5.92)$$

Plugging Eq. 5.92 into Eq. 5.90, multiplying the resulting equation by $|\boldsymbol{\Omega}|$, and switching to index notation yields

$$\Omega_j \frac{\partial U_i}{\partial x_j} = \frac{1}{l} \frac{dl}{dt} \Omega_i + |\boldsymbol{\Omega}| \frac{d(\Omega_i/|\boldsymbol{\Omega}|)}{dt} \quad (5.93)$$

Given Eq. 5.73, which expresses the rate of change of the vorticity of a material fluid particle as the sum of the vortex stretching term and diffusive effects, one may think of Eq. 5.93 as contributing to the increase or decrease of the vorticity of a material fluid particle as it moves around the flow domain. The first term on the right-hand side of Eq. 5.93 may be thought of as enhancing or diminishing the vorticity of a material fluid particle due to the stretching, or contracting, of a fluid line element with material endpoints. If the fluid line element is stretching, then, to use the terminology defined in Figure 5.9 in conjunction with Eq. 5.76, $dl/dt > 0$ and the first term on the right-hand side of Eq. 5.93 serves to enhance the vorticity of a material fluid particle, while if the fluid line element is contracting, $dl/dt < 0$ and the first-term on the right-hand side of Eq. 5.93 serves to diminish the vorticity of a material fluid particle.

The second term on the right-hand side of Eq. 5.93 changes the vorticity of a material fluid particle by changing the direction of its vorticity, not its magnitude. An example can help explain this effect. Suppose, using the terminology defined in Figure 5.9, \mathbf{s} lies in the $x_1 - x_2$ plane oriented in the positive x_1 direction, and the local vorticity vector is also oriented in the positive x_1 direction, making Eq. 5.92 valid. Figure 5.10 illustrates this setup.

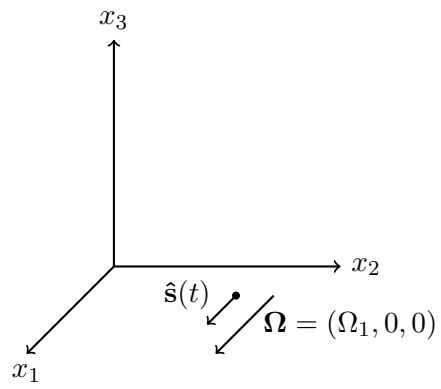


Figure 5.10: A small fluid line element and local vorticity vector oriented in the positive x_1 direction

In this case, Eq. 5.73 in the x_1 direction comes out to be:

$$\frac{D\Omega_1}{Dt} = \Omega_1 \frac{\partial U_1}{\partial x_1} + \nu \nabla^2 \Omega_1 \quad (5.94)$$

The first term on the right-hand side of Eq. 5.94 represents an increase or decrease of Ω_1 by stretching or compression. Eq. 5.73 in the x_2 direction is

$$\frac{D\Omega_2}{Dt} = \Omega_1 \frac{\partial U_2}{\partial x_1} + \nu \nabla^2 \Omega_2 \quad (5.95)$$

and Eq. 5.73 in the x_3 direction is

$$\frac{D\Omega_3}{Dt} = \Omega_1 \frac{\partial U_3}{\partial x_1} + \nu \nabla^2 \Omega_3 \quad (5.96)$$

The first terms on the right-hand sides of Eqs. 5.95 and 5.96 stand for Ω_1 turned to the x_2 and x_3 directions respectively by shearing motions generated by differences in velocity in the x_1 direction. These terms come from the second term on the right-hand side of Eq. 5.93, which represents the vorticity component Ω_i being turned in a direction perpendicular to the i direction. Figure 5.11a and 5.11b illustrate the turning of Ω_1 towards the x_2 and x_3 directions respectively by shearing motions generated by differences in velocity in the x_1 direction.

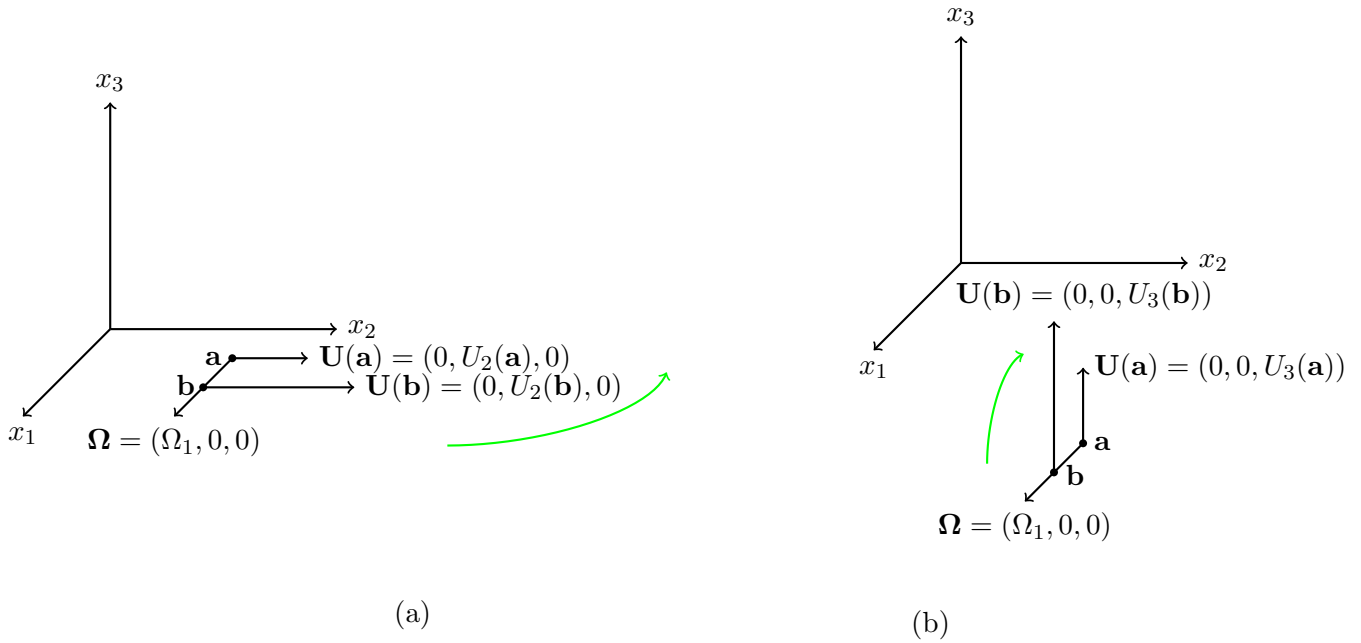


Figure 5.11: Shearing motions caused by velocity variations in the x_1 direction turning Ω_1 : (a) U_2 velocity variation along the x_1 direction turning Ω_1 toward the x_2 direction (b) U_3 velocity variation along the x_1 direction turning Ω_1 toward the x_3 direction

It is important to note that in a region in which Helmholtz's vortex theorems apply and the fluid is incompressible, the length of vortex lines will, on average, increase [131]. This attribute leads to the formation of vortex loops, as discussed in Section 5.8.

5.6 GVFS Calculation of Velocity

This section describes how the GVFS calculates the fluid's velocity. The GVFS calculates the fluid's velocity by utilizing the breakdown of the velocity field as in Eqs. 5.58-5.61. \mathbf{U}_Π is calculated by summing the velocity induced by the vorticity represented by the vortex tubes and the vorticity contained within the triangular prisms of the near-wall mesh via approximations to the Biot-Savart law [61]. The Biot-Savart law is adapted to represent the velocity induced by the i th vortex tube at a point \mathbf{x} in the flow, $\mathbf{U}_{\Pi,i}(\mathbf{x})$ as

$$\mathbf{U}_{\Pi,i}(\mathbf{x}) = -\frac{1}{4\pi} \frac{\mathbf{r}_i \times \mathbf{s}_i}{|\mathbf{r}_i|^3} \Gamma_i \cdot \gamma(|\mathbf{r}_i|/\sigma) \quad (5.97)$$

In Eq. 5.97, $\mathbf{s}_i = \mathbf{x}_i^2 - \mathbf{x}_i^1$ represents the length and direction (oriented along the direction of the local vorticity) of the i th vortex tube with endpoints \mathbf{x}_i^1 and \mathbf{x}_i^2 , $\mathbf{x}_i = (\mathbf{x}_i^1 + \mathbf{x}_i^2)/2$ is the midpoint of the i th vortex tube, $\mathbf{r}_i = \mathbf{x} - \mathbf{x}_i$, and Γ_i is the circulation of the i th vortex tube. γ is a function which serves the purpose of smoothing the induced velocity from the vortex tube [61] and compensates for the fact that the GVFS considers the vortex tubes to just be lines as opposed to having a finite cross-section. $\gamma(|\mathbf{r}_i|/\sigma)$ is defined as

$$\gamma(|\mathbf{r}_i|/\sigma) = 1 - \left(1 - \frac{3}{2}(|\mathbf{r}_i|/\sigma)^3\right)e^{-(|\mathbf{r}_i|/\sigma)^3} \quad (5.98)$$

with σ as a parameter affecting the distance in which smoothing takes place. Figure 5.12 plots Eq. 5.98 with $r_i = |\mathbf{r}_i|$.

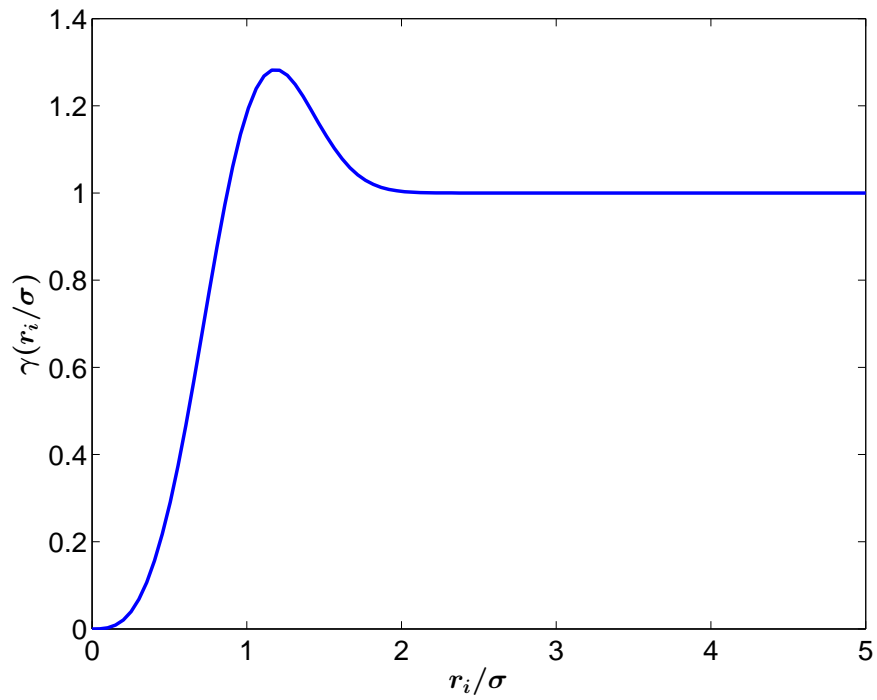


Figure 5.12: A graphical representation of Eq. 5.98.

Figure 5.13 illustrates what the velocity field which a vortex tube, in isolation, would induce according to Eq. 5.97.

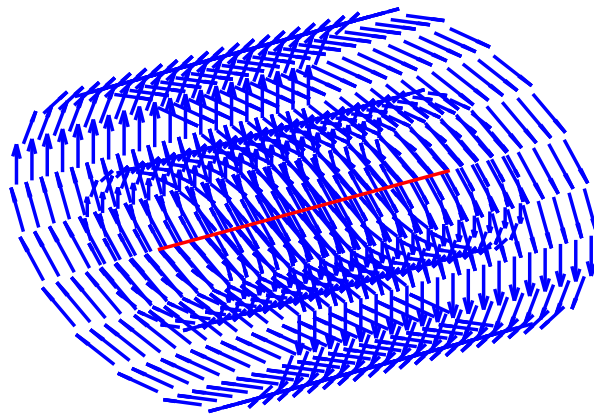


Figure 5.13: Velocity field (indicated by blue vectors) induced by an isolated vortex tube (in red)

Figure 5.13 illustrates that, in isolation, a vortex tube induces around it a little region of rotational motion.

In Eq. 5.97, $\Gamma \mathbf{s}$ approximately plays the same role that $\boldsymbol{\Omega}(\mathbf{y}, t) \mathbf{d}\mathbf{y}$ plays in the Biot-Savart Law, Eq. 5.65, and so one may think of Eq. 5.16 as determining a translation between the vorticity in a vortex tube and the vorticity in a prism for the purposes of evaluating the velocity of the fluid at a point far away from the tube/prism where the local effects due to the difference in shape between a tube and prism are negligible.

For the flows that the GVFS simulates, it is assumed that the Reynolds number, which can be considered to be the ratio of inertia to viscous forces, is large enough so that away from the solid boundaries the fluid is not subject to the effects of net viscous forces [63]. And so, in accordance with Helmholtz vortex theorem #1, the endpoints of the vortex tubes convect with the local fluid velocity. In this way, the motion of the vortex tubes efficiently represents the phenomenon of vortex stretching and reorientation [31] as discussed in Section 5.5. And because of Helmholtz vortex theorems #2 and #4, each vortex tube is assumed to have one circulation which does not change with time. But, as the vortex tubes stretch past a pre-defined length they are subdivided forming new, smaller vortex tubes. All of the vortex tubes created from an original vortex tube inserted into the flow at the top of the wall-adjacent mesh form a *vortex filament*. All the vortex tubes on the same vortex filament have equal circulation [63]. Figure 5.14 illustrates the evolution of a vortex filament from an original vortex tube inserted into the flow at the top of the wall-adjacent mesh to a connection of several vortex tubes.

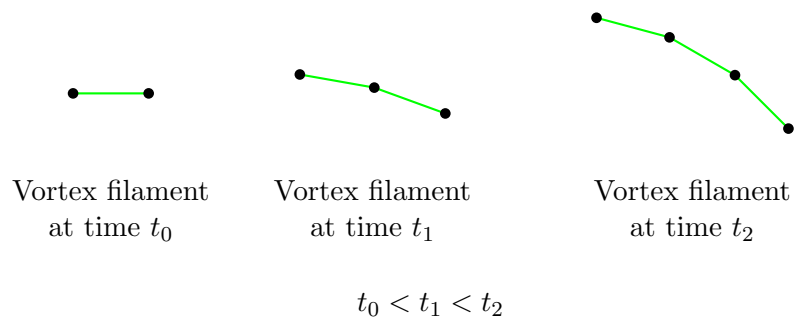


Figure 5.14: Evolution of a vortex filament in time

By breaking up a vortex filament into component vortex tubes, the GVFS simulates the phenomenon of vortex loop formation, a phenomenon which plays an integral part in the functioning of the GVFS (see Section 5.8).

It is important to point out that the contributions to the velocity field that the prisms in the near-wall mesh make differ depending on whether the point where the velocity is to be evaluated is near to or further away from the prism in question. At velocity field evaluation points outside of a radius on the order of the average edge length of the surface triangularization, a given prism adds to the velocity field as if it were a vortex tube with a strength found from Eq. 5.16. At velocity field evaluation points inside the radius mentioned in the previous sentence, a given prism adds to the velocity field through an evaluation of the integral in the Biot-Savart Law tailored to the layout of the near-wall mesh.

In the GVFS, \mathbf{U}_ϕ in the Helmholtz decomposition of the velocity field, Eq. 5.64, is obtained by first solving Eq. 5.60 subject to the boundary condition in Eq. 5.61. Because the boundary condition in Eq. 5.61 depends on \mathbf{U}_Π , at each large time step Δt^* , \mathbf{U}_Π must first be calculated by using appropriate approximations to the Biot-Savart Law as described above. ϕ in Eq. 5.60 is derived from a boundary element scheme as detailed in [108]. Part of the numerical implementation of the method outlined in [108] that the GVFS uses is detailed in [109].

In practice, the GVFS evaluates the velocity field using a fast multipole method³ based upon [110]. Using a fast multipole method to evaluate the velocity field significantly reduces the computational cost of updating the GVFS from time step to time step. This is the case because the velocities at the endpoints of all of the vortex tubes must be known in order to convect them with the local fluid velocity. Since each vortex tube contributes to the evaluation of every point in the fluid via the Biot-Savart Law, a direct calculation of the fluid's velocity at all of the endpoints of the vortex tubes would be $\mathcal{O}(N^2)$, with N the number of vortex tubes in the simulation. As previously mentioned in this paragraph, by using instead a fast multipole method to calculate the fluid's velocity, the computational cost of the GVFS is significantly reduced.

³For a description of the underlying fundamentals of multipole methods, see [111].

5.7 Violation of the Divergence-Free Condition of the Vorticity Field at the Vortex Filament Endpoints

In the simulations conducted by the GVFS the vorticity field does not have zero divergence where the vortex filaments end in the flow. One can adjust a vortex filament method so that zero divergence is kept at the ends of the vortex filaments [61], but it does not seem that this extra effort is worth its computational cost [112]. It is noteworthy that even though the vorticity field that the GVFS simulates does not have zero divergence where the vortex filaments end in the flow, the GVFS generates a Blasius boundary layer in laminar flow over a flat plate and “qualitative agreement with a log-type law” in the turbulent flow over a flat plate [62].

5.8 Vortex Loop Formation

By inspecting Eq. 5.97 one may observe that, if vortex tubes remained straight as they stretched, the kinetic energy due to the fluid motion induced by the vortex tubes would violate the conservation of energy principle due to increases in s and the constancy of Γ . The formation of vortex loops as the vortex lines stretch helps to conserve energy [131]. One way to understand the concept of vortex loop formation [123] is as follows: Consider Figure 5.15, which displays a vortex filament composed of vortex tubes forming an approximate loop.

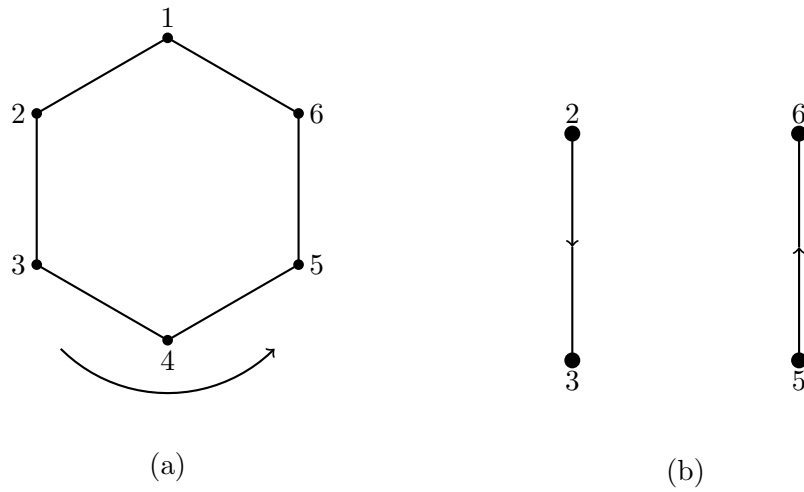


Figure 5.15: Vortex loop: (a) Vortex filament composed of tubes in the shape of a loop. ● denotes vortex tube endpoints. Arrow denotes orientation of vorticity along the vortex loop (b) Two vortex tubes opposite one another in (a) with orientation of vorticity along each tube indicated

Because the vortex tubes in Figure 5.15b are oppositely oriented, the resultant far-field velocities they induce, in accordance with Eq. 5.97, approximately cancel. This effect occurs for the other pairs of vortex tubes on opposite sides of the loop in Figure 5.15a. In this way, the formation of loops as the vortex stretching process takes place helps to insure the boundedness of energy within a fluid.

5.9 Vortex Filament Removal in the GVFS

If vortex tubes were tracked in a vortex filament simulation all the way to the point where they brought energy down to the dissipative scales of the flow, the number of vortex tubes in the simulation would become very costly from a computational perspective [63]. In order to get around this problem, vortex filaments that form approximate loops (see Section 5.8) are removed from the calculation at every time step. Chorin [113] showed that hairpin removal in a particular vortex method kept that computation at computationally acceptable levels. Bernard [114] applied the GVFS to the simulation of a turbulent puff. He demonstrated that vortex loop removal significantly reduced the computational cost of the GVFS's simulation of the turbulent puff. In addition, Bernard demonstrated that employing vortex loop removal did not significantly impact the correctness of the basic physics of the simulation.

When using the GVFS to simulate flow over a flat plate, another way in which the number of vortex tubes in the flow is decreased is by removing vortex filaments from the computation when they pass a downstream boundary. A region just upstream of this downstream boundary is then not available for analysis [63]. In addition, vortex filaments are removed from the computation when they cross into a solid boundary.

So to sum up, when the GVFS simulates flow over a flat plate, vortex tubes enter the calculation at the top of the wall-adjacent mesh and through vortex stretching and leave the calculation through vortex loop removal, the crossing of vortex filaments past a downstream boundary, and the crossing of vortex filaments into a solid boundary. When running the GVFS forward in time, the simulation eventually reaches an equilibrium in which the number of vortex tubes and filaments stay approximately constant in time. Flow statistics may then be obtained by appropriate time averages through the equilibrium region [62].

5.10 Some Advantages of Vortex Filament Methods

Large eddy simulations (LES) of fluid flow actually simulate the larger length scales in a flow simulation, but do not explicitly simulate the smaller length scales in a flow simulation. Instead, the effects of the smaller length scales upon the larger length scales are modeled [31]. Because the GVFS uses the vortex loop removal algorithm which insures that the dynamics of the smallest length scales of the fluid do not have to be tracked [63], it can be considered to be an LES [62]. One advantage of vortex filament methods with vortex loop removal as opposed to some other LES methods is that the phenomenon of backscatter is not obstructed [112].

LES methods which utilize grids can be subject to numerical dissipation⁴ which can interfere with the results of the simulation [116, 117]. Another advantage of vortex filament methods is that, away from the immediate vicinity of solid boundaries, they experience very little numerical dissipation due to the fact that vortex filament methods do not use a grid away from solid boundaries [62, 112].

5.11 Rough Flowchart of the GVFS

To sum up, Figure 5.16 displays a rough flowchart of the GVFS. This flowchart covers the activities of the GVFS during one large time step Δt^* .

⁴For a discussion of numerical dissipation, see Chapter 11 in [115].

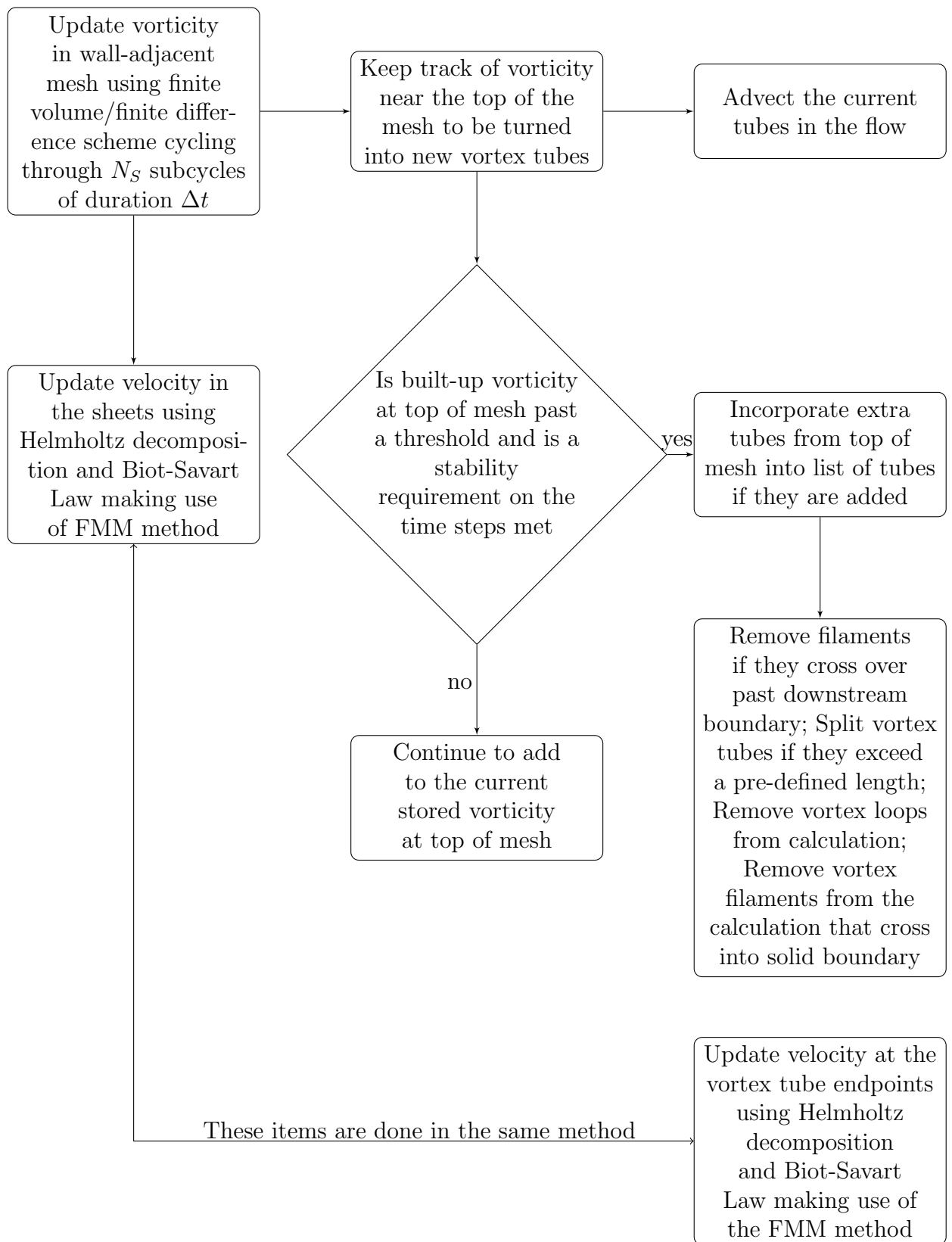


Figure 5.16: Rough flowchart for the GVFS. This flowchart covers the activities of the GVFS during one large time step Δt^* .

Chapter 6

Structural Aspects of Transitioning Boundary Layers

This chapter of the thesis describes some of the insights that were gained by using the GVFS to simulate transitioning boundary layers over a flat plate, and, in so doing, attempts to illustrate how vortex methods can be used to illuminate the structural development of a fluid.

6.1 Vortex Furrows

Bernard [63] utilized the GVFS to study, in part, transitioning boundary layers over a flat plate. The GVFS generated a Klebanoff-type transition. Klebanoff transitions possess, amongst other things, Ω -vortices [70], which presumably are entities in a fluid with axes which look like the Greek letter Ω . In addition, in Klebanoff transitions, low-speed fluid is moved out towards the free-stream in the wall-normal direction [70].

Bernard [63, 66] maintained that vortical structures cannot be defined as consisting of regions of rotational motion. Instead, Bernard argued that vortical structures can be identified only by considering all of the vorticity within a fluid, not just that vorticity responsible for rotational motion. Because the GVFS tracks the movement of vortex filaments around the flow, it is well-suited to identifying vortical structures according to this new definition.

By utilizing this new definition of vortical structure and the GVFS, Bernard [63] identified the vortex furrow as the main structure in Klebanoff-

type transitioning boundary layers. Vortex furrows are streamwise-elongated ‘bumps’ in the vortex sheets which form in a laminar boundary layer. It is important to note that low-speed streaks generally lie beneath vortex furrows [62]. Vortex furrows are illustrated in Figure 6.1.

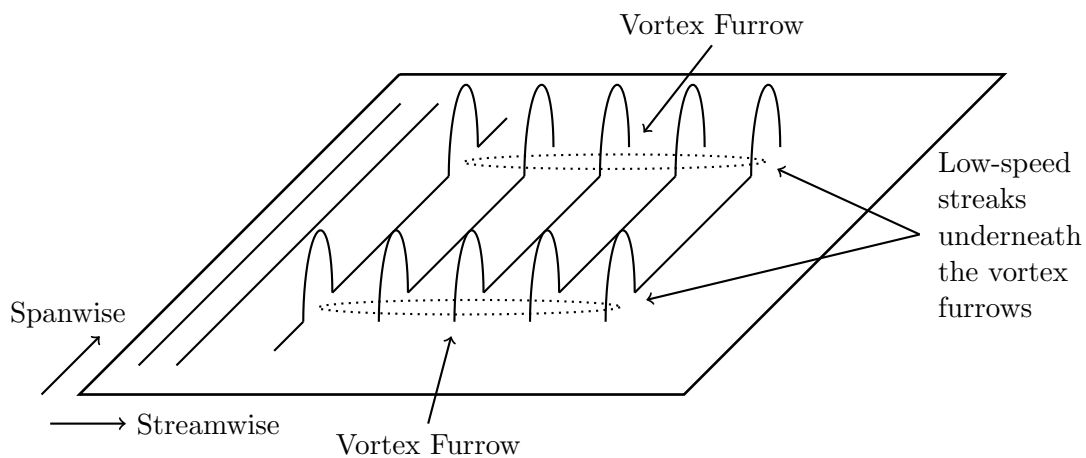


Figure 6.1: Vortex furrows in a transitioning boundary layer on top of low-speed streaks. The solid, thinner lines are vortex filaments.

At a given time, the upstream end of a furrow, which is closer to the laminar flow regime, has an ‘arch’ shape while the downstream end of a furrow, which is closer to the turbulent flow regime, has a ‘mushroom’ shape [63]. Figure 6.2 shows approximately what a furrow looks like at different streamwise locations.

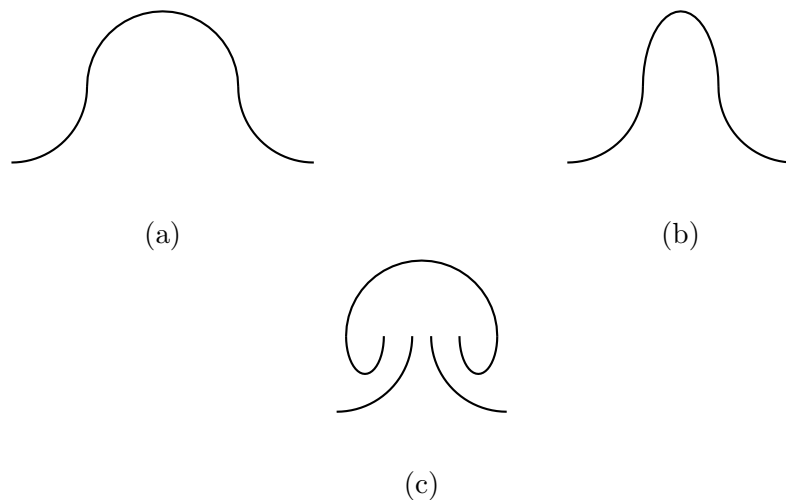


Figure 6.2: Vortex filaments in slices through a furrow in z - y planes at different streamwise locations at a fixed time (a) Towards the upstream end of a furrow (b) Between the upstream and downstream ends of a furrow (c) Towards the downstream end of a furrow

Figure 6.2 can also represent approximately how the vortex filaments change as one moves downstream along the length of the furrow at an appropriate convection velocity. In this case, the images in Figure 6.2a-c still represent a progression in the streamwise direction, but time increases moving from Figure 6.2a to Figure 6.2c [63]. When the vortex filaments within a furrow reach the state in which they form mushrooms, the lobes of the mushrooms possess streamwise-oriented vortex filaments, with one lobe inducing motion with a sense of rotation opposite to motion induced by the other lobe [62]. Mushroom lobes are labeled in Figure 6.3.

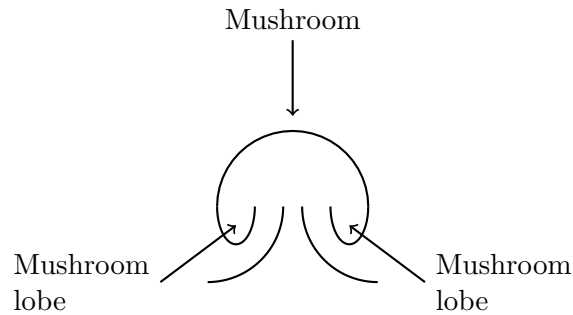


Figure 6.3: Identification of mushroom lobes

An important process within furrows occurs when pairs of streamwise-oriented vortex filaments¹ within the furrows induce oppositely-rotating motion which serves to both pull the ‘sides’ of the furrow together to form the stem of the mushroom and eject low-speed fluid outward from the boundary [62]. This is illustrated in Figure 6.4.

¹For a possible explanation as to how streamwise-oriented vortex filaments are generated in a furrow, see Section V.B. of [63].

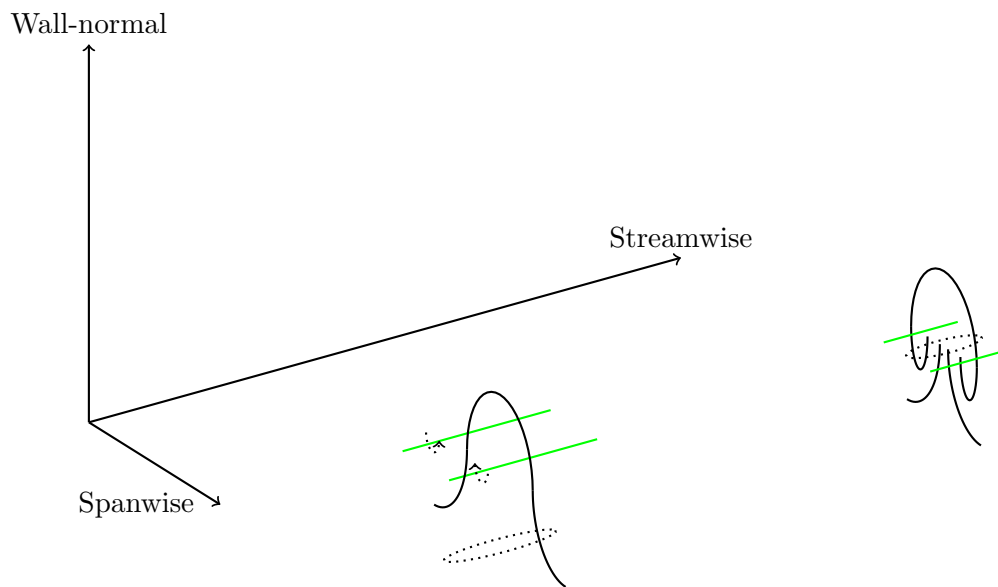


Figure 6.4: A pair of streamwise-oriented vortex filaments (in green) in a furrow inducing oppositely-rotating motion (described using dotted arrows) which forms the stem of a mushroom and lifts a low-speed streak (demarcated by a dotted line) away from the solid boundary.

It is important to be mindful of the role that non-rotational vorticity plays in fluid motions and processes. For instance, Bernard [64] stated that the first occurrences of near-wall rotational motion oriented about the streamwise direction in a transitioning boundary layer exists due to perturbations of the non-rotational spanwise vorticity that forms due to gradients in the wall-normal direction of the streamwise velocity.

It is noteworthy that Buffat et. al. [65], in their direct numerical simulation of flow in the entrance region of a channel undergoing bypass transitions², displayed plots of differences in the velocity field which were reminiscent of the mushrooms present in furrows [66].

²Transition to turbulence can be considered to be an orderly transition or bypass transition. Orderly transition contains within it the development of Tollmien-Schlichting (T-S) waves, whereas bypass transition does not. Bypass transition often occurs as the result of the presence of entities in the free-stream [67]. Tollmien-Schlichting waves are 2D waves that develop prior to the beginning of transition if the flow does not possess such things as turbulence in the free-stream [68].

Chapter 7

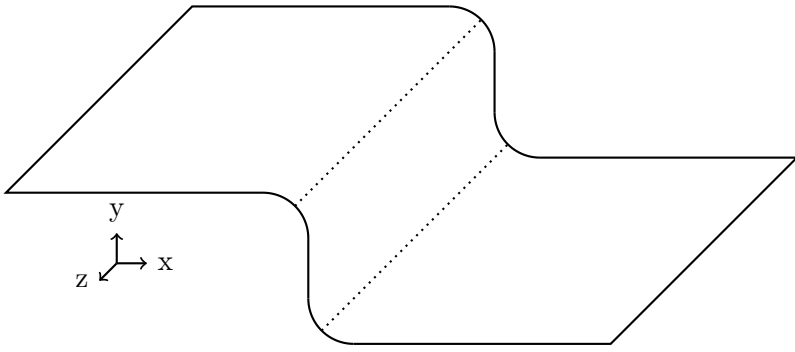
Step Flow Simulation

This chapter of the thesis describes both how the GVFS was used to simulate the step flow as well as some of the bulk properties of the resulting simulation.

7.1 Layout of the Step Geometry

To begin, this section describes the layout of the step geometry. Although only the top half of the step was analyzed for its vortical structure, the GVFS requires a symmetric geometry to run successfully. Therefore, many of the figures in this section display a symmetric geometry. But for the figures that display only the top half of the step it may be imagined that a symmetric configuration exists below it. It is also important to point out that the GVFS has trouble handling sharp edges so that many of the edges in the step geometry utilized for the present simulation have rounded edges.

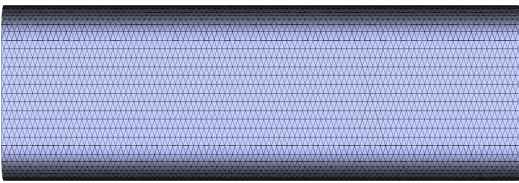
Figure 7.1a displays the coordinate directions used in the present simulation along with the relevant portions of the step geometry. Although the leading and rear edges of the step geometry are rounded, Figure 7.1a displays these edges as straight for the illustrative purpose of clarifying the orientation and location of the coordinate system. And although it may be difficult to discern from Figure 7.1a, the origin of the coordinate system lies at the leading edge of the step, in the center of the span, and slightly below the lower, horizontal plate. Figures 7.1b-e display the entire step geometry as observed from a couple of different viewpoints.



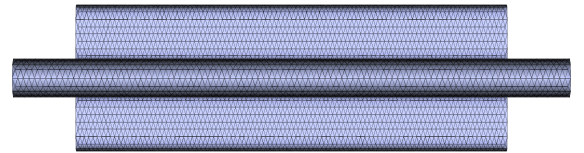
(a)



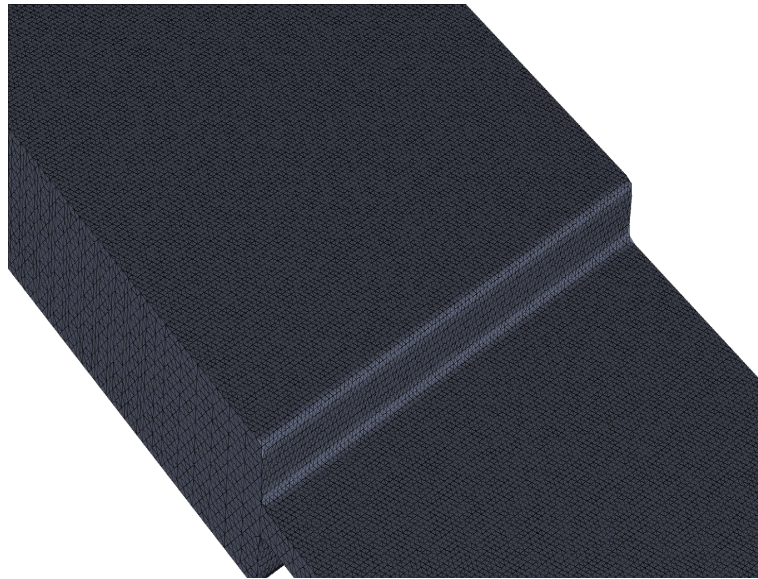
(b)



(c)



(d)



(e)

Figure 7.1: Illustration of the step geometry (figures (b)-(e) display the surface grid the step flow simulation utilizes): (a) Drawing of the coordinate system used in the step flow simulation along with an approximate outline of the upper portion of the step (b) Side view of the step (c) Front view of the step looking downstream (d) Back view of the step looking upstream (e) View of the step at an angle which shows the vertical step wall

Figure 7.2 displays another illustration of the top half of the step in order to provide some of its important dimensions and positioning (in this figure, the coordinate system is placed at the same location as in Figure 7.1a). In actuality, the leading and rear edges of the step are curved. But because the relevant part of the step used for the analysis of the vortical structure of the flow does not cover these areas, an approximation may be used which draws the leading and rear edges as straight.

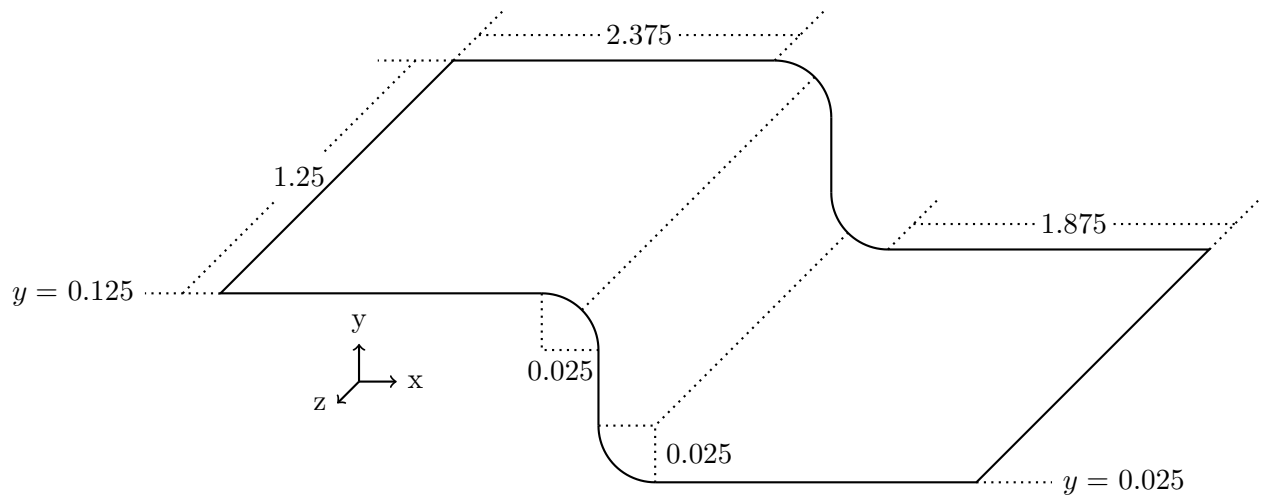


Figure 7.2: Illustration of the top half of the step along with its important dimensions and positioning

To summarize some of the important dimensions and positioning in Figure 7.2, the upper plate begins to curve around the upper step corner at $x = 2.375$ while the radius of this curve is 0.025 so that the vertical step wall is located at $x = 2.4$. The upper plate is at a height of $y = 0.125$. The vertical step wall begins to curve around the lower step corner at $y = 0.05$ and the radius of this curve is also 0.025 so that the lower plate is at a height of $y = 0.025$. And the streamwise distance from the vertical step wall to the end of the lower plate is $0.025 + 1.875 = 1.9$. The spanwise width of the step geometry is 1.25.

It was mentioned in Chapter 5 that the GVFS is made up of various patches where each patch can be either viscous or inviscid. For the current step geometry, the surface area represented by $-0.575 \leq z \leq 0.575$, $1 \leq x \leq 4.1$ is viscous while the remaining area of the step is inviscid. Data from the center of the span, $-0.25 \leq z \leq 0.25$, was used for the analysis of the step flow simulation.

7.2 Implementation of the Vortex Insertion Scheme

This section details the changes that were made to the GVFS to have it better simulate flow over a step. To start, it was noted in Chapter 5, that for flow over a flat plate, the GVFS solves the vorticity equation in a mesh made up of triangular prisms which is constructed by extending perpendiculars normal to the plate from the vertices of a triangular surface grid. A similar mesh is used for the step geometry. One of the differences between the step surface grid and the plate surface grid is that the step surface grid has to be rounded in the vicinity of the upper and lower step corners. This rounded part of the surface grid is displayed in Figure 7.3 which shows a portion of the step surface grid near the center of the span at and around the vertical step wall.

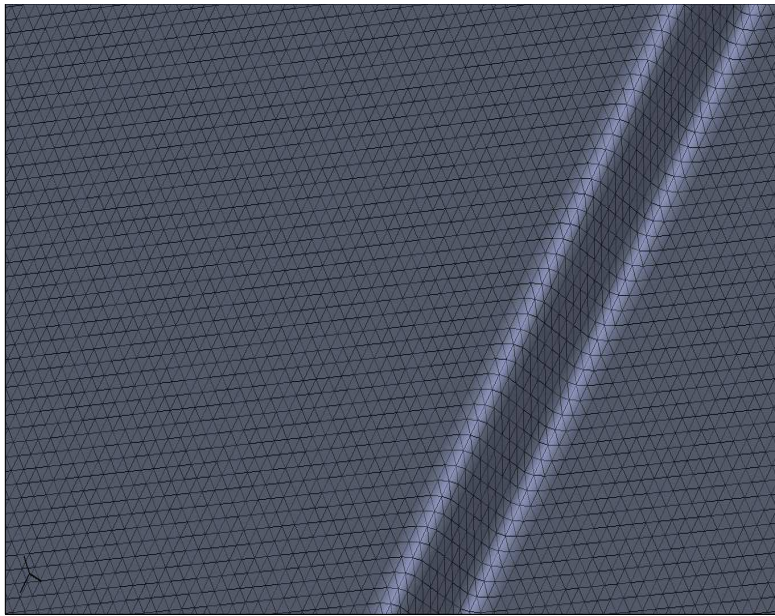


Figure 7.3: Display of the step surface grid at and around the curved step edges

As with the mesh for the flat plate geometry, the GVFS uses a mesh for the step geometry which is built up from lines perpendicular to the vertices of the surface grid. The mesh for the step geometry has ten levels going out in a direction normal to the surface. The first level of the mesh is half the thickness of the other levels. With Δy as the thickness of the upper levels of the mesh, the first level of the mesh has thickness $\Delta y/2 \approx 6.3 \times 10^{-4}$ while the other nine levels of the mesh have thickness $\Delta y \approx 12.6 \times 10^{-4}$. In total, the mesh extends out in a direction normal to the surface of 0.012. Figure 7.4 illustrates this configuration in a 2D plane.

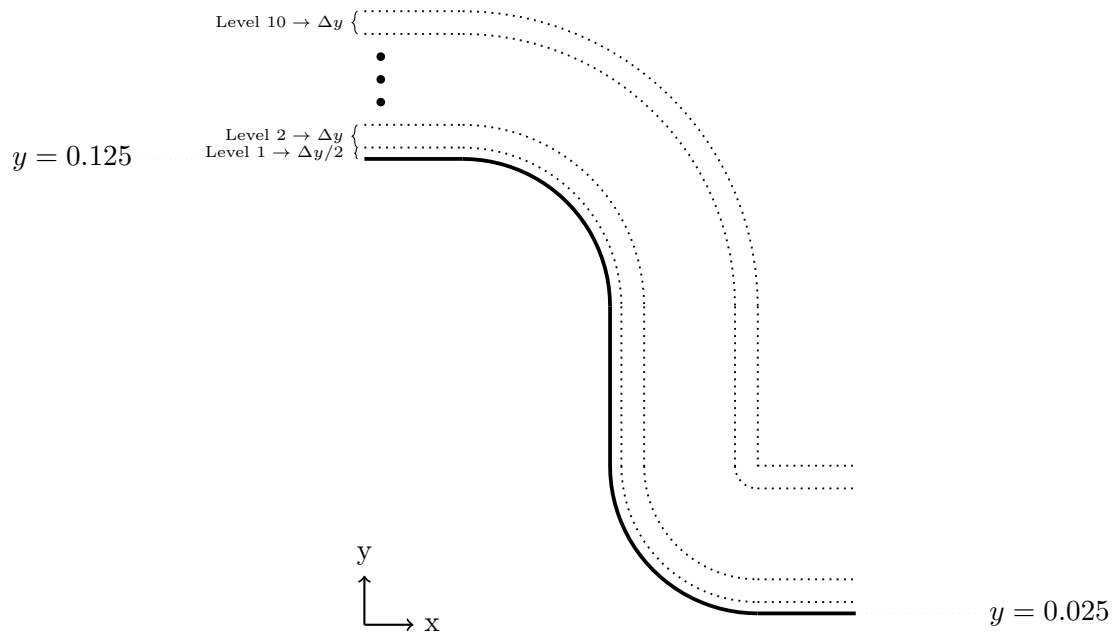


Figure 7.4: 2D illustration of the step mesh

The original version of the GVFS produced unphysical behavior past the step edge with streamlines which did not display any separation and curved sharply downward immediately downstream of the step edge. This behavior is illustrated in Figure 7.5.

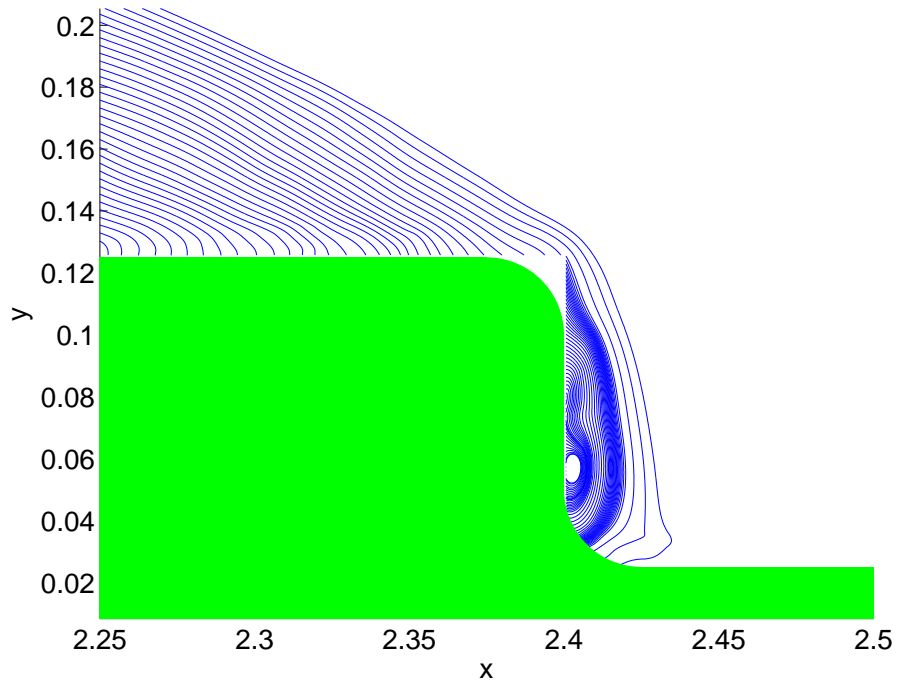
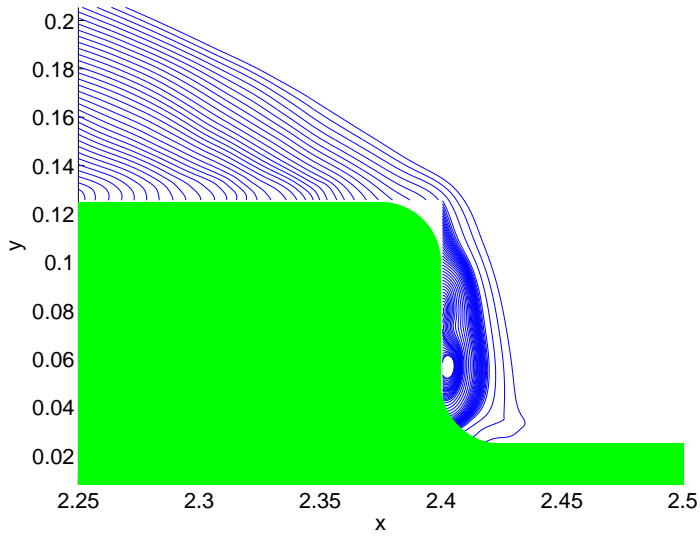


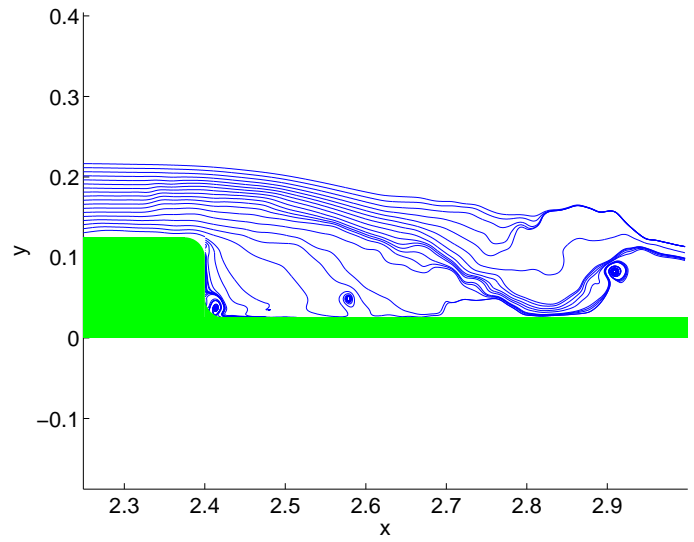
Figure 7.5: Instantaneous, 2D streamlines in the plane $z = 0$ generated by the original version of the GVFS

It was conjectured that the unphysical behavior depicted in Figure 7.5 was perhaps a result of vorticity in the mesh at, and immediately downstream of, the step edge preventing a separating streamline pattern in that vorticity might somehow be ‘trapped’ in the mesh in this region of the flow. As an attempt to remedy this problem, the following idea (which will be referred to in the rest of this thesis as the *vortex insertion scheme*) was attempted: at every time step at which vortex tubes were released from the top layer of the mesh, a vortex tube was created to replace the vorticity at every prism in the mesh that lay between $2.4 \leq x \leq 3.1$ with the tubes having a circulation based upon the local vorticity, i.e. Eq. 5.16 was used to determine the circulation with Ω as the local vorticity within a prism. It was reasoned that because the GVFS counts the contribution to the velocity from the prisms as if they were tubes away from their immediate vicinity [62] through the use of Eq. 5.16, it is reasonable to create tubes within a portion of the mesh based on local vorticity with the hope that this would stop inhibiting a separating streamline pattern. As a visual aid, Figure 7.6 displays a picture of the upper half of the step geometry along with an outline of the relevant part of the mesh where tubes are created in the vortex insertion scheme based on local vorticity. Because the step geometry is symmetric, the vortex insertion scheme applies to the lower half as well. But because only data from the top half of the step geometry was used for the structural analysis, only the top half of the step geometry is drawn in Figure 7.6.

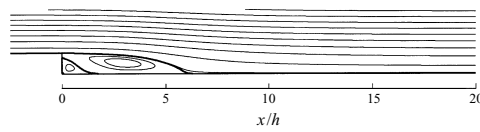
The results of simulating the step flow with the vortex insertion scheme are displayed in Figure 7.7b alongside a re-printing of Figure 7.5 in Figure 7.7a and a plot of mean streamlines from a DNS of the step flow with straight edges [13] in Figure 7.7c. A comparison of Figure 7.7b, which displays 2D, instantaneous streamlines from the simulation with the vortex insertion scheme to Figure 7.7a, which displays 2D, instantaneous streamlines from the simulation without the vortex insertion scheme, demonstrates that the vortex insertion scheme significantly affects the flow pattern at and around the step edge. In Figure 7.7a, the streamlines prior to the step edge possess a pronounced downward slant and immediately downstream of the step edge the streamlines drop precipitously downward toward the lower plate. Figure 7.7b, on the other hand, possesses a number of streamlines which are directed roughly straight around the step edge and curl slowly downward until some of these streamlines reach the lower plate well downstream of the step edge. In addition, many of the streamlines in Figure 7.7b which are situated near the upper step corner spread out as they emerge into the separated region. Although the curvature of the upper step corner directs fluid adjacent to it more vertically downward than flow over a step with straight edges, a comparison of the streamlines in Figure 7.7b to the streamlines of a DNS [13] of the step flow with straight edges (Figure 7.7c) demonstrates the overall similarity of the two flow patterns in the separated region around and above the height of the step in that both pictures contain streamlines which curve gently downward toward the lower plate.



(a)



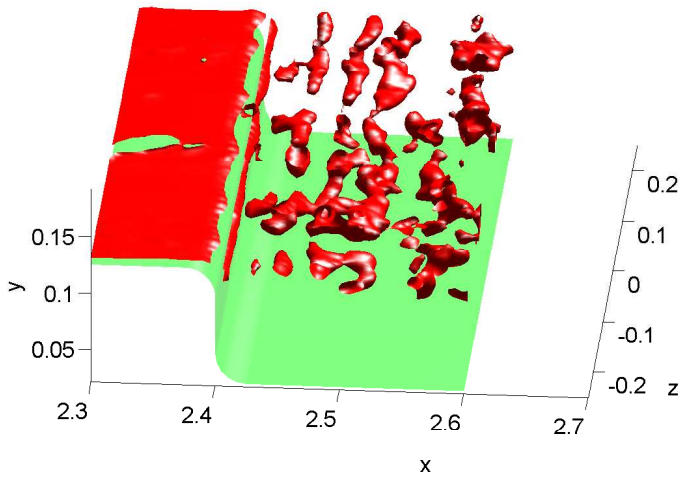
(b)



(c)

Figure 7.7: Instantaneous, 2D streamlines in the plane $z = 0$: (a) without the vortex insertion scheme (b) with the vortex insertion scheme (c) Mean streamlines in a DNS of flow over a backward-facing step with straight edges [13]

It is also important to point out that the simulation with the vortex insertion scheme generates a nice set of roller vortices downstream of the step edge, as is illustrated in Figure 7.8a (the mesh used in this figure to generate the isosurfaces was tailored so as to illuminate the presence of the roller vortices). The roller vortices from the GVFS's simulation of the step flow match nicely with an LES conducted by Silveira Neto et. al. [94] as displayed in Figure 7.8b. Both plots in Figure 7.8 display rollers vortices which extend across the span. That the roller vortices in Figure 7.8a possess spanwise gaps (to be discussed further in Chapter 8) but the rollers vortices in Figure 7.8b continue uninterrupted across the span is probably due to the fact that the simulation pictured in Figure 7.8b is generated using conditions in the upstream boundary layer which do not take into account the spanwise make-up of boundary layers (furrows, low-speed streaks, etc.). Despite this difference, both pictures in Figure 7.8 display a nice set of roller vortices in the separated region downstream of the step edge.



(a)



(b)

Figure 7.8: (a) Instantaneous isosurfaces of $\Omega_z = -55$ generated by the GVFS's simulation of the step flow with the vortex insertion scheme (b) Figure 7a from Silveira Neto et. al. [94] with isosurfaces of the magnitude of vorticity in blue, isosurfaces of streamwise vorticity at a positive level in yellow, and isosurfaces of streamwise vorticity at a negative level in green

Returning to Figure 7.7b, it can be observed that reattachment occurs at roughly $x = 2.8$, where the streamlines which emanate from the upstream boundary layer pass into the separated region and curve down to the lower plate. More visually descriptive depictions of reattachment are provided by Figure 7.9. Figure 7.9a re-prints the same streamlines in Figure 7.7b along with the approximate reattaching streamline in red, while Figure 7.9b displays an instantaneous contour plot of streamwise velocity in a plane close to the lower plate at the same instant in time as Figure 7.9a. Observation of Figure 7.9b shows that reattachment occurs at around $x = 2.8$ where the downstream-moving fluid abuts the backflow. It should be pointed out that the streamlines in Figure 7.9a which are immediately adjacent to the upper plate curl around the curved upper step corner when they proceed out over the step edge and slant downward toward the lower plate. These streamlines do not participate in the reattachment as defined by the trajectory of the red streamline in Figure 7.9a. This part of the step flow pattern in the present simulation stands in contrast to the flow pattern around a backward-facing step with straight edges in which all of the streamlines which progress past the upper step corner into the separated region eventually reach reattachment. This aspect of the flow pattern in flow over a backward-facing step with straight edges is visible in Figure 7.7c wherein even the mean streamlines adjacent to the upper plate reach reattachment. It is also noteworthy that with reattachment in Figure 7.9a at about $x = 2.8$, this equates to a reattachment length of about four step heights which is less than that seen in flow over a backward-facing step with straight edges (Le, Moin, and Kim [13] reported a mean reattachment length of 6.28 step heights downstream of the step edge).

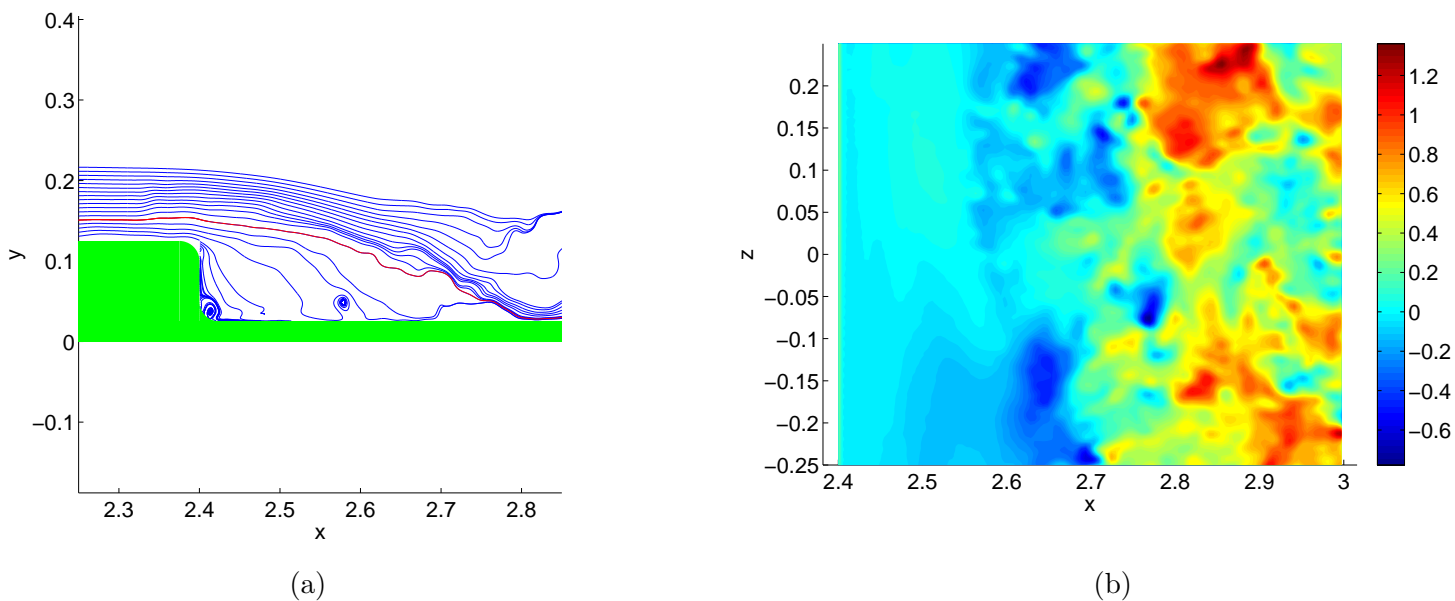


Figure 7.9: (a) Instantaneous, 2D streamlines in the plane $z = 0$ with the red streamline marking the approximate reattaching streamline (b) Instantaneous contour plot of streamwise velocity in the plane $y = 0.03$ (lower plate lies at $y = 0.025$) at the same time as the plot in (a)

The reduction in reattachment length in the present simulation as compared to flow over a step with straight edges can be attributed to two factors. The first factor which leads to a reduction in reattachment length in the present simulation is the fact that the GVFS simulates flow over a backward-facing step using curved edges. In order to attain an understanding of how a curved step edge can affect the flow around it, it is helpful to consider the work of Choi et. al. [133] and Thacker et. al. [134]. Choi et. al., in an *Annual Review of Fluid Mechanics* journal article, examined the flow patterns around heavy vehicles, such as trucks. One simplified model they considered is the *Ahmed* model pictured below in Figure 7.10a (Figure 1a in Choi et. al.). When α (defined in Figure 7.10a) becomes large enough, the flow separates where the top plates meets the slanted plate. This is illustrated in Figure 7.10b (part of Figure 2b in Choi et. al.).

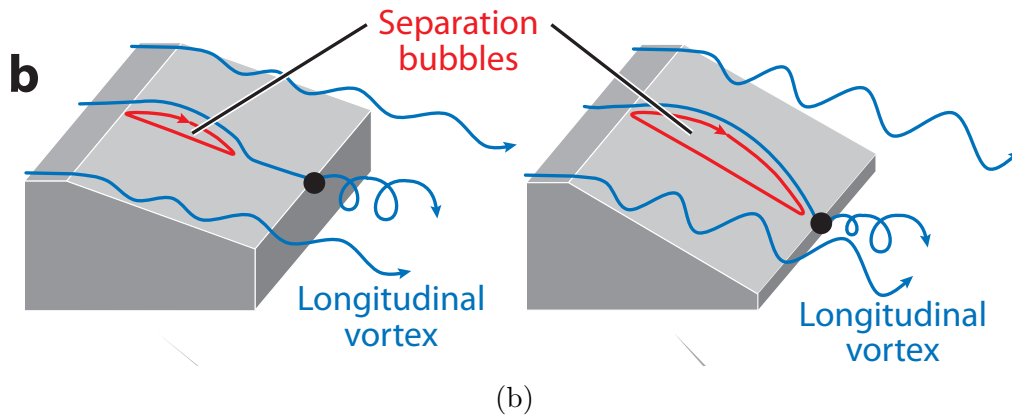


Figure 7.10: (a) Illustration of the *Ahmed* model, Figure 1a of Choi et. al. [133] (b) Separated flow over the *Ahmed* model, part of Figure 2b of Choi et. al. [133]

One of the journal articles Choi et. al. cite when discussing the Ahmed model is the work authored by Thacker et. al. [134]. Thacker et. al., in an experimental investigation, considered flow over two Ahmed models, one with a straight edge between the top plate and slanted plate and another with a curved edge between the top plate and slanted plate. These two set-ups are illustrated in Figure 7.11 (Figure 2 of Thacker et. al. [134]). Thacker et. al.'s results revealed that, while the flow separated where the top plate met the slanted plate for the case of the straight-edge set-up, the flow didn't separate where the top plate met the slanted plate for the case of the curved-edge set-up. These results are illustrated in Figure 7.12 (Figure 7 of Thacker et. al.).

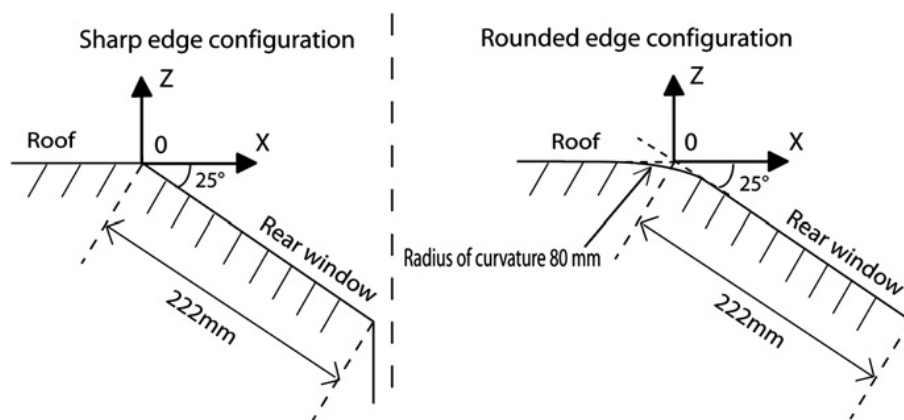


Figure 7.11: Ahmed models with straight or curved edges between the top plate and slanted plate, Figure 2 of Thacker et. al. [134]

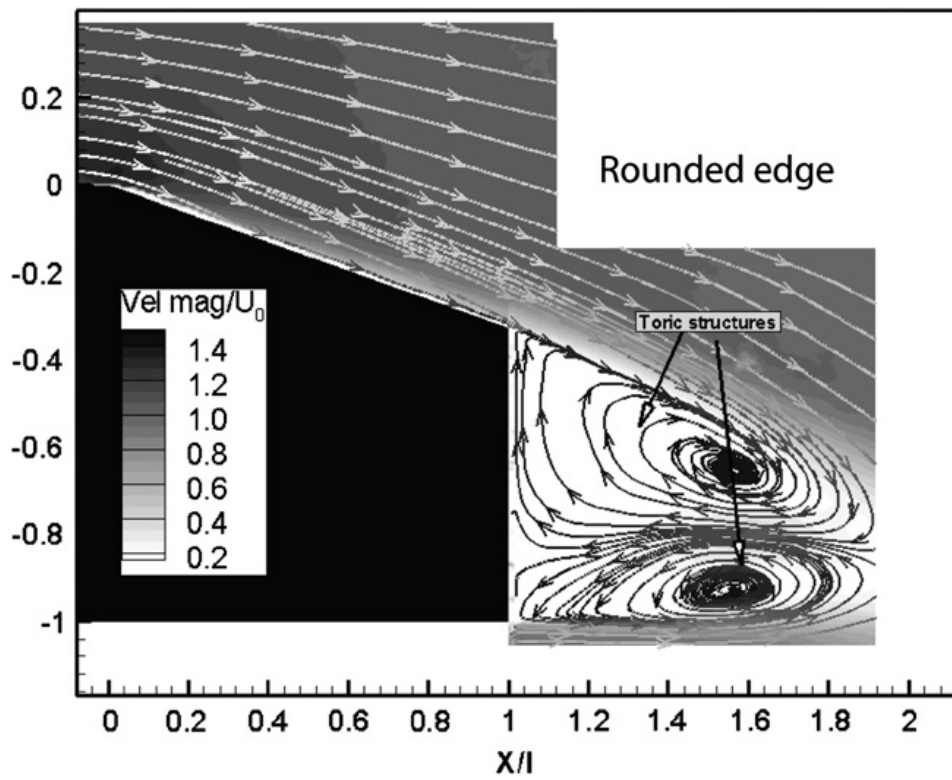
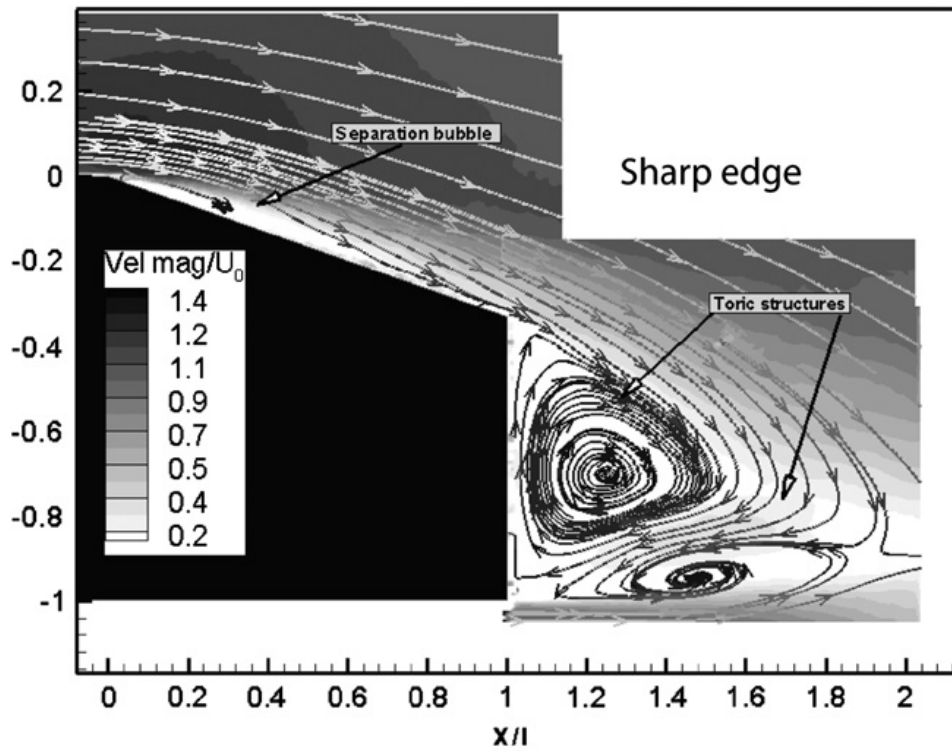
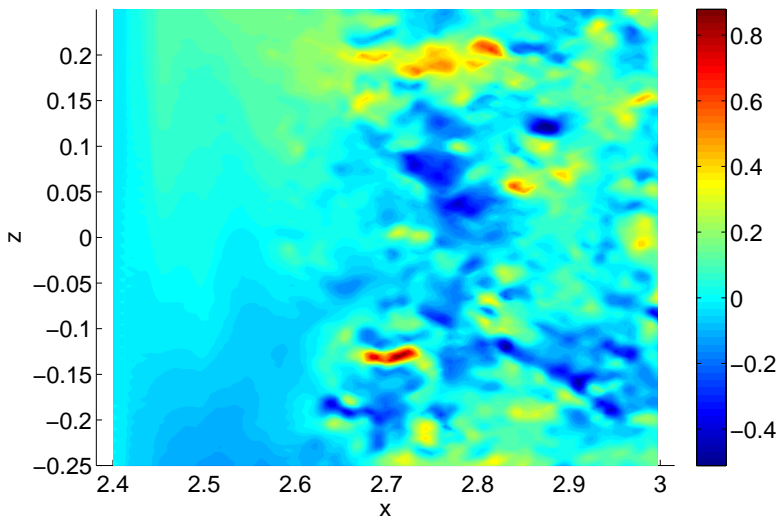


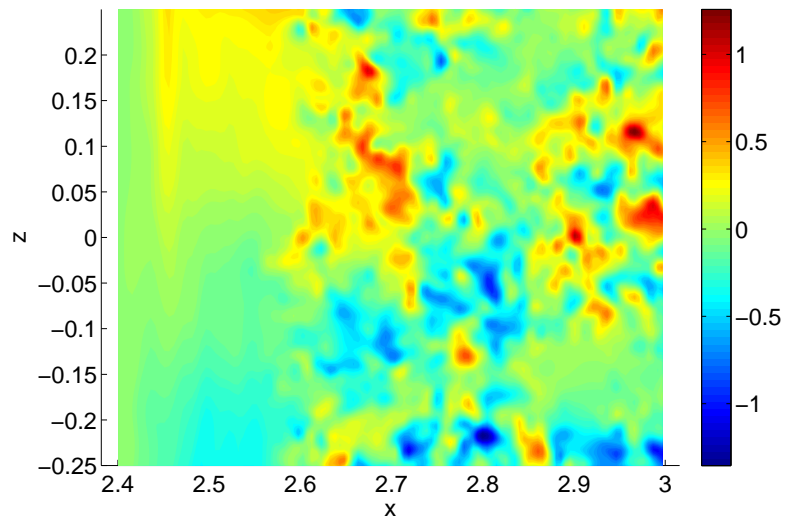
Figure 7.12: Flow past the two configurations illustrated in Figure 7.11 (Figure 7 of Thacker et. al. [134])

The ideas involving separation contained in Figures 7.10, 7.11, and 7.12 are relevant to the step geometry utilized by the GVFS. In particular, Figure 7.12 illustrates that a rounded edge can curtail the effects of separation. This same phenomenon appears to be occurring in the GVFS's step flow simulation in that the upper rounded step corner curtails the full effects of separation, thereby leading to shorter reattachment lengths.

The second factor which reduces the reattachment length in the present simulation revolves around the idea that the GVFS's simulation of the step flow utilizes a step geometry with a finite spanwise width without periodic boundary conditions. Evidence to support the idea that the finite spanwise width of the step flow geometry is affecting the simulation is provided by Figure 7.13 which displays contour plots of spanwise velocity in two different $x - z$ planes downstream of the step. Both plots in this figure reveal that upstream of roughly $x = 2.6$ the fluid moves toward either end of the plate, an indication that the limited spanwise extent of the step is affecting the flow even within the central portion of the flow domain illustrated in Figure 7.13 ($-0.25 \leq z \leq 0.25$).



(a)



(b)

Figure 7.13: Contour plots of W in the planes: (a) $y = 0.026$ (b) $y = 0.076$

7.3 Analysis of the Vortex Insertion Scheme

With the previous section of this thesis detailing the implementation of the vortex insertion scheme, this current section analyzes the vortex insertion scheme in order to explain why it works in the way that it does.

As a starting point for this discussion, Figure 7.14 re-prints instances of the streamline patterns generated without and with the vortex insertion scheme.

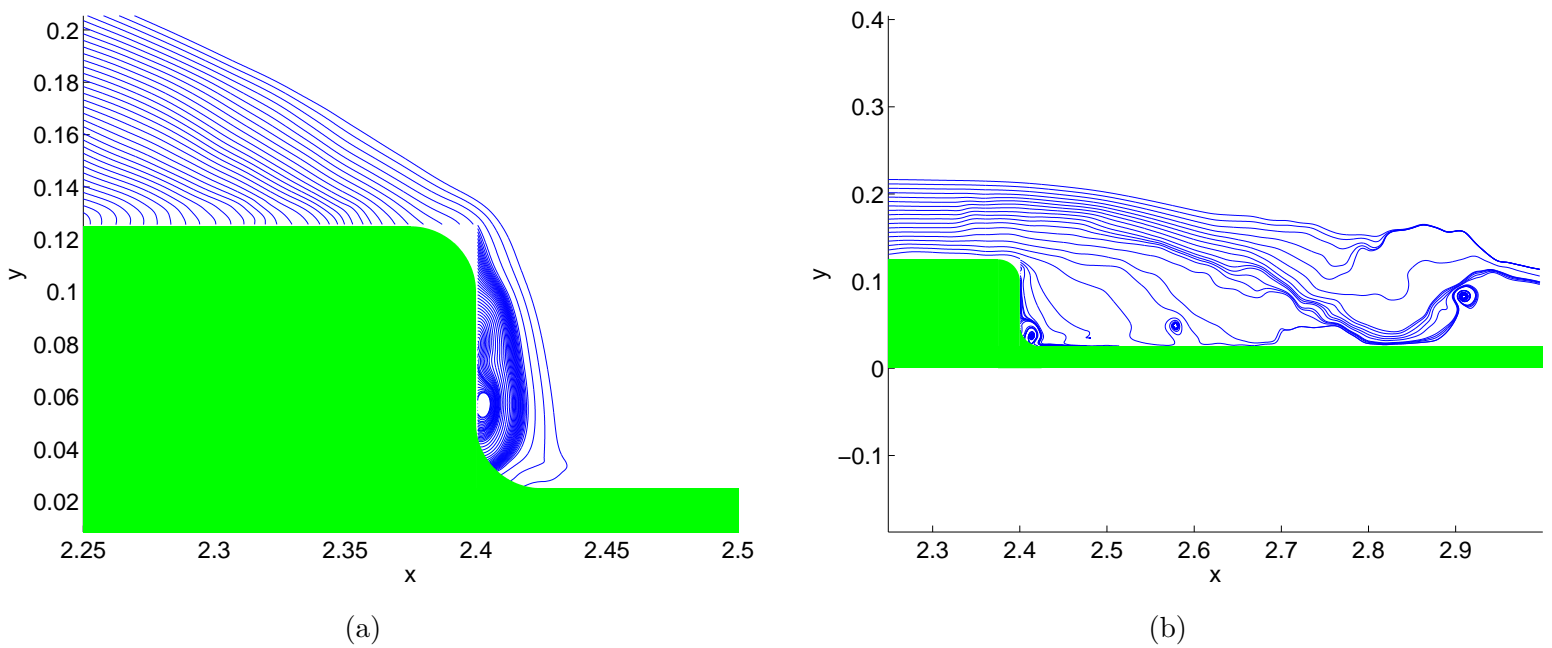


Figure 7.14: Instantaneous, 2D streamlines in the plane $z = 0$: (a) without the vortex insertion scheme (same plot as Figure 7.7a) (b) with the vortex insertion scheme (same plot as Figure 7.7b)

The stark change in streamline pattern between Figures 7.14a and 7.14b is generated by a change in sign of the spanwise vorticity downstream of the vertical step wall. Figure 7.15 displays a line plot of spanwise vorticity at two different streamwise locations downstream of the vertical step wall both with and without the vortex insertion scheme. This figure demonstrates that the vortex insertion scheme largely changes the sign of the spanwise vorticity in the region just downstream of the vertical step wall (located at $x = 2.4$) and beneath the height of the step edge (located at $y = 0.125$).

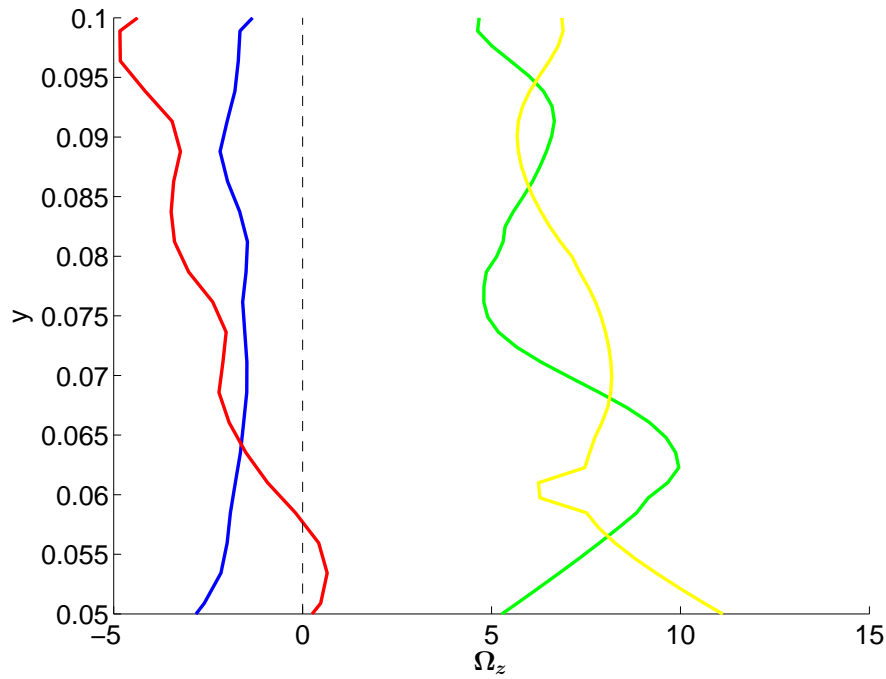


Figure 7.15: Line plots of spanwise vorticity: —, $x = 2.425$, with vortex insertion scheme; —, $x = 2.425$, without vortex insertion scheme; —, $x = 2.45$, with vortex insertion scheme; —, $x = 2.45$, without vortex insertion scheme

The influence of negative spanwise vorticity beneath the separated region on the separated region can be seen in the shape of the streamlines as is shown in Figure 7.16. In this figure, the same streamlines as Figure 7.7b are plotted (with the vortex insertion scheme) along with the trajectory induced by negative spanwise vorticity represented by the pathline (projected onto the $z = 0$ plane) of a particle which begins around separation and moves toward the lower plate (green line with the trajectory of the particle moving from left to right). The streamlines in the separated region clearly conform to the shape and orientation of the green line which indicates that the negative spanwise vorticity beneath the separated region does induce changes in the shape of the streamlines above it.

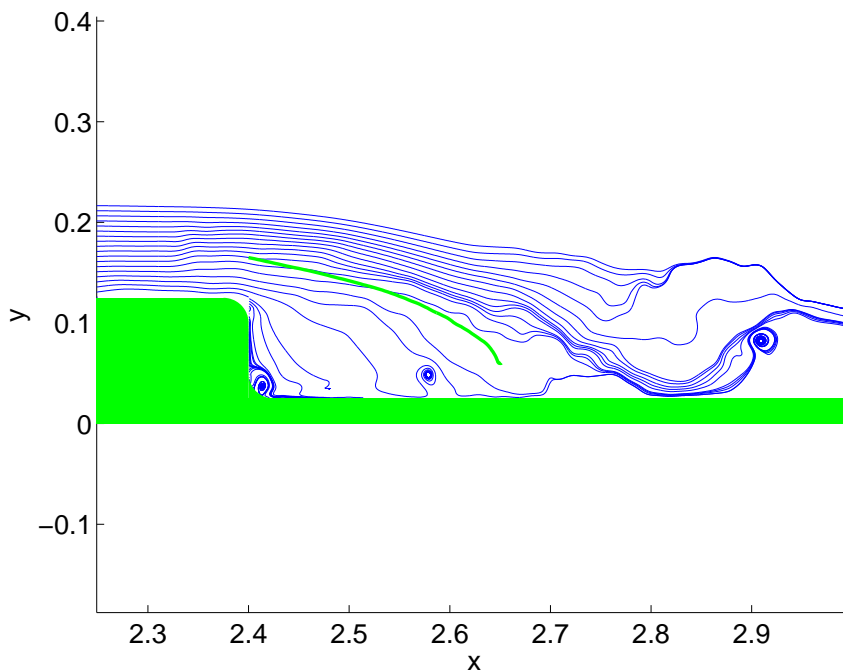
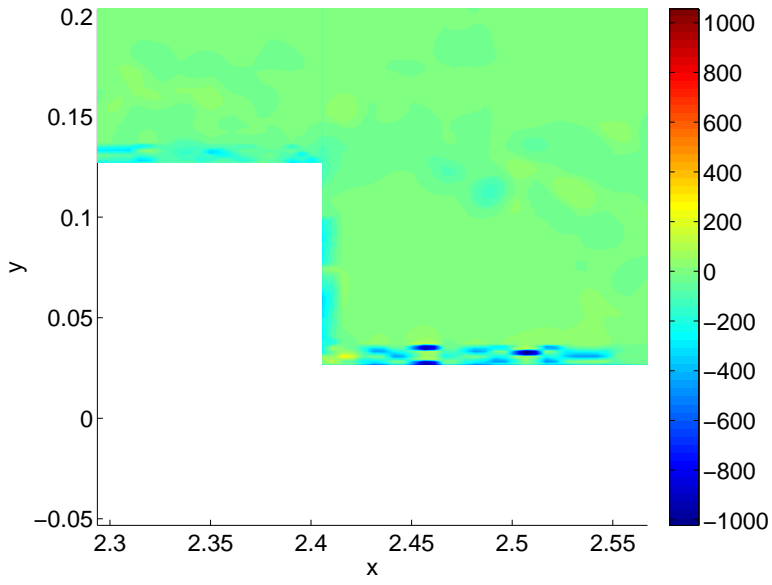
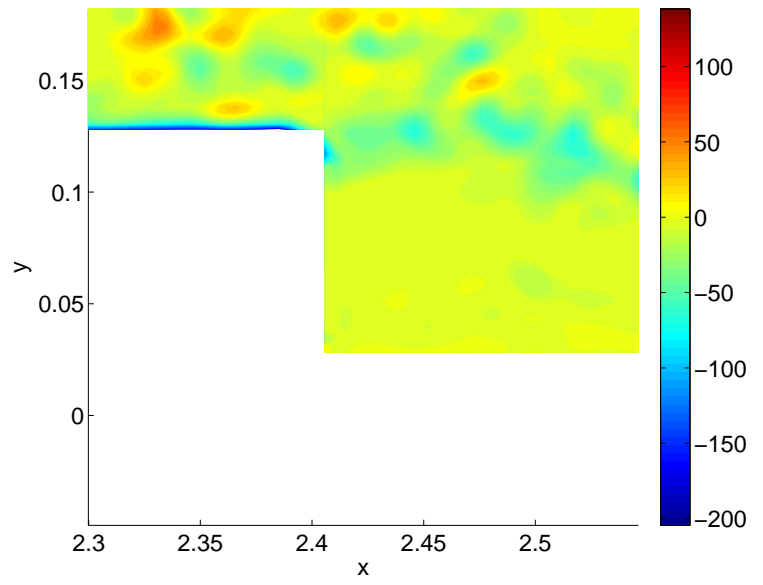


Figure 7.16: Instantaneous, 2D streamlines from the plane $z = 0$ from the simulation with the vortex insertion scheme with the green line representing the pathline (flow from left to right) of a particle projected onto the $z = 0$ plane

The effect of the vortex insertion scheme in creating negative spanwise vorticity beneath the separated region can be seen in Figure 7.17, which displays contour plots of spanwise vorticity in the simulations with and without the vortex insertion scheme. In the plot of spanwise vorticity in the simulation without the vortex insertion scheme (Figure 7.17a), there is a narrow band of negative spanwise vorticity adjacent to the vertical step wall from around $y = 0.05$ to around $y = 0.1$. Just downstream of this region, the spanwise vorticity is positive. This rather sharp discontinuity in the spanwise vorticity indicates that the vorticity in the wall-adjacent mesh was not properly transported into the outer flow without the vortex insertion scheme. By contrast, the contour plot of spanwise vorticity from the simulation with the vortex insertion scheme (Figure 7.17b) displays a distribution of spanwise vorticity which is largely negative near the vertical step wall without any sharp discontinuities immediately adjacent to the vertical step wall. By inserting tubes into the flow at all levels of the mesh which subsequently move along with the local fluid velocity, the area beneath the separated region is populated with a greater concentration of tubes which generate negative spanwise vorticity. This effect can be observed in Figure 7.18 in which the region beneath the separated zone is more heavily populated by tubes in the simulation with the vortex insertion scheme than in the simulation without the vortex insertion scheme. The spanwise vorticity in the region near the vertical step wall is negative because the tubes that are originally created adjacent to the vertical step wall possess negative spanwise vorticity. This is the case because the fluid which flows around the upper step corner gets sent downward and moves next to fluid which has zero velocity due to the no-slip condition leading to $\frac{\partial V}{\partial x} < 0$. Figure 7.19 displays a distribution of wall-normal velocity which moves slowly downward near the vertical step wall.

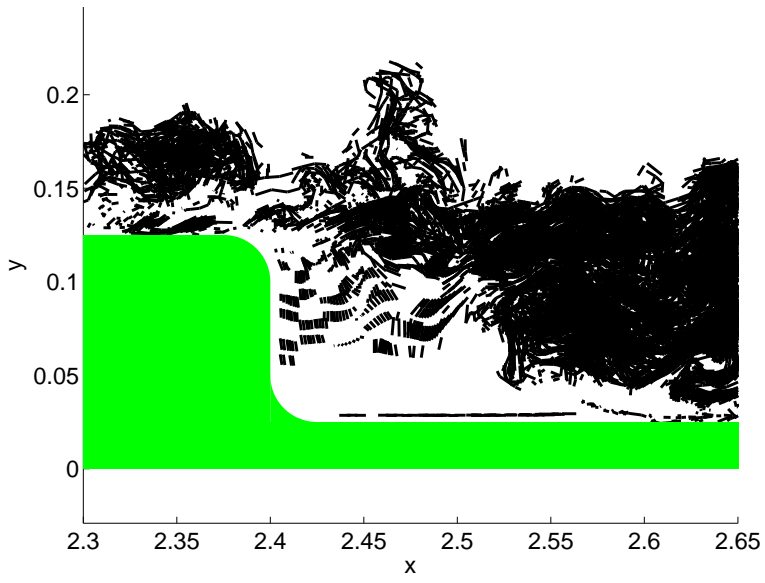


(a)

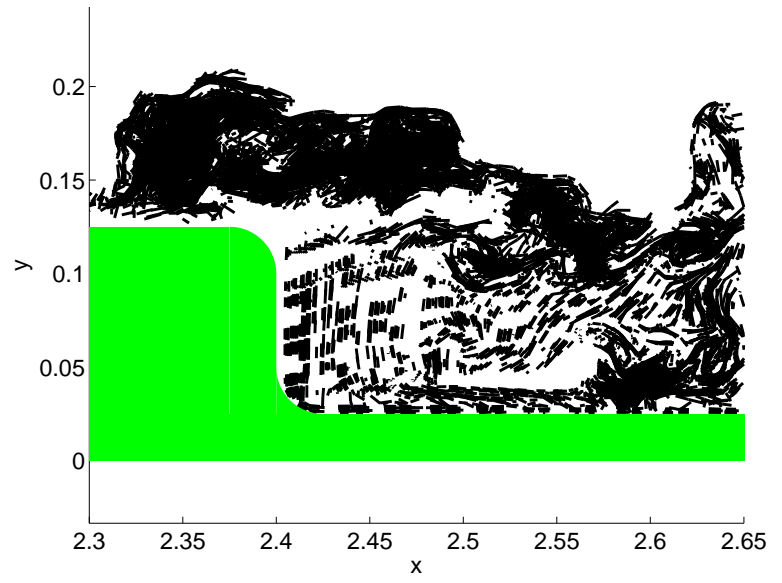


(b)

Figure 7.17: Contour plot of spanwise vorticity in the plane $z = 0$: (a) without the vortex insertion scheme (b) with the vortex insertion scheme



(a)



(b)

Figure 7.18: Plot of tubes in the plane $z = 0$: (a) without the vortex insertion scheme (b) with the vortex insertion scheme

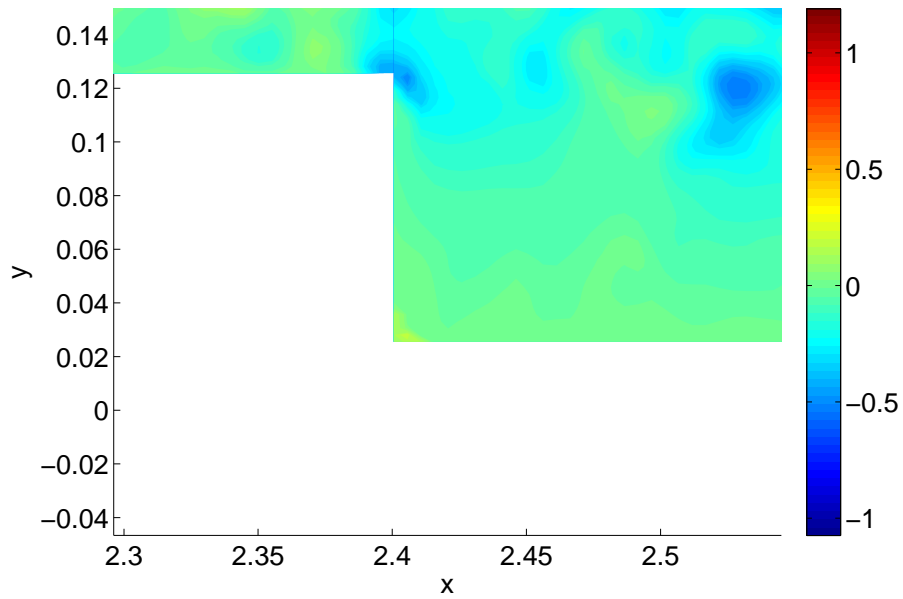
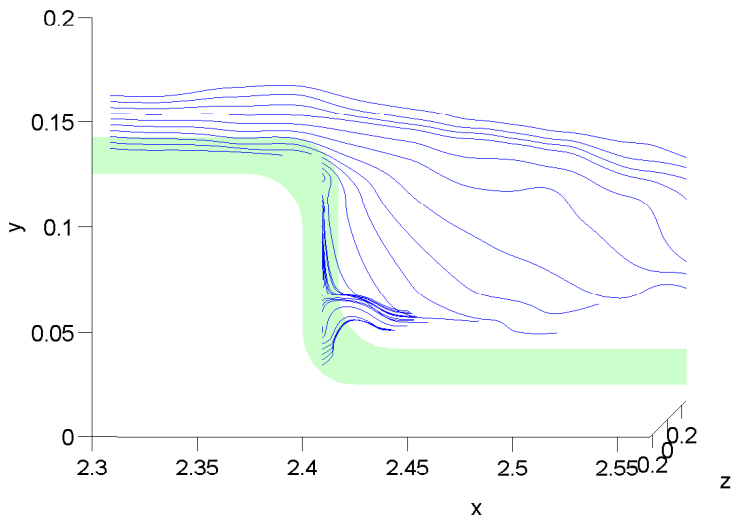


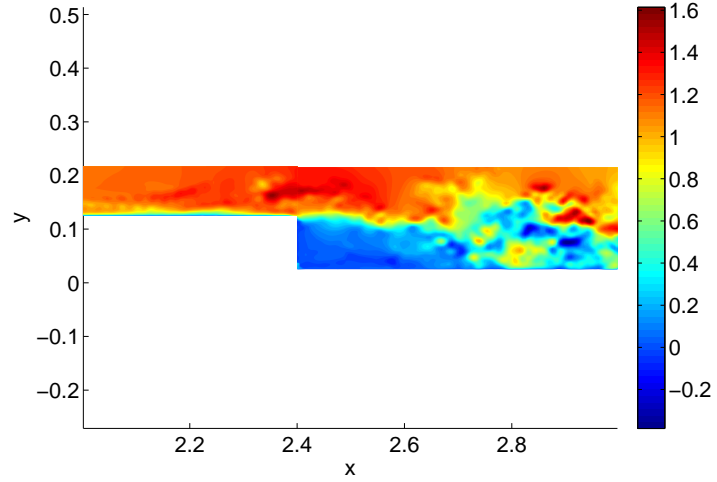
Figure 7.19: Contour plot of wall-normal velocity in the plane $z = 0$ from the simulation with the vortex insertion scheme

As indicated by the streamlines in Figure 7.20a, when the fluid passes over the step edge¹ it fills out a wider region, leading to a diverging of the streamlines, and, by conservation of mass, a slowing-down of the fluid in the region adjacent to the step edge and the formation of a shear layer. Figure 7.20b displays a contour plot of streamwise velocity in the plane $z = 0$ and Figure 7.20c is a line plot of streamwise velocity at $x = 2.43$. Both of these plots display a nice shear layer adjacent to the step edge. Figure 7.20d, which is a contour plot of streamwise velocity in the plane $x = 2.43$, demonstrates that this shear layer extends across the span.

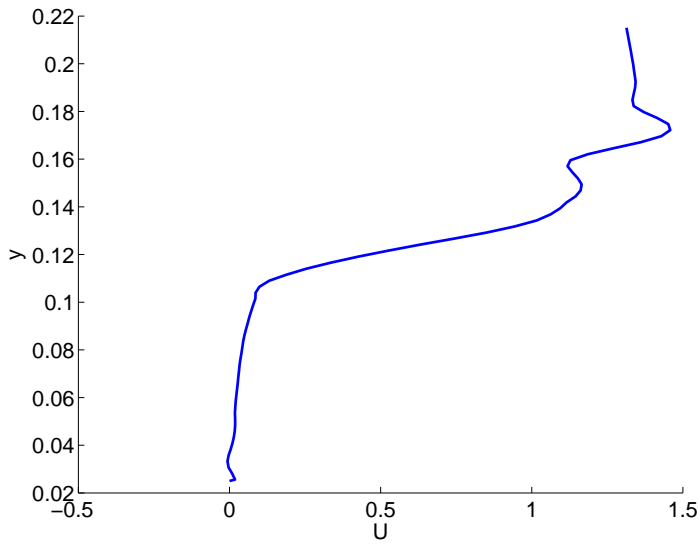
¹It is worth noting that although the plots in Figure 7.20 come from the simulation with the vortex insertion scheme, a shear layer exists in the simulation without the vortex insertion scheme. However, the streamline pattern in the separated and reattachment regions in the simulation without the vortex insertion scheme is very different from that of the simulation with the vortex insertion scheme as is evidenced by Figures 7.7a and 7.7b.



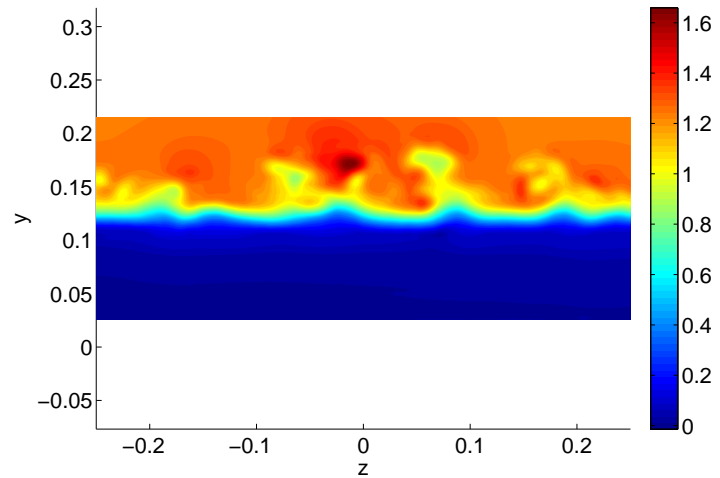
(a)



(b)



(c)



(d)

Figure 7.20: All plots in this figure taken from the simulation with the vortex insertion scheme: (a) Instantaneous, 3D streamlines emanating from points in the plane $z = 0$ (b) Contour plot of streamwise velocity in the plane $z = 0$ (c) Streamwise velocity line plot at $x = 2.43$ (d) Contour plot of streamwise velocity in the plane $x = 2.43$

7.4 Time Development of the Step Flow Simulation

With the vortex insertion scheme implemented, the GVFS was used to simulate flow over a backward-facing step. Figure 7.21a displays the time development of the simulation from the viewpoint of the number of tubes and filaments in the flow. Observation of Figure 7.21a reveals that a rough equilibrium is reached in the simulation at around $t = 5.4$. At around this time production of new tubes in the simulation from the near-wall mesh and vortex stretching occurs at around the same level as removal of tubes which either cross over boundaries or enter into the loop removal algorithm [62]. As another way to check that equilibrium has been reached, Figure 7.21b displays a view from overhead of the tubes in the upstream boundary layer which lie between $x = 1.2$ and $x = 2.4$ (the step edge is located at $x = 2.4$) at time $t = 5.44$. Observation of Figure 7.21b demonstrates that a full set of furrows has formed across the span and that these furrows have begun to break up at the right side of the picture so that the fluid is in the late transitional regime at separation.

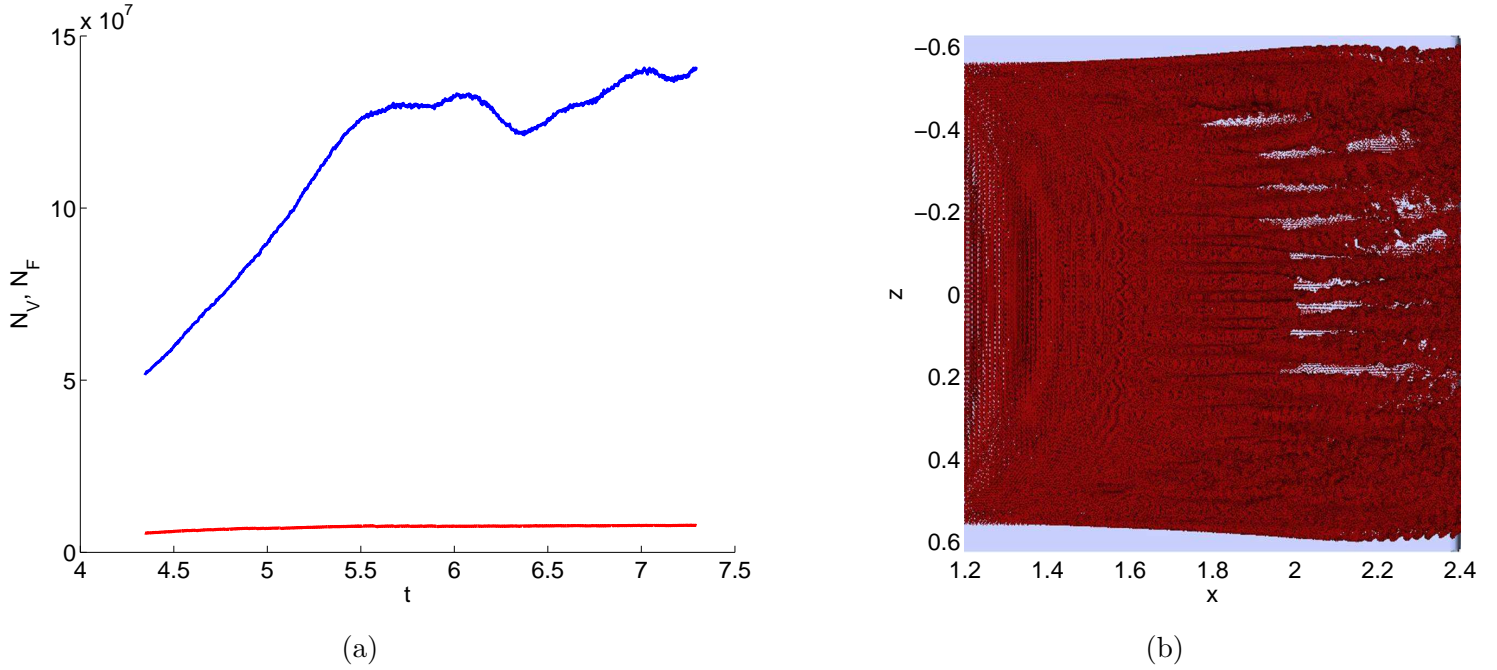


Figure 7.21: (a) Time development of the step flow simulation: --- , number of tubes (N_V); --- , number of filaments (N_F) (b) View from overhead of the tubes in the upstream boundary layer which lie between $x = 1.2$ and $x = 2.4$ (the step edge is located at $x = 2.4$) at time $t = 5.44$

7.4.1 State of the Fluid at Reattachment

With the state of the fluid at separation in the late transitional regime, one can determine the state of the fluid at reattachment by comparing skin friction coefficients at separation and reattachment. Indeed, the skin friction coefficient has been used to determine the difference between the laminar, transitional, and fully turbulent regimes in flow in a channel [65] and flow over a flat plate [69]. With the skin friction coefficient defined as

$$C_f = \frac{\nu \frac{\partial U}{\partial y} \Big|_{y=0}}{\frac{1}{2} U_\infty^2} \quad (7.1)$$

Figure 7.22 displays contour plots of the instantaneous skin friction coefficients on the upper and lower plates in the present step flow simulation. Figure 7.22a, which represents transitional boundary layer flow, possesses at least some degree of regularity, including the imprint of low-speed streaks

spaced out across the span. Conversely, Figure 7.22b, in which reattachment occurs at about $x = 2.8$ where the downstream-moving fluid meets the back-flow, possesses no regularity at or downstream of $x = 2.8$. This demonstrates that the flow is fully turbulent at reattachment.

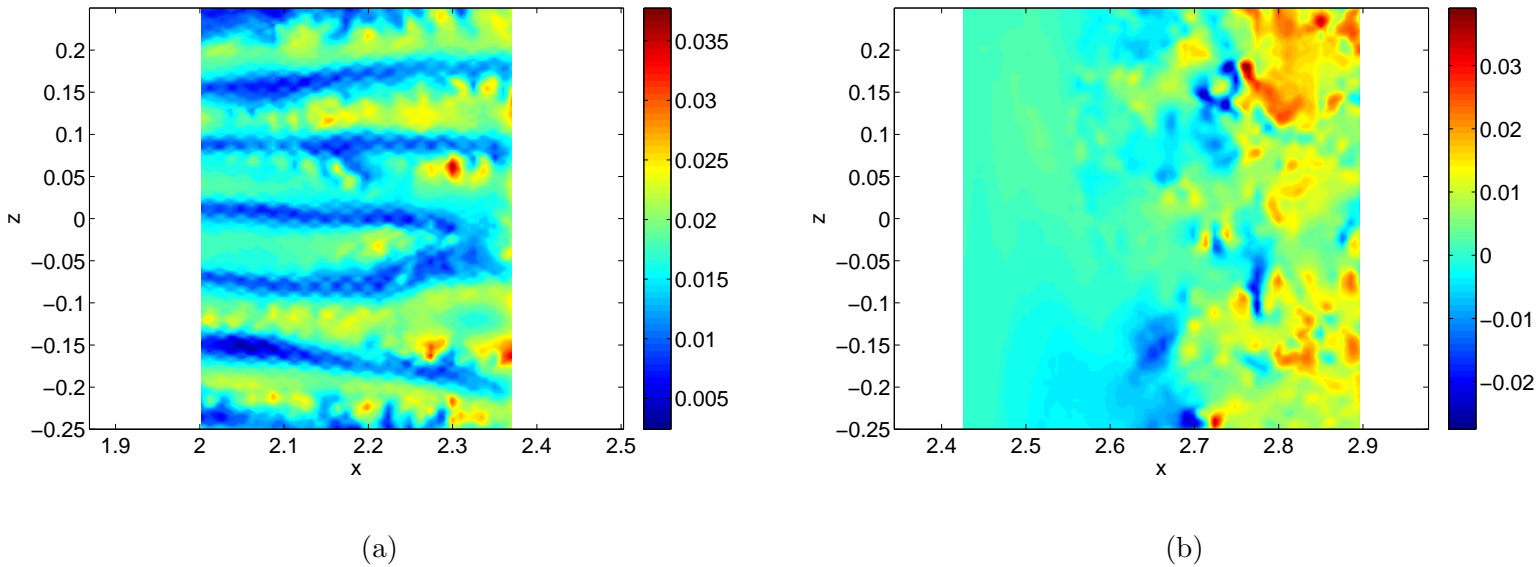


Figure 7.22: Contour plots of instantaneous C_f : (a) Upstream of the step edge (b) Downstream of the step edge

Chapter 8

Structural Analysis of the Step Flow Simulation

This chapter of the thesis analyzes the structural make-up and dynamics of the fluid which passes from the upstream boundary layer into the separated region and also discusses reattachment.

8.1 Structural Evolution of the Fluid Into the Separated Region

With a simulation which produces a shear layer downstream of the step edge and streamlines in the separated region which curve slowly downward until they reattach to the lower plate downstream of the step edge, the vortical dynamics of the flow along this shear layer can be examined and the results compared to flow over a step with straight edges.

The shear layer which emanates from the step edge rolls-up along its length [13]. In the separated zone, this roll-up of the shear layer produces roller vortices¹ as can be seen from Figure 8.1. In this figure, roller vortices are clearly present downstream of the step edge. In addition, the vortex tubes simulated by the GVFS conform to the shape of the roller vortices as can be seen by observing Figure 8.2, which plots vortex tubes and isosurfaces of $\Omega_z = -55$ from narrow slices at three different spanwise locations.

¹The plots of isosurfaces of vorticity displayed in this chapter were generated from meshes tailored to illuminate the presence of structures at or near the shear layer in the separated region.

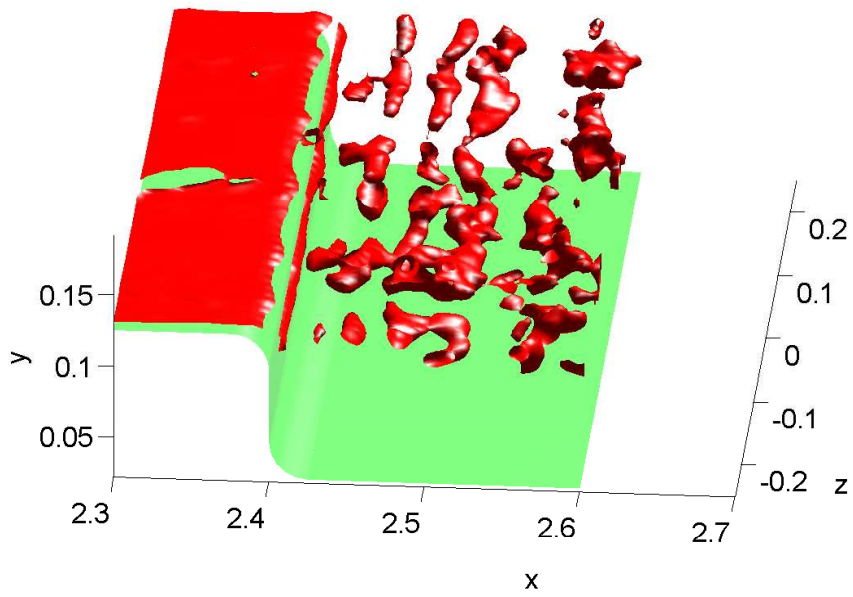
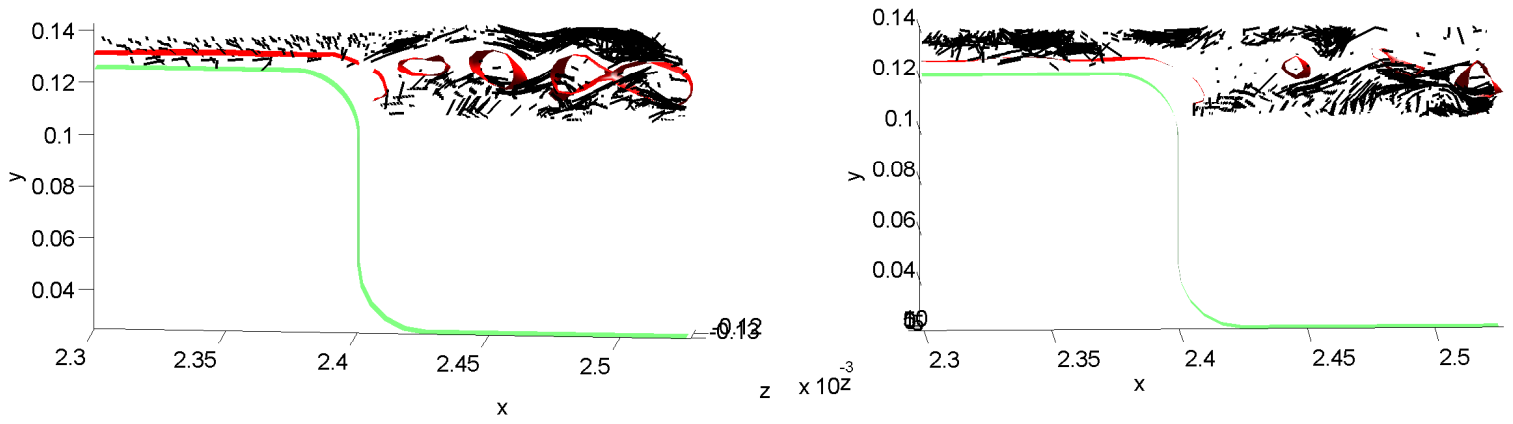
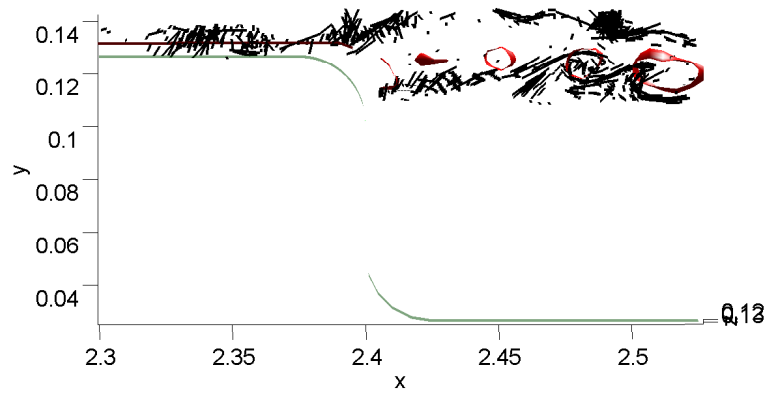


Figure 8.1: Isosurfaces of $\Omega_z = -55$ at time $t = 5.82$



(a)

(b)



(c)

Figure 8.2: Isosurfaces of $\Omega_z = -55$ along with plots of the vortex tubes from time $t = 5.82$ located within: (a) $z = -0.1275 \pm 0.005$ (b) $z = 0.0 \pm 0.005$ (c) $z = 0.125 \pm 0.005$

Because vortex lines move with the local fluid velocity when removed from viscous effects near solid boundaries [33, 63], the roll-up of the vortex lines in the shear layer can be illuminated by inserting particles into the flow which advect along with the local fluid velocity at a location surrounding part of a roller vortex and tracking these particles backward in time. To that end, Figure 8.3a displays a plot of isosurfaces of Ω_z which highlight the approximate location of the roller vortices in the shear layer with particle positions superimposed alongside the result of tracking these particles backward in time (Figure 8.3b). In Figure 8.3b, the dotted black line seeks to capture the approximate trend the particles display after they are tracked backward in time. Observation of Figures 8.3a and 8.3b demonstrates that the shear layer does indeed roll-up. Although the upstream set of particles in Figure 8.3b does not unroll exactly due to corrugations in the roller vortices and the nature of the near-turbulent field, this plot nevertheless captures the clear roll-up trend in the shear layer in the separated region. By contrast, Figure 8.3c displays a set of particles which are located above the heart of shear layer. Tracking this set of particles backward in time as in Figure 8.3d reveals that they do not unroll, an indication that the roll-up phenomenon does not regularly occur outside of the shear layer.

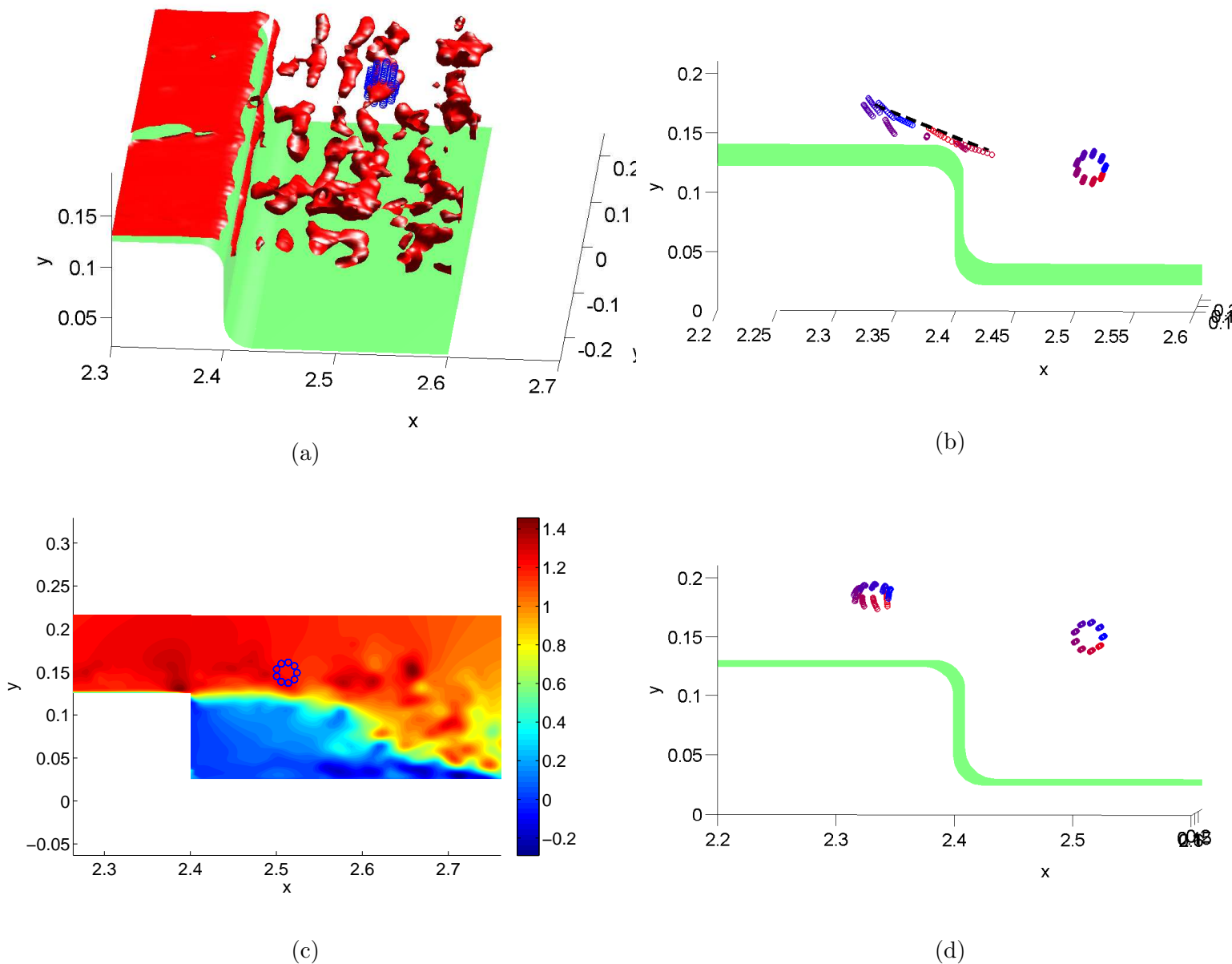


Figure 8.3: (a) Initial particle positions placed to approximately coincide with part of a roller vortex (b) Same particle positions as (a) along with the positions of those particles tracked backward in time, the particles in this figure are color-coded so that they are easier to keep track of and the dotted black line describes the approximate trend the particles display when they are tracked backward in time (c) Initial particle positions projected onto a contour plot of streamwise velocity, these particle positions are placed above the heart of the shear layer (d) Same particle positions as (c) along with the positions of those particles tracked backward in time, the particles in this figure are also color-coded

Examination of Figure 8.3a reveals that some of the isosurfaces of spanwise vorticity contain spanwise gaps. These gaps can be explained by inspecting Figure 8.4b, in which particles were placed at the endpoints of vortex tubes which surround two parts of a roller vortex with a spanwise gap (located around $z = 0.0875$) in the middle. Because the vortex tube endpoints advect with the local fluid velocity, inserting particles into the flow at vortex tube endpoints provides a means to roughly track the motions of the tubes which are removed from the viscous effects present near solid boundaries [63]. In this vein, the particles in Figure 8.4b were then tracked backward into the upstream boundary layer based on the local fluid velocity as a way of approximating the motion of the vortex tubes. A cut through these particles in a $z-y$ plane was superimposed on a plot of the vortex tubes from the same plane and time (Figure 8.4d). The particles in Figure 8.4d do not overlap exactly with the vortex tubes because the use of particles as an approximation of the motion of the tubes does not take into account vortex splitting and loop removal. However, observation of Figure 8.4d reveals that the gap between the sets of particles in Figure 8.4b occurs as a result of the lack of vorticity in the stem of the mushroom between the two sets of particles in Figure 8.4d. Figure 8.5, which plots isosurfaces of spanwise vorticity with vortex tubes above these isosurfaces superimposed, helps to elucidate this same phenomenon across the span in that most of the gaps in the isosurfaces lie beneath the stems of mushroom-like structures which largely lack vortex tubes.

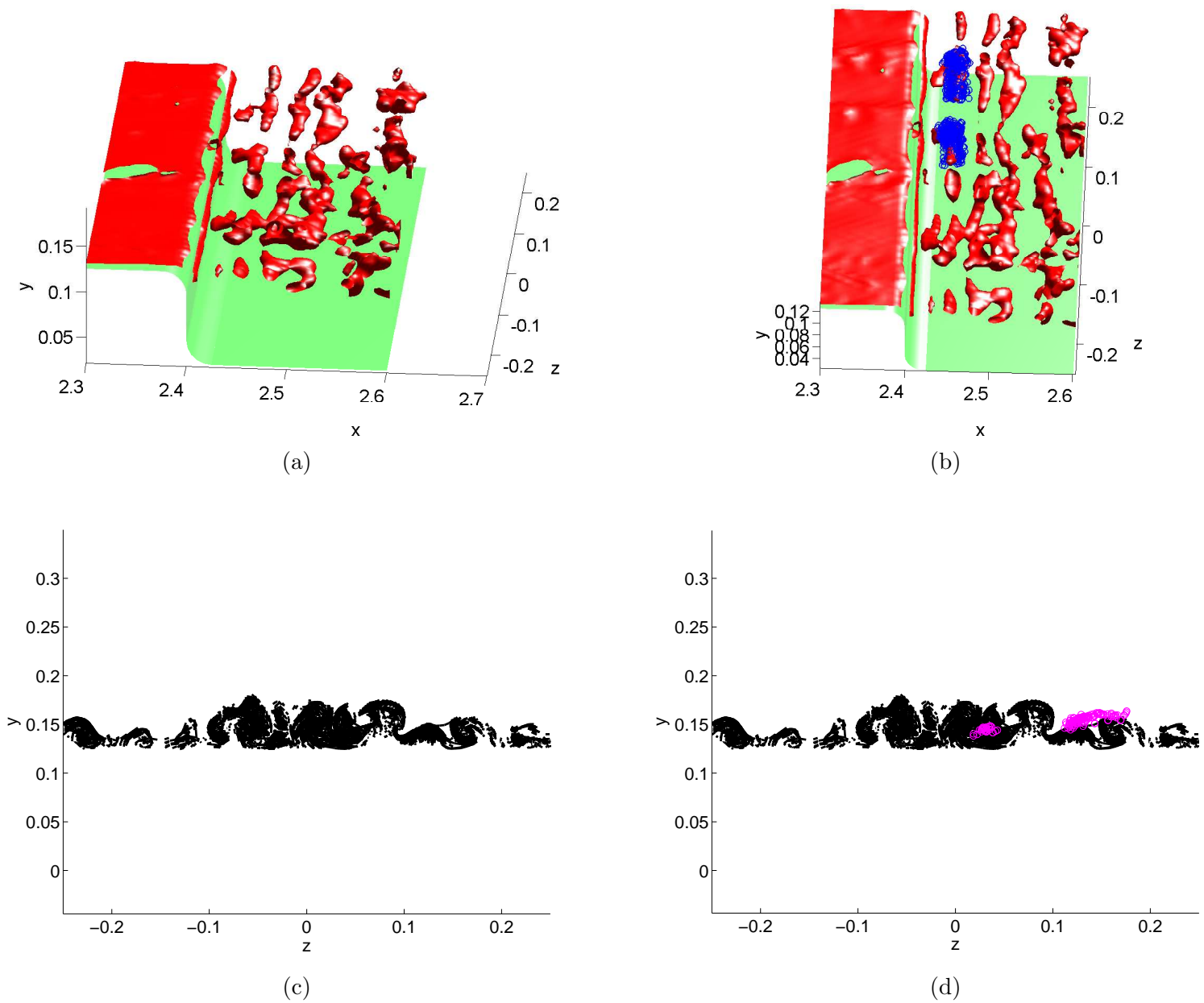


Figure 8.4: (a) Isosurfaces of spanwise vorticity revealing the presence of roller vortices (b) Same plot as (a), with the endpoints of vortex tubes which surround part of a roller vortex with gaps, plotted as particles (c) Plot of vortex tubes in a $z - y$ plane in the upstream boundary layer (d) Same plot as (c) with positions of a slice through the particles from (b) tracked backward in time superimposed

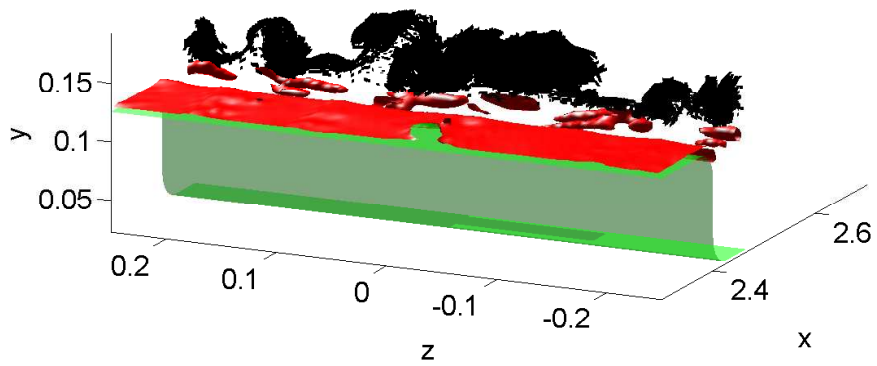
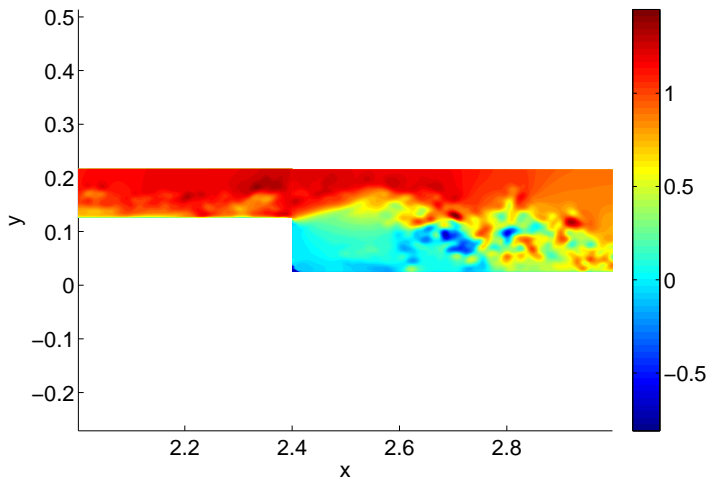
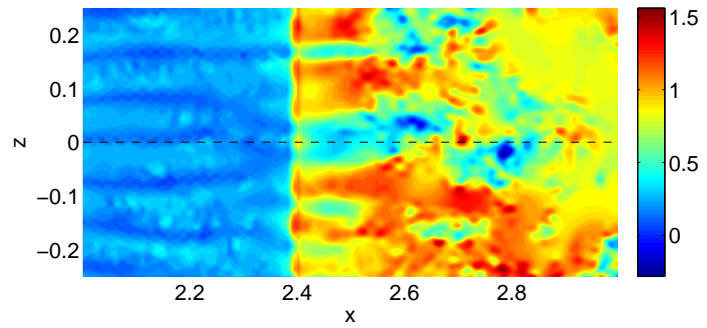


Figure 8.5: Isosurfaces of spanwise vorticity with vortex tubes above these isosurfaces superimposed

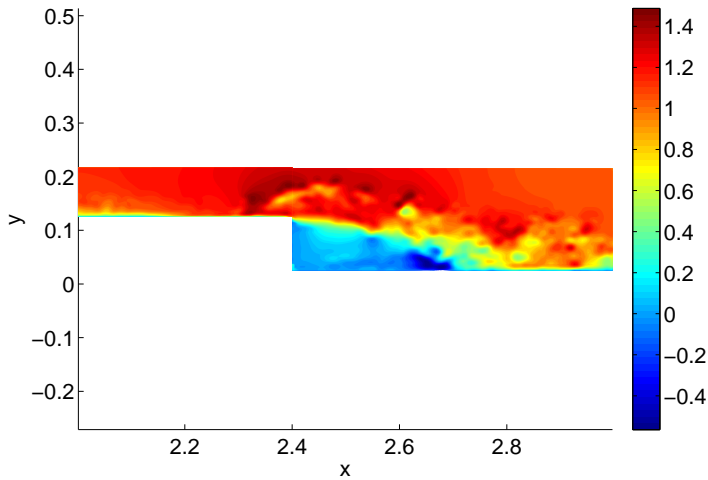
Figure 8.5 can also be related to another phenomenon present in flow over a backward-facing step as follows: a number of researchers [13, 18, 11] have noted the presence of low-frequency oscillatory motions in the step flow. These low-frequency motions include flapping of the shear layer and oscillations of the instantaneous reattachment point which may point to periodic motions of the entire recirculation region. Coming back to Figure 8.5, one can note that mushroom-shaped structures generally overlie low-speed streaks and upward-moving fluid as the counter-rotating motions induced by the lobes of the mushrooms lift low-speed fluid upward. As the furrows in the upstream boundary layer shift in time, the positions of the low-speed streaks which protrude into the separated zone also shift. These shifts in the positions of the furrows therefore alter the direction of the separating shear layer at a given point across the span as low-speed streaks accompany upward-moving fluid and the regions between the streaks accompany downward-moving fluid due once again to the motion induced by the lobes of the mushroom-like structures. In line with these ideas, Figure 8.6 displays flapping of the shear layer at $z = 0$. Figure 8.6a displays a shear layer emanating from the step edge which is directed upward and the contour plot in Figure 8.6b reveals that at this instant in time $z = 0$ coincides with the continuation of low-speed streaks which extend over the edge of the step. Figure 8.6c, on the other hand, displays a shear layer which is directed downward and Figure 8.6d reveals that at this later instant in time $z = 0$ lies between the continuation of the low-speed streaks.



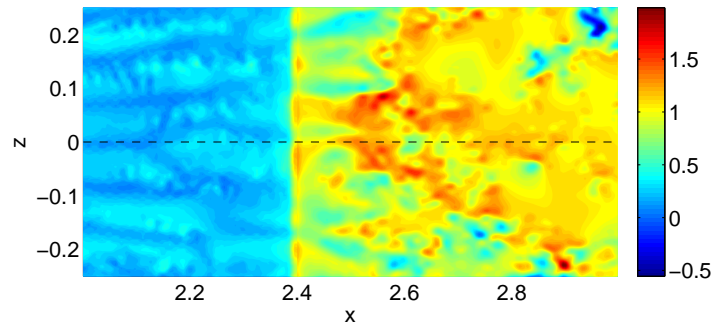
(a)



(b)



(c)



(d)

Figure 8.6: Contour plots of U at: (a) time t_1 in the plane $z = 0$ (b) time t_1 in the plane $y = 0.127$; runs through $z = 0$ (c) later time t_2 in the plane $z = 0$ (d) time t_2 in the plane $y = 0.127$; runs through $z = 0$

With the origins and creation of the roller vortices explained as described above, it is worthwhile to next investigate how these vortices break up. The break-up of these vortices can also be examined through the use of particle trajectories. To that end, Figures 8.7 and 8.8 cover two different parts of a roller vortex with two different sets of particles and plot their subsequent projected positions on top of 2D streamlines and contour plots of streamwise velocity of a nearby plane. Examining the trajectories of both sets of particles one can conclude that the shear layer, which is responsible for the roll-up into coherent structures in the separated zone, is also responsible for the break-up of the roller vortices as these vortices get sheared away by the wall-normal gradient in streamwise velocity. The streamlines in Figures 8.7 and 8.8 help to elucidate the idea that the curvature of the upper step corner bends the streamlines in the shear layer slightly downward, which therefore imparts a slightly downward trajectory to the particles displayed in the plots.

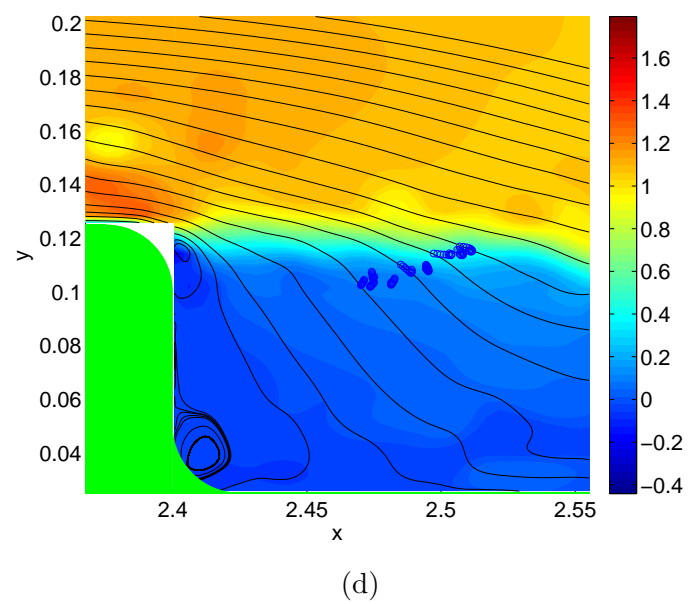
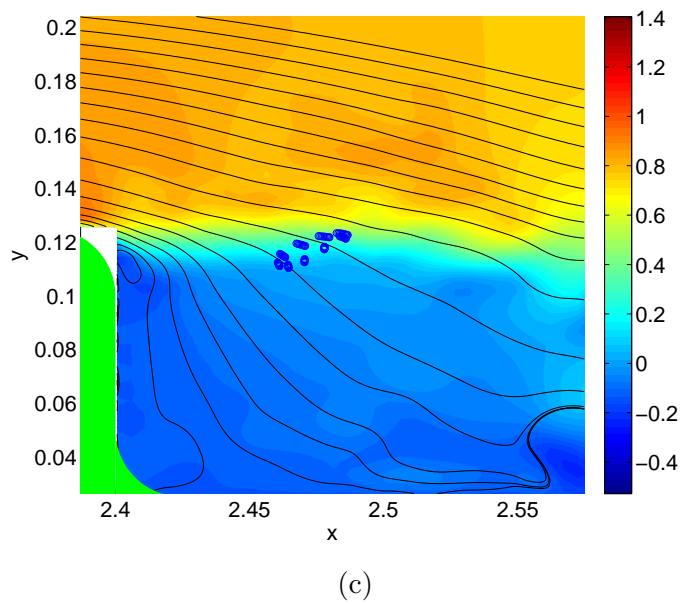
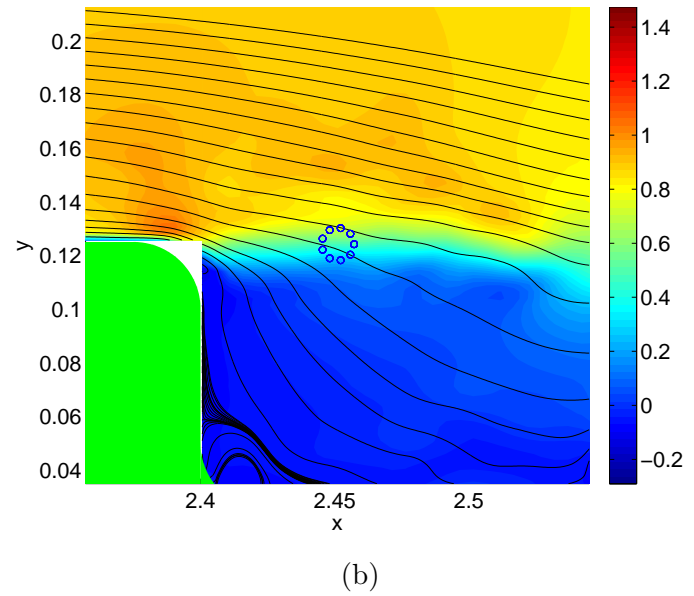
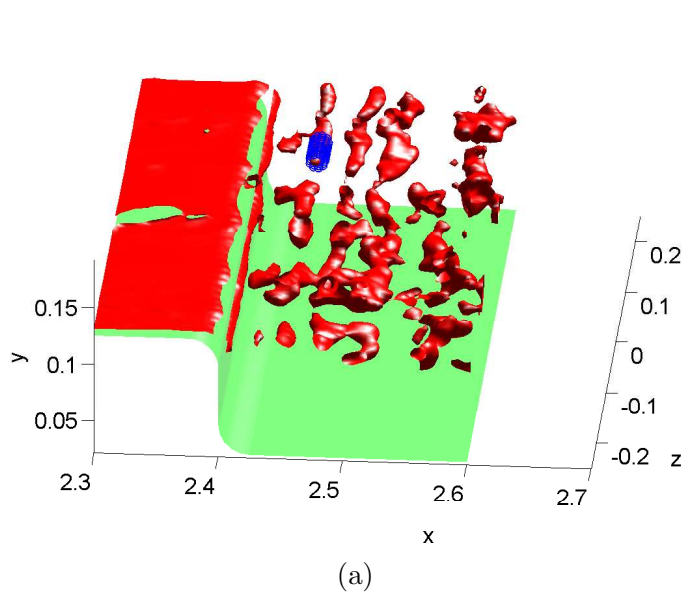
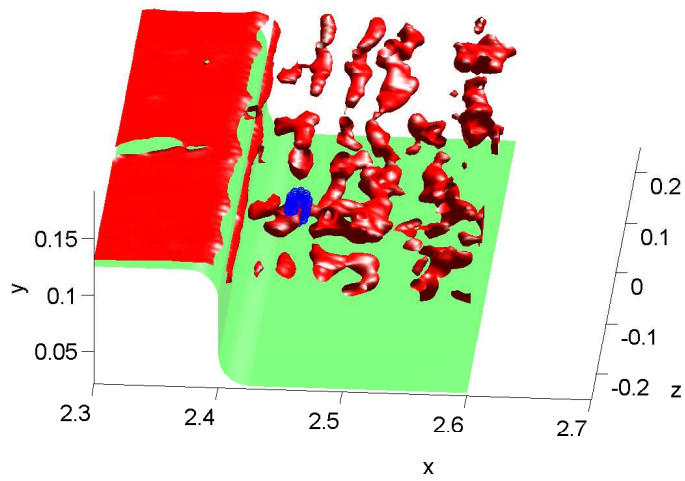
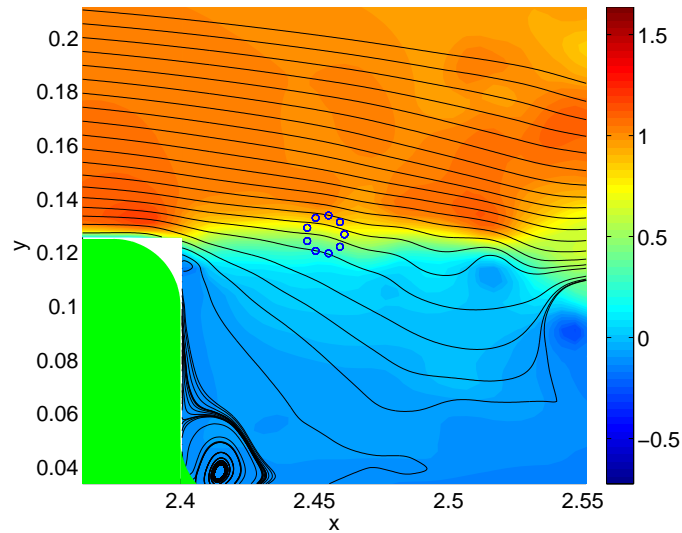


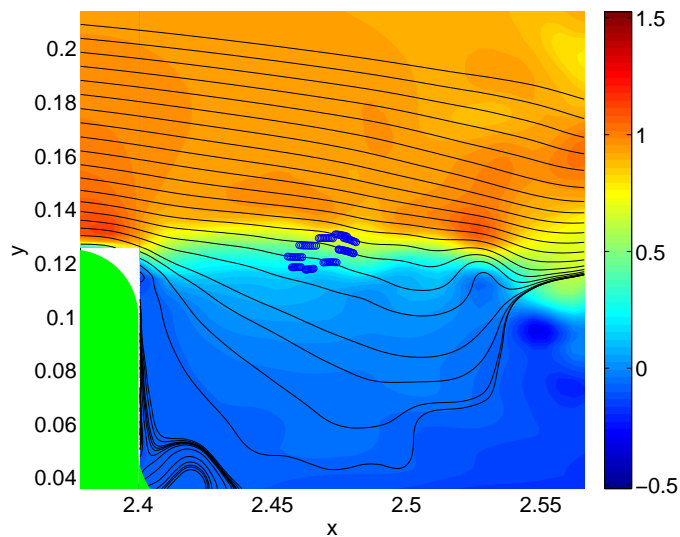
Figure 8.7: Demonstration of how the shear layer breaks up a roller vortex: (a) Particles covering part of a roller vortex (b)-(d) Subsequent evolution of the particles in (a) projected onto 2D streamlines and contour plots of streamwise velocity of nearby planes



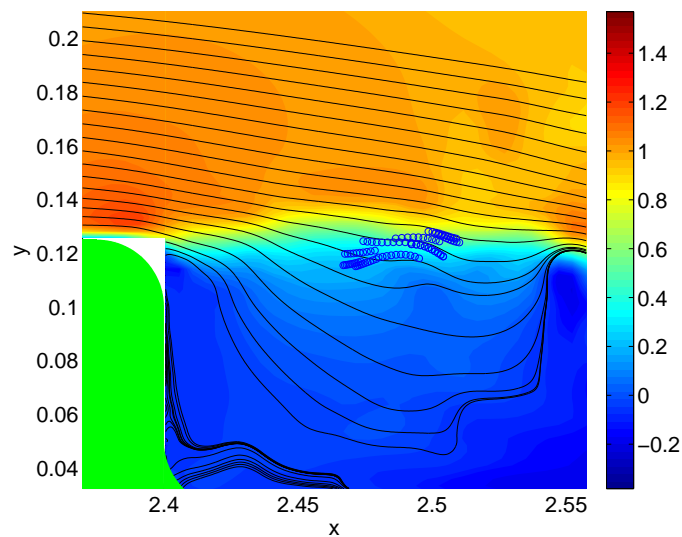
(a)



(b)



(c)



(d)

Figure 8.8: Same plots as Figure 8.7 except that the particles in this figure cover a different part of the roller vortex than in Figure 8.7

It is also worth noting that traditional mixing layers contain streamwise-aligned rib vortices in the braid region between the roller vortices [58]. Figure 8.9, which plots isosurfaces of negative Ω_z and positive and negative Ω_x , demonstrates that rib vortices begin to form slightly downstream of $x = 2.5$, but a full-fledged braid region with a set of rib vortices which wrap underneath their upstream roller and on top of their downstream roller and alternate across the span [129] does not exist. A simulation with a longer separation length and perhaps streamlines which more directly align with the streamwise direction in the separated region (i.e. flow over a step with straight edges) would generate a mixing layer which contains rib vortices spaced out across the span. Silveira Neto et. al. [94], in their simulations of flow over a backward-facing step with straight edges, generated roller vortices and alternating rib vortices spaced out across the span downstream of the step edge.

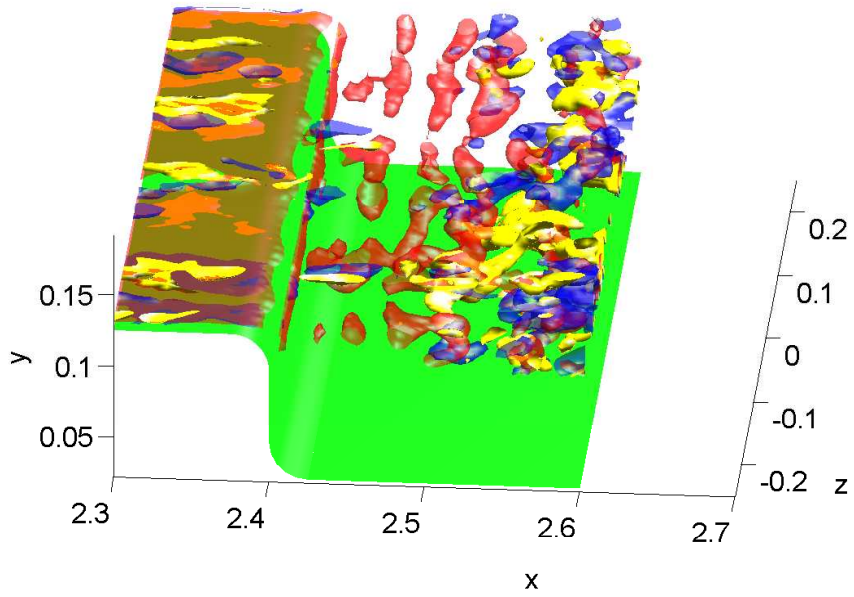


Figure 8.9: Isosurfaces of $\Omega_z = -55$ (red), $\Omega_x = -30$ (blue), $\Omega_x = 30$ (yellow) in the separated region

8.2 Reattachment

As was illustrated by Figure 7.9, the instantaneous reattachment line across the span is illuminated by contour plots of streamwise velocity in $y=\text{constant}$ planes near the lower plate. In these plots, the reattachment line occurs where there is a marked shift from slower-moving fluid/backflow to faster-moving fluid. An investigation was undertaken to examine the behavior of the fluid in the vicinity of reattachment in order to try and determine if a connection might exist between the configuration of the instantaneous reattachment line and the structural make-up of the boundary layer upstream of the step edge. To that end, Figure 8.10 advects particles backward in time which were placed in the vicinity of reattachment and possessed a spanwise configuration which approximately matches where the slower-moving fluid meets the faster-moving fluid. The particles in Figure 8.10 are color-coded based on their spanwise positions in the first image so as to make it easier to track the particles when they are advected backward in time. The images move backward in time when progressing from Figure 8.10a to Figure 8.10e. The instantaneous line as depicted by the particles in Figure 8.10a approximately draws a dividing line between the fluid upstream of the particles which is destined to interact with the lower plate beneath the separated region and the fluid downstream of the particles which is destined to move off downstream along the lower plate. Observation of Figure 8.10a reveals that the instantaneous line of particles in this figure protrudes slightly forward in the downstream direction around $z = 0$. Observation of Figures 8.10b and 8.10c demonstrates that the line of particles still approximately tracks where slower-moving fluid meets faster-moving fluid and that the particles still protrude slightly forward near the center of the span. In Figure 8.10d the particles have largely migrated back to a wall-normal position above the upper plate (the upper plate lies at $y = 0.125$) and still possess a spatial configuration which protrudes forward toward the center of the span. In Figure 8.10e, the particles still protrude forward toward the center of the span and many of the particles have migrated upstream of the step edge (the step edge lies at $x = 2.4$). In Figure 8.10e, the purple and blue particles which are situated near the center of the span and upstream of the step edge are located within relatively fast-moving fluid. By contrast the red and blue particles which lie toward either side of the span and upstream of the step edge are located within fluid that moves less fast than the purple and blue particles which are located in the center of the span and upstream of the step edge.

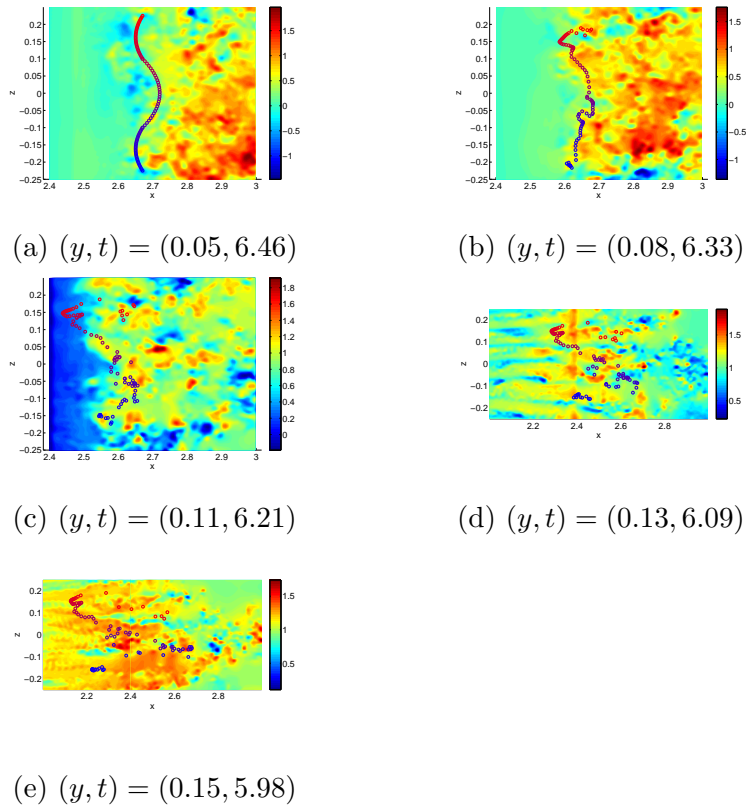


Figure 8.10: Particles inserted into the flow in the vicinity of reattachment (the lower plate lies at $y = 0.025$) and advected backward in time and projected onto contour plots of streamwise velocity from y -constant planes near to the particles; the particles are color-coded according to their spanwise positions in the first plot

The reason behind the configuration in Figure 8.10e is revealed by examining Figure 8.11. Figure 8.11a re-prints the particles which lie upstream of the step edge in Figure 8.10e on top of a contour plot of streamwise velocity from a plane ($y = 0.175$) determined by averaging the y positions of the particles in Figure 8.10e which lie upstream of the step edge. Figure 8.11b displays a plot of vortex tubes in the plane $x = 2.35$. Figure 8.11c superimposes the same particles from Figure 8.11a onto a contour plot of streamwise velocity also in the plane $x = 2.35$. Figure 8.11d displays a plot of spanwise vorticity also in the plane $x = 2.35$. The dotted blue lines in Figure 8.11 connect the y -constant plane in Figure 8.11a to the x -constant planes in Figures 8.11b, 8.11c, 8.11d. A comparison of Figures 8.11a and 8.11c tends to show that the red and blue particles which are situated in relatively slower-moving fluid toward either side of the span in Figure 8.11a lie between patches of ejecting low-speed fluid in Figure 8.11c. For instance, in Figure 8.11c the blue particles which are situated around $z = -0.15$ lie between the patches of ejecting low-speed fluid positioned at approximately $z = -0.18$ and $z = -0.075$. By contrast, the purple particles which lie toward the center of the span and are immersed in relatively faster-moving fluid in Figure 8.11a tend² to lie above ejecting low-speed fluid. For instance, the purple particles in Figure 8.11c which lie around $z = 0.085$ are located above a patch of ejecting low-speed fluid which is also positioned at around $z = 0.085$.

The fluid above an ejecting low-speed streak is faster than the fluid between ejecting low-speed streaks because the mushroom-like structures which overlie low-speed streaks contain negative spanwise vorticity in their arches. These arches containing negative spanwise vorticity, in accordance with the Biot-Savart law, contribute to creating slower-moving fluid beneath the arches and faster-moving fluid above the arches. This effect can be seen in Figures 8.11c and 8.11d at around $z = 0.085, y = 0.16$ in which a band of negative spanwise vorticity helps to create slower-moving fluid beneath around $y = 0.16$ and faster-moving fluid above around $y = 0.16$. A comparison of Figures 8.11d and 8.11b demonstrates that the band of negative spanwise vorticity located at around $z = 0.085, y = 0.16$ indeed coincides with the arch of a mushroom-like structure.

The preceding arguments tend to explain the particle arrangement in

²A comparison of Figures 8.11a and 8.11c shows that many of the purple particles which coincide with an ejecting patch of slow-moving fluid around $z = 0$ are located close to the step edge ($x = 2.4$) so that these particles are destined to move further away from the upper plate if they are advected further back in time.

Figure 8.11a in which particles toward either side of the span lie upstream of the particles which lie toward the center of the span, a spanwise configuration which also exists in the vicinity of reattachment. Taking Figures 8.10 and 8.11 together suggests that the spanwise configuration of the reattachment line has its origins in the structural make-up of the fluid upstream of the step edge. This potential connection is used to suggest an area for future research in Chapter 10 of the thesis.

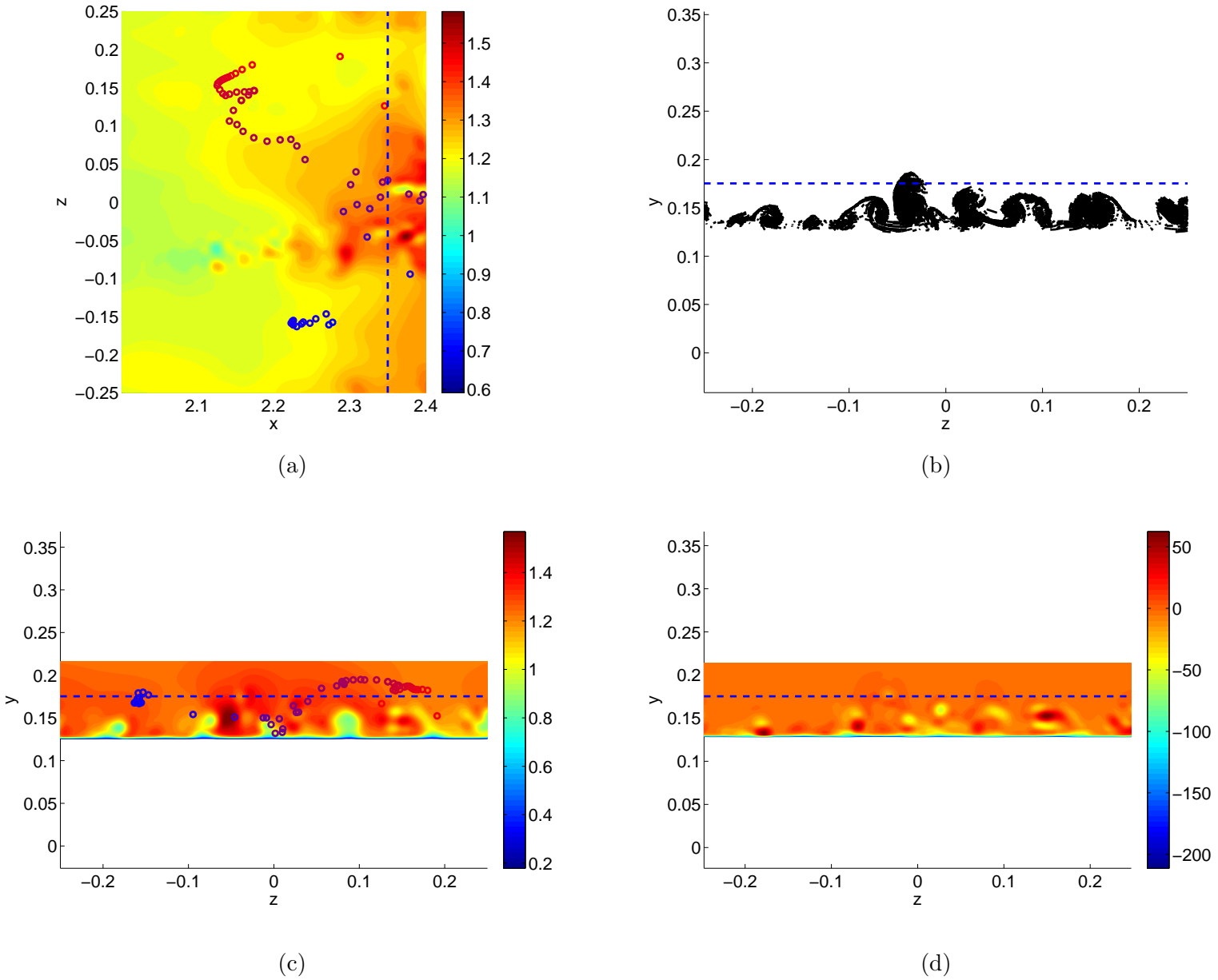


Figure 8.11: All images in this figure taken from the same time as in Figure 8.10e, $t = 5.98$: (a) Contour plot of streamwise velocity in the plane $y = 0.175$ with the particles from Figure 8.10e which lie upstream of the step edge superimposed (b) Vortex tubes from the plane $x = 2.35$ (c) Contour plot of streamwise velocity in the plane $x = 2.35$ with the same particles from (a) superimposed (d) Contour plot of spanwise vorticity in the plane $x = 2.35$; $\dots\dots\dots$ connects the y -constant plane in (a) with the x -constant planes in (b), (c), (d)

Chapter 9

Summary and Conclusions

The step flow is a geometry designed to study the physics of flow separation, reattachment, recirculation, and recovery and in this thesis a vortex filament scheme (the GVFS) was used to simulate flow over a backward-facing step with curved edges. Vortex filament methods utilize vortex tubes as their main computational element in order to depict the complete vortical structure of a flow. In order to improve the way in which the GVFS simulated the way the fluid separated from the step, vortex tubes were inserted into the flow from the near wall mesh based on local vorticity downstream of the step edge (the vortex insertion scheme).

This thesis offers a number of conclusions. Utilizing plots of isosurfaces of spanwise vorticity and particles which advect with the local velocity it was demonstrated that the fluid which moves from the upstream boundary layer into the shear layer in the separated region rolls-up to form roller vortices. It was also demonstrated that these same roller vortices, when viewed through the lens of isosurfaces of spanwise vorticity, extended across the span but possessed spanwise gaps. These spanwise gaps underlie mushroom-like structures. These mushroom-like structures are, in turn, extensions of the furrows in the upstream boundary layer that have convected over the step edge into the separated region. It was also discovered that changes in the positions of the furrows in the upstream boundary layer cause flapping of the shear layer in that extensions of the furrows into the separated region direct the shear layer upward whereas the regions between the furrows direct the shear layer downward. It was in addition also determined that the shear layer in the separated region, which is responsible for the roll-up of the fluid into roller vortices, also serves to break up these vortices through the actions

of shearing motions.

Overall, using a vortex filament method to simulate flow over a backward-facing step helped to provide a complete picture as to how the extensions of furrows which convect over the step edge interact with roller vortices in the separated region. Connecting the furrows to the roller vortices in this way illustrates the connection between the upstream boundary layer structure and the mixing layer structure which results from separation.

Chapter 10

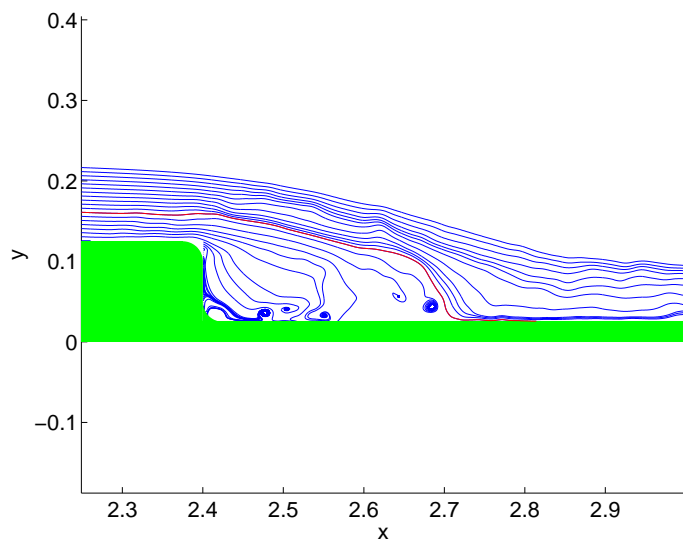
Suggestions for Future Work

This chapter discusses a potential idea for how the current research problem might be extended.

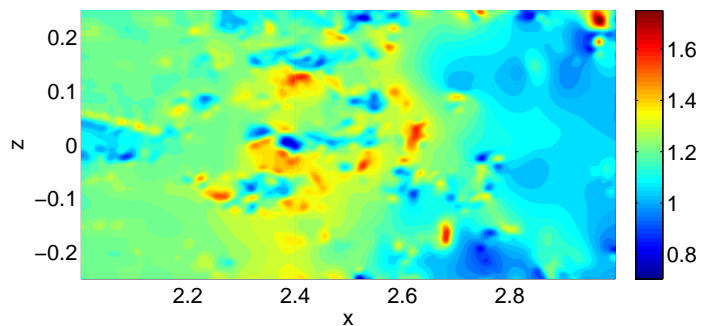
10.1 Effect of the Curved Step Edge on the Flow Pattern in the Present Simulation

As was alluded to in Chapter 7.2, the rounded upper step corner of the step geometry used in the present simulation imparts a downward trajectory to the fluid which flows around it. Because of this effect, the fluid at reattachment emanates from a wall-normal height in the upstream boundary layer which lies above the clearly-defined spanwise structure of the low-speed streaks.

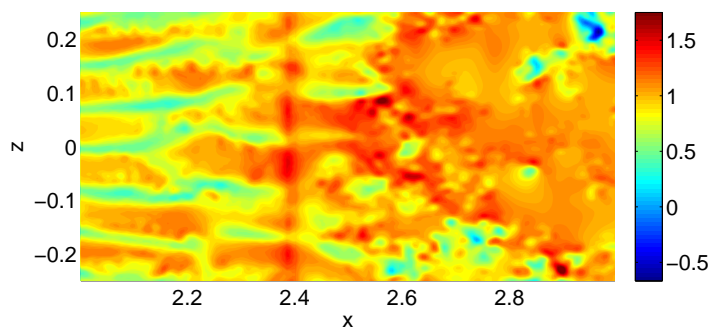
As evidence of this assertion, Figure 10.1a displays 2D, instantaneous streamlines in the plane $z = 0$ at time $t = 6.46$ with the approximate reattaching streamline outlined in red. This red streamline emanates from the upstream boundary layer at a wall-normal height of roughly $y = 0.161$. Figure 10.1b then displays a contour plot of streamwise velocity in the plane $y = 0.161$, also at time $t = 6.46$. Figure 10.1b is clearly taken from a wall-normal height above the low-speed streaks. For comparison purposes, Figure 10.1c displays a contour plot of streamwise velocity in the plane $y = 0.1275$ in which the low-speed streaks are clearly visible.



(a)



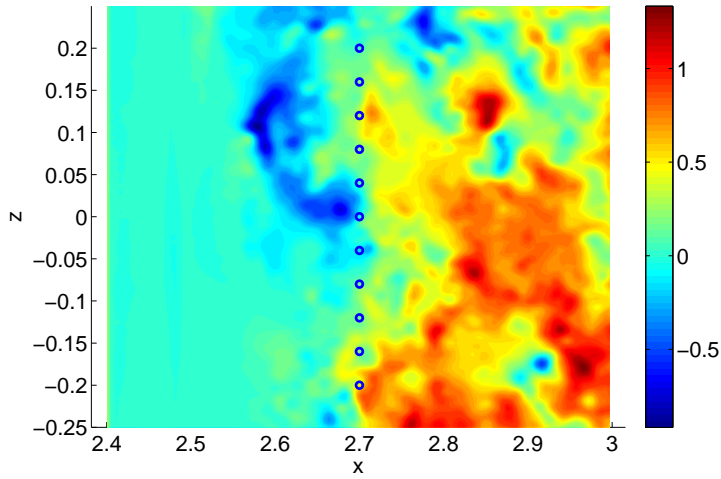
(b)



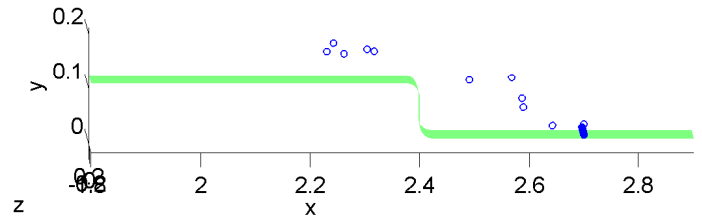
(c)

Figure 10.1: All plots taken from time $t = 6.46$: (a) 2D streamlines from the plane $z = 0$ with the approximate reattaching streamline highlighted in red which emanates from a wall-normal height in the upstream boundary layer of $y = 0.161$ (b) Contour plot of streamwise velocity in the plane $y = 0.161$ (c) Contour plot of streamwise velocity from the plane $y = 0.1275$

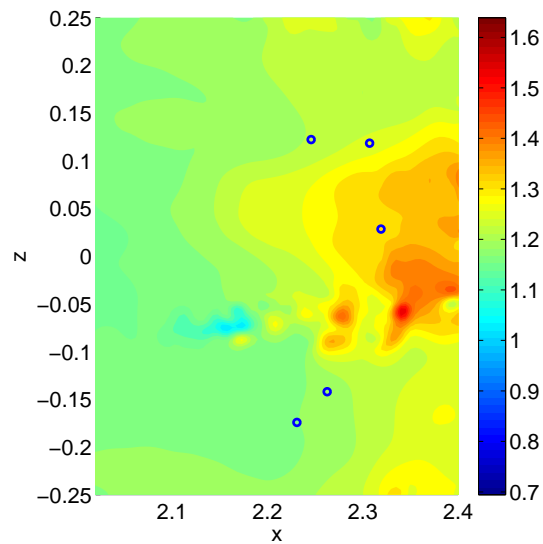
As another way of demonstrating that the fluid at reattachment emanates from a wall-normal position in the upstream boundary layer above the low-speed streaks, Figure 10.2a shows the positions of particles inserted in the flow at reattachment, $x = 2.7$, $y = 0.03$, at time $t = 6.46$ (same time as the streamline plot in Figure 10.1a). These particles were tracked backward in time to $t = 6.02$ based on advection by the local fluid velocity and the 3D results of this calculation are displayed in Figure 10.2b. Those particles in Figure 10.2b which tracked backward upstream of the step edge were superimposed on a contour plot of streamwise velocity from the plane $y = 0.1763$ (Figure 10.2c). This wall-normal height for the contour plot in Figure 10.2c was chosen to be near the particles which tracked backward upstream of the step edge in Figure 10.2b. Observation of Figure 10.2c demonstrates that the particles which tracked backward upstream of the step edge in Figure 10.2b reside at a wall-normal height above the well-defined spanwise structure of the low-speed streaks.



(a)



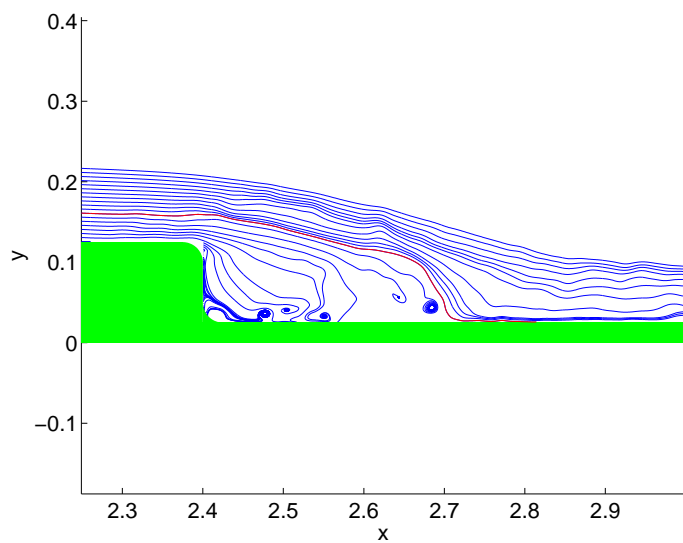
(b)



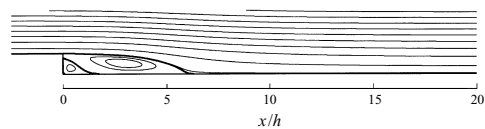
(c)

Figure 10.2: (a) Contour plot of streamwise velocity at time $t = 6.46$ in the plane $y = 0.03$ with a line of particles superimposed at $x = 2.7$, $y = 0.03$ (b) Result of tracking the particles in (a) backward in time to $t = 6.02$ (c) Contour plot of streamwise velocity in the plane $y = 0.1763$ at time $t = 6.02$ with the particles from (b) which tracked back upstream of the step edge superimposed

As was mentioned at the beginning of this chapter, the reason that the reattaching fluid emanates from a point in the upstream boundary layer well above the upper plate is due to the curvature of the upper step corner, which imparts a downward trajectory to the fluid which travels around it. These downward motions, which affect the fluid passing out over the step both near to and farther away from the upper plate, can be seen in Figure 10.1a (Figure 10.1a is reprinted in Figure 10.3a). By contrast, in a step with straight edges, the fluid passes nearly straight out over the step edge, as can be seen by the mean streamlines in a DNS [13] (Figure 10.3b).



(a)



(b)

Figure 10.3: (a) 2D streamlines from the plane $z = 0$ with the approximate reattaching streamline highlighted in red (same plot as Figure 10.1a) (b) Mean streamlines in a DNS of flow over a backward-facing step with straight edges [13] (same plot as Figure 7.7c)

10.2 Area for Future Research Involving Reattachment

Because Chapter 8.2 established a tentative connection between the structural composition of the fluid upstream of the step edge and the spanwise configuration of an instantaneous reattachment line in the present simulation, one avenue for future research involving reattachment would be to investigate whether the structure represented by the low-speed streaks spaced out across the span in the upstream boundary layer prior to separation persists into reattachment. Because the step geometry in the present simulation utilizes rounded edges which then generates a flow pattern in which the origins of reattachment lie above the low-speed streaks in the upstream boundary layer, in order to examine the connection between the low-speed streaks and reattachment it is preferable to utilize a step with straight edges in which, as can be seen by examining Figure 10.3b, the fluid adjacent to the upper plate, which presumably contains the low-speed streaks, eventually reaches reattachment. A sketch of what a connection between the low-speed streaks in the upstream boundary layer and reattachment might look like is provided by Figure 10.4. The idea behind Figure 10.4 is that the low-speed streaks reattach to the lower plate slightly upstream of where the faster-moving fluid reattaches.

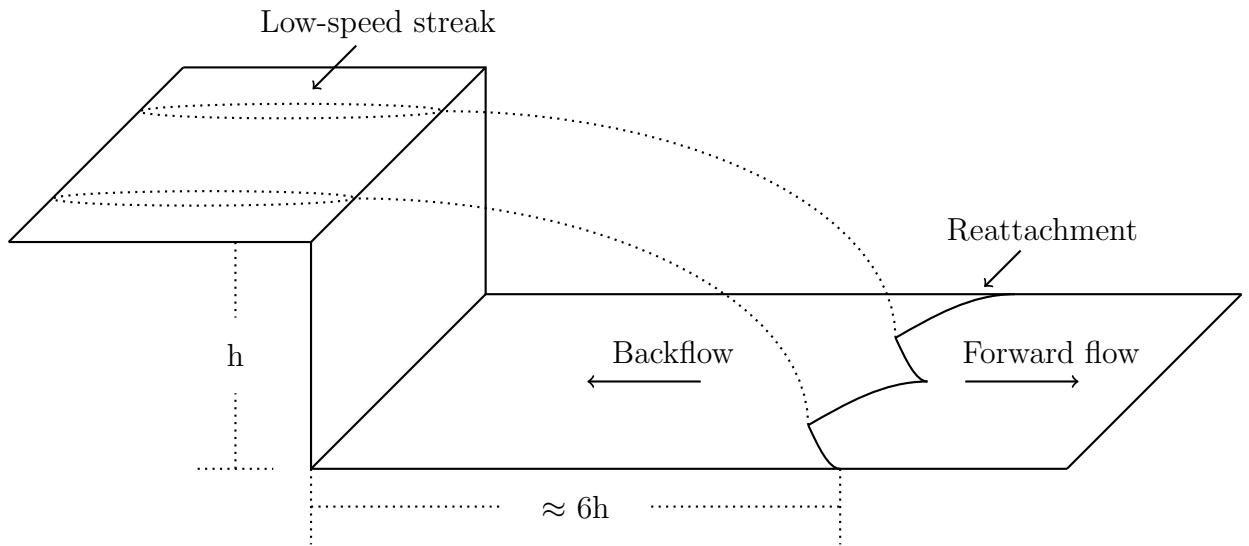


Figure 10.4: Schematic of what a possible connection between the low-speed streaks in the upstream boundary layer and reattachment might look like in a flow over a backward-facing step with straight edges

Appendix A

Adverse Pressure Gradient Turbulent Boundary Layers

As mentioned at the beginning of Chapter 4, an adverse pressure gradient (APG) occurs in the step flow downstream of the step edge as a result of the step expansion. Although the APG in the step flow occurs in and around the reattachment region [13], it can be helpful, when studying the step flow, to acquire some familiarity with the characteristics of adverse pressure gradient turbulent boundary layers (APGTBLs), in order to determine if there are any similarities between the most downstream region of the step flow where an APG exists and APGTBLs, and to see if any of the characteristics of APGTBLs extend into the part of the recovery region where pressure gradients cease to exist. And although the present thesis does not utilize the information in this appendix, further investigations into the step flow may require knowledge of the basic characteristics of APGTBLs.

Before proceeding to a discussion of equilibrium and similarity in turbulent boundary layers with pressure gradients, it is worth noting that many researchers generate APGTBLs through the use of expanding channels or decreasing free-stream velocity rather than as a result of a sudden expansion as in the step flow. However, it is still worthwhile to review the characteristics of APGTBLs even if they are generated in ways different than in the step flow.

A.1 Equilibrium and Similarity in TBLs with Pressure Gradients

Clauser [47] conducted an analytical and experimental investigation into APGTBLs. Clauser described equilibrium boundary layers as those which produce equivalent wall-normal mean velocity and turbulent profiles (plotted with appropriate scalings) as one moves downstream (this is the phenomenon of similarity [33]). Clauser noted that these conditions for equilibrium might be impossible to realize in practice. In addition, Clauser identified the two important forces acting on boundary layers to be the force resulting from pressure gradients and the force resulting from the viscous shear stress exerted upon the fluid at the wall. He quantified the streamwise force per streamwise unit length per spanwise unit length resulting from pressure gradients as $\delta'(dp/dx)$, where δ' is an undetermined wall-normal length scale of the boundary layer. He then noted that if the ratio of streamwise force per streamwise unit length per spanwise unit length resulting from pressure gradients to the ratio of streamwise force per streamwise unit length per spanwise unit length resulting from the wall viscous shear stress for a particular boundary layer, $(\delta'/\tau_w)(dp/dx)$, remains constant with downstream distance, then that boundary layer is in equilibrium.

Clauser also sought to identify appropriate metrics and scales of boundary layers. He identified the following “thickness”:

$$\Delta = \int_0^\infty \frac{U_\infty - \bar{U}}{U_\tau} dy \quad (\text{A.1})$$

in which Δ/δ remains constant for a given equilibrium boundary layer. In addition, he identified another parameter, which he called G , which is defined along somewhat the same lines as the shape factor [1], $H = \delta^*/\theta$ (where δ^* is displacement thickness and θ is momentum thickness)¹. Clauser defined the parameter, G , as:

$$G = \frac{\int_0^\infty \left(\frac{U_\infty - \bar{U}}{U_\tau}\right)^2 dy}{\int_0^\infty \frac{U_\infty - \bar{U}}{U_\tau} dy} \quad (\text{A.2})$$

Lee and Sung [50], in their direct numerical simulation of APGTBLs, apparently interpreted Clauser’s [47] paper as meaning that when the parameter

¹Clauser [47] noted that the shape factor, H , is approximately 1.3 for ZPGTBLs and approximately 2.5 for separating turbulent boundary layers

they call β , where $\beta = (\delta^*/\tau_w)(dp/dx)$, and G (defined in Equation A.2) remain constant for a turbulent boundary layer with increasing downstream distance, the boundary layer is in equilibrium, in which case the profiles of $(U_\infty - \bar{U})/U_\tau$ versus y/Δ (with Δ defined by Equation A.1) should be constant with increasing downstream distance.

It is important to point out that Clauser's definition of equilibrium is not realized by the majority of experiments [48, 49]. Castillo and George [49] conducted an analytical investigation of the outer region of turbulent boundary layers subject to pressure gradients and came up with a new definition of equilibrium. These researchers defined equilibrium turbulent boundary layers as those in which Λ remains constant with downstream distance, where Λ is defined as:

$$\Lambda = -\frac{\delta}{U_\infty} \frac{dU_\infty}{d\delta/dx} \frac{dU_\infty}{dx} \quad (\text{A.3})$$

These researchers noted that most experimental turbulent boundary layers are in equilibrium using this definition. However, Castillo and George noted that this new definition of equilibrium does not imply that the velocity profiles, when plotted as $(U_\infty - \bar{U})/U_\infty$ versus y/δ , will collapse for finite Reynolds numbers, but instead implies that these profiles will converge toward an infinite Reynolds number asymptotic velocity profile. But when Castillo and George plotted the data of other researchers (one plot for APGTBLs and one plot for FPG² TBLs) using the velocity scale offered by Zagarola and Smits [51], $\frac{U_\infty - \bar{U}}{U_\infty \frac{\delta^*}{\delta}}$, versus y/δ , the plot of the APGTBL data collapsed and the plot of the FPGTBL data collapsed. Castillo and George took this to mean that these profiles ($\frac{U_\infty - \bar{U}}{U_\infty \frac{\delta^*}{\delta}}$ versus y/δ) represent the outer boundary layer velocity profiles in the limit as the Reynolds number goes to infinity.

A.2 Statistical Characteristics of APGTBLs

For APGTBLs, when the mean streamwise velocity, scaled by wall variables, is plotted versus wall-normal distance, scaled by wall variables, the relationship $\bar{U}^+ = y^+$ is still valid in the viscous sublayer, but \bar{U}^+ lies below a logarithmic profile in the log layer [52]. However in the wake region, the

²FPG stands for favorable pressure gradient.

fluid's mean velocity in an APGTBL exceeds the fluid's mean velocity of a ZPGTBL [54, 105].

In an APGTBL, $\sqrt{u'^2}/U_\tau$, $\sqrt{v'^2}/U_\tau$, $\sqrt{w'^2}/U_\tau$, and $-\overline{u'v'}/U_\tau^2$, when plotted versus y^+ on a logarithmic scale, all increase with respect to ZPGTBLs, with $\sqrt{u'^2}/U_\tau$ developing a second peak away from the boundary for strong enough APGs [52]. In addition, the viscous sublayer becomes more turbulent as the strength of the APG increases [52]. However, when $\sqrt{u'^2}$, $\sqrt{v'^2}$, and $\sqrt{w'^2}$ are normalized by scales pertaining to the outer part of the boundary layer, these quantities remain approximately the same or decrease with respect to ZPGTBLs [52].

From Clauser's data [47], the skin friction coefficient of an APGTBL varies with the strength of the APG and streamwise distance, but seems to be on the order of $1 \times 10^{-3} - 2 \times 10^{-3}$. Lee and Sung [50], in their DNS of APGTBLs, found that the skin friction coefficient also changes with the strength of the APG and streamwise distance, but that the magnitude of the skin friction coefficient for their test cases varied from around $1 \times 10^{-3} - 3 \times 10^{-3}$.

Another important aspect of APGTBLs is that, for a strong enough APG, turbulent transport of the turbulence occurs in a direction moving toward the solid boundary [53]. In ZPGTBLs, turbulent transport of the turbulence moves outward from the solid boundary [30, 53]. Another facet of the turbulent kinetic energy budget of APGTBLs is that it contains a second peak in turbulent kinetic energy production which occurs in the outer layer of the flow, in addition to the peak near the solid boundary seen in ZPGTBLs [54].

Lee and Sung [50], in their DNS of ZPG and APG TBLs, calculated the budgets for the normal and shear Reynolds stresses (in this case the Reynolds shear stress corresponds to $-\overline{u'v'}$) and displayed plots of these budgets scaled by quantities pertaining to the outer part of the boundary layer. Close to the solid boundary, the components of the Reynolds stress budgets of APGTBLs are about the same or less than that of ZPGTBLs. In the outer layer, the components of the Reynolds stress budgets of APGTBLs and ZPGTBLs differ. For instance, the $\overline{u'^2}$ budget of an APGTBL displays a second production peak in the outer layer. For the $\overline{v'^2}$ and $\overline{w'^2}$ budgets of APGTBLs in the outer layer, the term which produces the most Reynolds stress is the pressure-strain term and the term most responsible for taking it away is the dissipation term. For the Reynolds shear stress budget of an APGTBL in the outer layer, the term which produces the most Reynolds

shear stress is the production term and the term most responsible for taking it away is the velocity pressure gradient term.

A.3 Coherent Fluid Motions in APGTBLs

Lee and Sung [55] published another paper in which they detailed the analysis of direct numerical simulations of APG and ZPG TBLs pertaining to the coherent fluid motions in these boundary layers. They found that low-speed streaks still exist in APGTBLs near the wall, but possess higher momentum than the low-speed streaks in ZPGTBLs. In addition, these researchers found that in APGTBLs, the low-speed streaks are spaced further apart in the spanwise direction than in ZPGTBLs, and on average, the low-speed streaks in an APGTBL are shorter in the streamwise direction than in ZPGTBLs. Lee and Sung also found that in the outer region of APGTBLs, there exist low-momentum regions which are below groups of structures progressing in the streamwise direction which are, according to Lee and Sung, “hairpin-like.” They observed a packet of these hairpin-like entities in an APGTBL. In addition, Lee and Sung presented evidence to support the idea that the legs of the hairpins in APGTBLs are inclined further from the wall than those in ZPGTBLs. They also presented evidence indicating that turbulence in the outer region of an APGTBL is moved toward the solid boundary via the action of spanwise-aligned entities in the log layer.

Nagano, Tsuji, and Houra [56] conducted an experimental investigation into non-equilibrium APGTBLs (most experimentally generated APGTBLs are non-equilibrium [48, 49]). Nagano, Tsuji, and Houra found that, when analyzing the component parts of the Reynolds shear stress, sweeps increase in importance relative to ejections for wall-normal positions from the wall into the log layer of APGTBLs when compared against ZPGTBLs. These researchers noted that this supports the observations that energy moves by turbulent diffusion toward the solid boundary in APGTBLs [53].

Appendix B

Basic Operating Principles of GPUs

This appendix describes some of the basic ideas behind the workings of GPUs as applied to scientific computing purposes¹. It is hoped that the ideas described in this appendix can at some point be put towards efforts to have the GVFS make full use of GPU parallelism.

Traditionally, numerical simulations run on computers perform computations on hardware called CPUs, or central processing units. Increased parallelism can be obtained, however, by running certain portions of a computation on GPUs, or graphical processing units². The parallelism on a GPU is distributed in the following way: a GPU can launch a number of parallel processes called *blocks*. The collection of blocks launched on a GPU is called a *grid*. Within a block, a GPU can launch another set of parallel processes called *threads*. Figure B.1 displays a sample grid with two blocks where each block contains two threads.

¹It's worth noting that the data for this thesis was generated with a version of the GVFS which utilized MPI parallelism [126] but not GPU parallelism.

²Unless otherwise noted, the material from this section is based on [127].

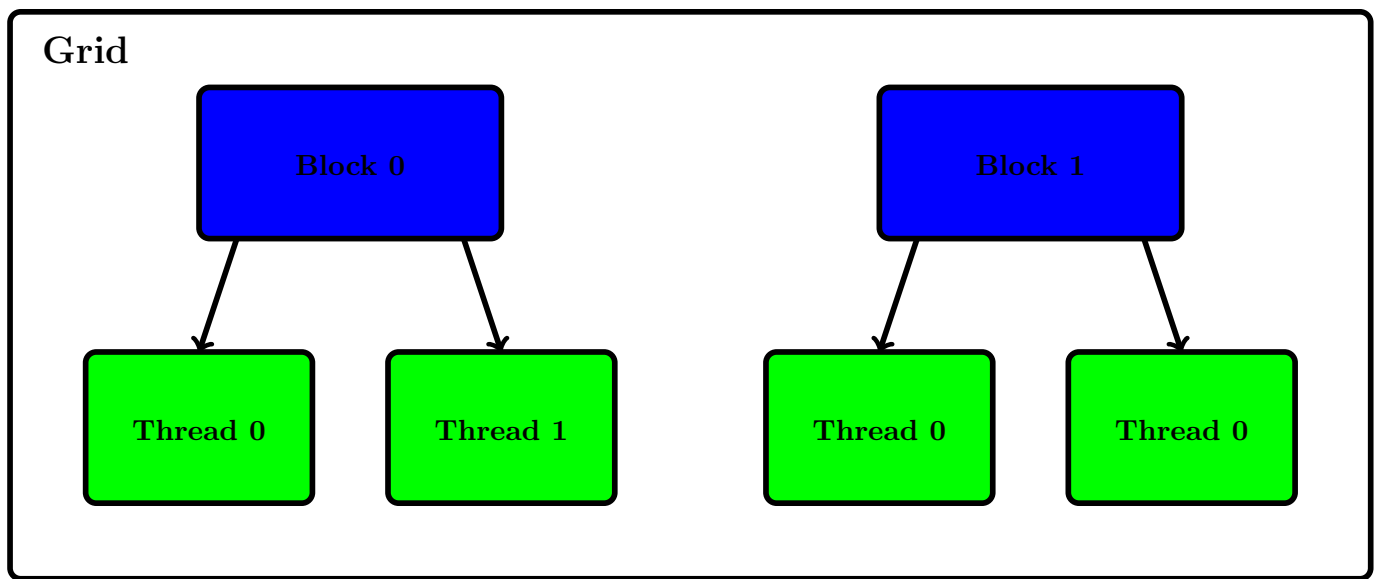


Figure B.1: Sample GPU grid containing two blocks where each block contains two threads

It is also important to note that a GPU is a separate piece of hardware. One company which manufactures GPUs is *NVIDIA*. *NVIDIA* GPUs utilize the *CUDA Architecture*. *NVIDIA* GPUs can be programmed in a language called *CUDA C*.

Because GPUs are a separate piece of hardware, there must be data transfers back and forth between the computer's memory and the GPU in order to use a GPU for scientific computing purposes. For the earlier versions of *CUDA*, data had to be first transferred from the computer's memory to the GPU. Then, parallel computations could be done on the GPU. Finally, the results of the computations had to be transferred from the GPU back to the computer's memory. Figure B.2 illustrates this process.

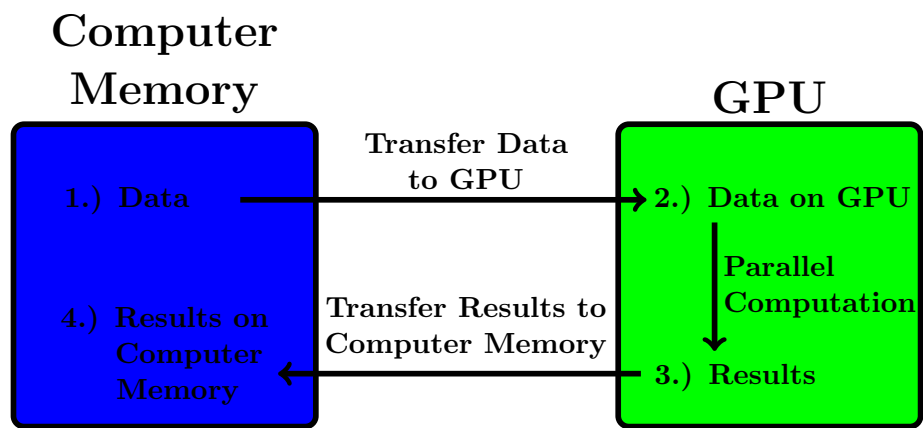


Figure B.2: Visualization of the data transfer process between the computer memory and the GPU utilized by the earlier versions of CUDA. The steps in this process are numbered 1.) - 4.).

A more recent version of CUDA simplifies this data transfer process for the programmer by making available a feature known as *Unified Memory* [128]. With Unified Memory it is possible to allocate an array such that changes to the elements of the array, if the changes occur on the GPU, are automatically updated on the computer's memory and vice versa. This helps to simplify CUDA programming. Figure B.3 illustrates the basic idea behind Unified Memory.

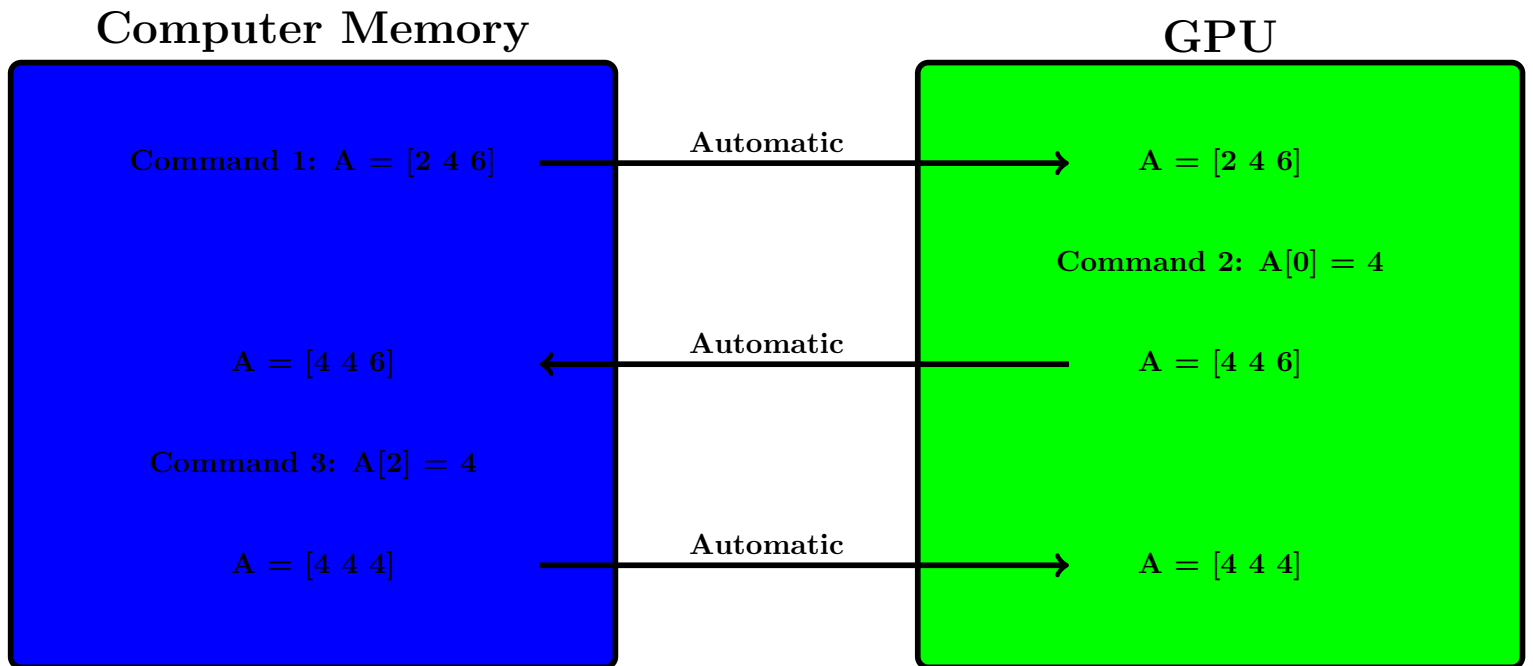


Figure B.3: Allocation and operations on an array, A , in unified memory. Changes to A on the GPU are automatically updated on the computer's memory and vice versa.

Bibliography

- [1] Fox, R. W., Pritchard, P. J., and McDonald, A. T., *Introduction to Fluid Mechanics*, John Wiley & Sons, Inc., Hoboken, NJ, 2009.
- [2] Rhie, C. M., and Chow, W. L., “Numerical Study of the Turbulent Flow Past an Airfoil with Trailing Edge Separation,” *AIAA Journal*, Vol. 21, 1983, pp. 1525-1532.
- [3] Sparrow, E. M., Abraham, J. P., and Minkowycz, W. J., “Flow Separation in a diverging conical duct: Effect of Reynolds number and divergence angle,” *International Journal of Heat and Mass Transfer*, Vol. 52, 2009, pp. 3079-3083.
- [4] Pelorson, X., Hirschberg, A., van Hassel, R. R., Wijnands, A. P. G., and Auregan, Y., “Theoretical and experimental study of quasisteady-flow separation within the glottis during phonation. Application to a modified two-mass model,” *The Journal of the Acoustical Society of America*, Vol. 96, 1994, pp. 3416-3431.
- [5] Schobeiri, M. T., Ozturk, B., Ashpis, D. E., “On the physics of flow separation along a low pressure turbine blade under unsteady flow conditions,” *Journal of Fluids Engineering*, Vol. 127, 2005, pp. 503-513.
- [6] Nakagawa, H., and Nezu, I., “Experimental investigation on turbulent structure of backward-facing step flow in an open channel,” *Journal of Hydraulic Research*, Vol. 25, 1987, pp. 67-88.
- [7] Xia, J., and Leung, D. Y. C., “Numerical Study on Flow over Buildings in Street Canyon,” *Journal of Environmental Engineering*, Vol. 127, 2001, pp. 369-376.

- [8] Bradshaw, P., and Wong, F. Y. F., “The reattachment and relaxation of a turbulent shear layer,” *Journal of Fluid Mechanics*, Vol. 52, Part 1, 1972, pp. 113-135.
- [9] Huang, H. T., and Fiedler, H. E., “A DPIV study of a starting flow downstream of a backward-facing step,” *Experiments in Fluids*, Vol. 23, 1997, pp. 395-404.
- [10] Kuehn, D. M., “Effects of Adverse Pressure Gradient on the Incompressible Reattaching Flow over a Rearward-Facing Step,” *AIAA Journal*, Vol. 18, No. 3, March 1980, pp. 343-344.
- [11] Spazzini, P. G., Iuso, G., Onorato, M., Zurlo, N., Di Cicca, G. M., “Unsteady behavior of back-facing step flow,” *Experiments in Fluids*, Vol. 30, 2001, pp. 551-561.
- [12] Hall, S. D., Behnia, M., Fletcher, C. A. J., Morrison, G. L., “Investigation of the secondary corner vortex in a benchmark turbulent backward-facing step using cross-correlation particle imaging velocimetry,” *Experiments in Fluids*, Vol. 35, 2003, pp. 139-151.
- [13] Le, H., Moin, P., and Kim, J., “Direct numerical simulation of turbulent flow over a backward-facing step,” *Journal of Fluid Mechanics*, Vol. 330, 1997, pp. 349-374.
- [14] Kim, J., Kline, S. J., Johnston, J. P., “Investigation of a Reattaching Turbulent Shear Layer: Flow Over a Backward-Facing Step,” *Journal of Fluids Engineering*, Vol. 102, 1980, pp. 302-308.
- [15] Eaton, J. K., “Turbulent Flow Reattachment: An Experimental Study of the Flow and Structure Behind a Backward-Facing Step,” Ph.D. dissertation, Department of Mechanical Engineering, Stanford University, 1980.
- [16] Barri, M., Khoury, G. K. El, Andersson, H. I., and Pettersen, B., “DNS of backward-facing step flow with fully turbulent inflow,” *International Journal for Numerical Methods in Fluids*, Vol. 64, 2010, pp. 777-792. doi:10.1002/flid.2176

- [17] Aider, Jean-Luc, and Danet, Alexandra, "Large-eddy simulation study of upstream boundary conditions influence upon a backward-facing step flow," *C. R. Mecanique*, Vol. 334, 2006, pp. 447-453.
- [18] Driver, D. M., Seegmiller, H. L., and Marvin, J. G., "Time-Dependent Behavior of a Reattaching Shear Layer," *AIAA Journal*, Vol. 25, 1987, pp. 914-919.
- [19] Roos, F. W., and Kegelman, J. T., "Control of Coherent Structures in Reattaching Laminar and Turbulent Shear Layers," *AIAA Journal*, Vol. 24, 1986, pp. 1956-1963.
- [20] Barkely, Dwight, Gomes, M. Gabriela M, and Henderson, Ronald D., "Three-dimensional instability in flow over a backward-facing step," *Journal of Fluid Mechanics*, Vol. 473, 2002, pp. 167-190.
- [21] Nadge, P. M., and Govardhan, R. N., "High Reynolds number flow over a backward-facing step: structure of the mean separation bubble," *Experiments in Fluids*, Vol. 55, Issue 1, 2014, Article 1657.
doi: 10.1007/s00348-013-1657-5
- [22] Jovic, S., and Driver, D., "Reynolds number effect on the skin friction in separated flows behind a backward-facing step," *Experiments in Fluids*, Vol. 18, 1995, pp. 464-467.
- [23] Westphal, R. V., and Johnston, J. P., "Effect of Initial Conditions on Turbulent Reattachment Downstream of a Backward-Facing Step," *AIAA Journal*, Vol. 22, No. 12, 1984, pp. 1727-1732.
- [24] Castro, I. P., and Bradshaw, P., "The turbulence structure of a highly curved mixing layer," *Journal of Fluid Mechanics*, Vol. 73, 1976, pp. 265-304.
- [25] Chandrsuda, C., Bradshaw, P., "Turbulence structure of a reattaching mixing layer," *Journal of Fluid Mechanics*, Vol. 110, 1981, pp. 171-194.
- [26] Eaton, J. K., and Johnston, J. P., "A Review of Research on Subsonic Turbulent Flow Reattachment," *AIAA Journal*, Vol. 19, 1981, pp. 1093-1100.

- [27] Adams, E. W., “Experiments on the Structure of Turbulent Reattaching Flows,” Ph.D. dissertation, Department of Mechanical Engineering, Stanford University, 1984.
- [28] Moffatt, M. K., “Viscous and resistive eddies near a sharp corner,” *Journal of Fluid Mechanics*, Vol. 18, 1964, pp. 1-18.
- [29] Yoo, J. Y., and Baik, S. J., “Redeveloping Turbulent Boundary Layer in the Backward-Facing Step Flow,” *Journal of Fluids Engineering*, Vol. 114, 1992, pp. 522-529.
- [30] Spalart, P. R., “Direct simulation of a turbulent boundary layer up to $Re_\theta = 1410$,” *Journal of Fluid Mechanics*, Vol. 187, 1988, pp. 61-98.
- [31] Bernard, P. S., and Wallace, J. M., *Turbulent Flow: Analysis, Measurement, and Prediction*, Wiley, Hoboken, NJ, 2002.
- [32] Coles, D. E., “The law of the wake in the turbulent boundary layer,” *Journal of Fluid Mechanics*, Vol. 1, 1956, pp. 191-226.
- [33] Kundu, P. K., Cohen, I. M., and Dowling, D. R., *Fluid Mechanics*, Elsevier, Waltham, MA, Fifth Edition, 2012.
- [34] Nagib, H., and Hites, M., “High Reynolds Number Boundary-Layer Measurements in the NDF,” *AIAA Paper 95-0786*, 1995.
- [35] Wu, X., and Moin, P., “Direct numerical simulation of turbulence in a nominally zero-pressure-gradient flat-plate boundary layer,” *Journal of Fluid Mechanics*, Vol. 630, 2009, pp. 5-41.
- [36] Schlatter, P., and Orlu, R., “Assessment of direct numerical simulation data of turbulent boundary layers,” *Journal of Fluid Mechanics*, Vol. 659, 2010, pp. 116-126.
- [37] Adrian, R. J., “Hairpin vortex organization in wall turbulence,” *Physics of Fluids*, Vol. 19, 2007.
doi: 10.1063/1.2717527
- [38] Kline, S. J., Reynolds, W. C., Schraub, F. A., and Runstadler, P. W., “The structure of turbulent boundary layers,” *Journal of Fluid Mechanics*, Vol. 30, 1967, pp. 741-773.

- [39] Kim, H. T., Kline, S. J., and Reynolds, W. C., “The production of turbulence near a smooth wall in a turbulent boundary layer,” *Journal of Fluid Mechanics*, Vol. 50, 1971, pp. 133-160.
- [40] Adrian, R. J., Meinhart, C. D., and Tomkins, C. D., “Vortex organization in the outer region of the turbulent boundary layer,” *Journal of Fluid Mechanics*, Vol. 422, 2000, pp. 1-54.
- [41] Tardu, S., “Characteristics of single and clusters of bursting events in the inner layer,” *Experiments in Fluids*, Vol. 20, 1995, pp. 112-124.
- [42] Corino, E. R., and Brodkey, R. S., “A visual investigation of the wall region in turbulent flow,” *Journal of Fluid Mechanics*, Vol. 37, 1969, pp. 1-30.
- [43] Zhou, J., Adrian, R. J., and Balachandar, S., “Autogeneration of near-wall vortical structures in channel flow,” *Physics of Fluids*, Vol. 8, 1996.
- [44] Zhou, J., Adrian, R. J., Balachandar, S., and Kendall, T. M., “Mechanisms for generating coherent packets of hairpin vortices in channel flow,” *Journal of Fluid Mechanics*, Vol. 387, 1999, pp. 353-396.
- [45] Smits, A. J., McKeon, B. J., Marusic, I., “High-Reynolds Number Wall Turbulence,” *Annual Review of Fluid Mechanics*, Vol. 43, 2011, pp. 353-375.
doi: 10.1146/annurev-fluid-122109-160753
- [46] Hutchins, N., and Marusic, I., “Evidence of very long meandering features in the logarithmic region of turbulent boundary layers,” *Journal of Fluid Mechanics*, Vol. 579, 2007, pp. 1-28.
doi: 10.1017/S0022112006003946
- [47] Clauser, F. H., “Turbulent boundary layers in adverse pressure gradients,” *Journal of the Aeronautical Sciences*, Vol. 21, 1954, pp. 91-108.
- [48] Castillo, L., and George, W. K., “Boundary Layers with Pressure Gradient: Similarity of the Velocity Deficit,” *38th Aerospace Sciences Meeting & Exhibit*, AIAA 2000-0913, January 2000.
- [49] Castillo, L., and George, W. K., “Similarity Analysis for Turbulent Boundary Layer with Pressure Gradient: Outer Flow,” *AIAA Journal*, Vol. 39, 2001, pp. 41-47.

- [50] Lee, J. H., and Sung, H. J., “Effects of an adverse pressure gradient on a turbulent boundary layer,” *International Journal of Heat and Fluid Flow*, Vol. 29, 2008, pp. 568-578.
- [51] Zagarola, M. V., and Smits, A. J., “Mean-flow scaling of turbulent pipe flow,” *Journal of Fluid Mechanics*, Vol. 373, 1998, pp. 33-79.
- [52] Nagano, Y., Tagawa, M., and Tsuji, T., “Effects of adverse pressure gradients on mean flows and turbulence statistics in a boundary layer,” *Turbulent shear flows: selected papers from the ... International Symposium on Turbulent Shear Flows*, Vol. 8, 1993, pp. 7-21.
- [53] Houra, T., Tsuji, T., and Nagano, Y., “Effects of adverse pressure gradient on quasi-coherent structures in turbulent boundary layer,” *International Journal of Heat and Fluid Flow*, Vol. 21, 2000, pp. 304-311.
- [54] Krogstad, P. A., and Skare, P. E., “Influence of a strong adverse pressure gradient on the turbulent structure in a boundary layer,” *Physics of Fluids*, Vol. 7, 1995.
- [55] Lee, J. H., and Sung, H. J., “Structures in turbulent boundary layers subjected to adverse pressure gradients,” *Journal of Fluid Mechanics*, Vol. 639, 2009, pp. 101-131.
- [56] Nagano, Y., Tsuji, T., and Houra, T., “Structure of turbulent boundary layer subjected to adverse pressure gradient,” *International Journal of Heat and Fluid Flow*, Vol. 19, 1998, pp. 563-572.
- [57] Bell, J. H., and Mehta, R. D., “Development of a Two-Stream Mixing Layer from Tripped and Untripped Boundary Layers,” *AIAA Journal*, Vol. 28, 1990, pp. 2034-2042.
- [58] Rogers, M. M., and Moser, R. D., “Direct simulation of a self-similar turbulent mixing layer,” *Physics of Fluids*, Vol. 6, 1994, pp. 903-923.
- [59] Winant, C. D., and Browand, F. K., “Vortex pairing: the mechanism of turbulent mixing-layer growth at moderate Reynolds number,” *Journal of Fluid Mechanics*, Vol. 63, 1974, pp. 237-255.

- [60] Bernard, P. S., “Grid-Free Simulation of the Spatially Growing Turbulent Mixing Layer,” *AIAA Journal*, Vol. 46, 2008, pp. 1725-1737.
- [61] Puckett, E. G., “Vortex Methods: An Introduction and Survey of Selected Research Topics,” *Incompressible computational fluid dynamics-Trends and advances*, Cambridge, United Kingdom and New York, Cambridge University Press, 1993, pp. 335-407.
- [62] Bernard, P. S., Collins, P., and Potts, M., “Vortex Filament Simulation of the Turbulent Boundary Layer,” *AIAA Journal*, Vol. 48, 2010, pp. 1757-1771.
- [63] Bernard, P. S., “Vortex Dynamics in Transitional and Turbulent Boundary Layers,” *AIAA Journal*, Vol. 51, 2013, pp. 1828-1842.
- [64] Bernard, P. S., “Boundary Layer Vorticity and the Rise of “Hairpins””, *Progress in Wall Turbulence: Understanding and Modelling*, 18-20 June 2014, Lille, France.
- [65] Buffat, M., Le Penven, L., Cadiou, A., and Montagnier, J., “DNS of bypass transition in entrance channel flow induced by boundary layer interaction,” *European Journal of Mechanics B/Fluids*, Vol. 43, 2014, pp. 1-13.
- [66] Bernard, P. S., “The hairpin vortex illusion,” *Journal of Physics: Conference Series*, Vol. 318, 2011.
- [67] Vaughan, N. J., and Zaki, T. A., “Stability of zero-pressure-gradient boundary layer distorted by unsteady Klebanoff streaks,” *Journal of Fluid Mechanics*, Vol. 681, 2011, pp. 116-153.
- [68] Tani, I., “Boundary-Layer Transition,” *Annual Review of Fluid Mechanics*, Vol. 1, 1969, pp. 169-196.
- [69] Jacobs, R. G., and Durbin, P. A., “Simulations of bypass transition,” *Journal of Fluid Mechanics*, Vol. 428, 2001, pp. 185-212.
- [70] Bake, S., Meyer, D. G. W., and Rist, U., “Turbulence mechanism in Klebanoff transition: a quantitative comparison of experiment and direct numerical simulation,” *Journal of Fluid Mechanics*, Vol. 459, 2002, pp. 217-243.

- [71] Yang, D. D., and Qiang, W. S., “Direct numerical simulation of turbulent flow over backward-facing at high Reynolds numbers,” *Science China Technological Sciences*, Vol. 55, 2012, pp. 3213-3222.
- [72] Sethian, J. A., and Ghoniem, A. F., “Validation Study of Vortex Methods,” *Journal of Computational Physics*, Vol. 74, 1988, pp. 283-317.
- [73] Ghoniem, A. F., and Cagnon, Y., “Vortex Simulation of Laminar Recirculating Flow,” *Journal of Computational Physics*, Vol. 68, 1987, pp. 346-377.
- [74] Gagnon, Y., Giovannini, A., and Hebrard, P., “Numerical simulation and physical analysis of high Reynolds number recirculating flows behind sudden expansions,” *Physics of Fluids*, Vol. 5, 1993, pp. 2377-2389.
- [75] Head, M. R., and Bandyopadhyay, P., “New Aspects of turbulent boundary-layer structure,” *Journal of Fluid Mechanics*, Vol. 107, 1981, pp. 297-338.
- [76] Kitzhofer, J., Brucker, C., Pust, O., and Nonn, T., “Volumetric Measurement of the Transitional Backward Facing Step Flow,” *9th International Symposium on Particle Image Velocimetry*, Kobe, Japan, July 21-23, 2011.
- [77] Biswas, G., Breuer, M., and Durst, F., “Backward-Facing Step Flows for Various Expansion Ratios at Low and Moderate Reynolds Numbers”, *Journal of Fluids Engineering*, Vol. 126, 2004, pp. 362-374.
- [78] Yoshioka, S., Obi, S., Masuda, S., “Turbulence statistics of periodically perturbed separated flow over backward-facing step,” *International Journal of Heat and Fluid Flow*, Vol. 22, 2001, pp. 393-401.
- [79] Tihon, J., Legrand, J., and Lengenthalhomme, P., “Near-wall investigation of backward-facing step flows,” *Experiments in Fluids*, Vol. 31, 2001, pp. 484-493.
- [80] Otugen, M. V., “Expansion ratio effects on the separated shear layer and reattachment downstream of a backward-facing step,” *Experiments in Fluids*, Vol. 10, 1991, pp. 273-280.

- [81] Kasagi, N., and Matsunaga, A., “Three-dimensional particle-tracking velocimetry measurement of turbulence statistics and energy budget in a backward-facing step flow,” *International Journal and Heat and Fluid Flow*, Vol. 16, 1995, pp. 477-485.
- [82] Chun, K. B., and Sung, H. J., “Control of turbulent separated flow over a backward-facing step by local forcing,” *Experiments in Fluids*, Vol. 21, 1996, pp. 417-426.
- [83] Kostas, J., Soria, J., and Chong, M. S., “Particle image velocimetry measurements of a backward-facing step flow,” *Experiments in Fluids*, Vol. 33, 2002, pp. 838-853.
doi: 10.1007/s00348-002-0521-9
- [84] Kang, S., and Choi, H., “Suboptimal feedback control of turbulent flow over a backward-facing step,” *Journal of Fluid Mechanics*, Vol. 463, 2002, pp. 201-227.
- [85] Armaly, B. F., Durst, F., Pereira, J. C. F., and Schonung, B., “Experimental and theoretical investigation of backward-facing step flow,” *Journal of Fluid Mechanics*, Vol. 127, 1983, pp. 473-496.
- [86] Friedrich, R., and Arnal, M., “Analysing Turbulent Backward-Facing Step Flow with the Lowpass-Filtered Navier-Stokes Equations,” *Journal of Wind Engineering and Industrial Aerodynamics*, Vol. 35, 1990, pp. 101-128.
- [87] Kaiktsis, L., Karniadakis, G. E., and Orszag, S. A., “Onset of three-dimensionality, equilibria, and early transition in flow over a backward-facing step,” *Journal of Fluid Mechanics*, Vol. 231, 1991, pp. 501-528.
- [88] Adrian, R. J., and Liu, Z. C., “Observation of Vortex Packets in Direct Numerical Simulation of Fully Turbulent Channel Flow,” *Journal of Visualization*, Vol. 5, 2002, pp. 9-19.
- [89] Thangam, S., and Speziale, C. G., “Turbulent Flow Past a Backward-Facing Step: A Critical Evaluation of Two-Equation Models,” *AIAA Journal*, Vol. 30, No. 5, 1992, pp. 1314-1320.
- [90] Park, T. S., and Sung, H. J., “A nonlinear low-Reynolds-number $k - \epsilon$ model for turbulent separated and reattaching flows - I. Flow field

- computations,” *International Journal of Heat and Mass Transfer*, Vol. 38, No. 14, 1995, pp. 2657-2666.
- [91] Abe, K., Kondoh, T., and Nagano, Y., “A new turbulence model for predicting fluid flow and heat transfer in separating and reattaching flows - I. Flow Field Calculations,” *International Journal of Heat and Mass Transfer*, Vol. 37, No. 1, 1994, pp. 139-151.
- [92] Shih, T., Liou, W. W., Shabbir, A., Yang, Z., and Zhu, J., “A new $k - \epsilon$ eddy viscosity model for high reynolds number turbulent flows,” *Computers & Fluids*, Vol. 24, No. 3, 1995, pp. 227-238.
- [93] Lan, H., Armaly, B. F., and Drallmeier, J. A., “Three-dimensional simulation of turbulent forced convection in a duct with backward-facing step,” *International Journal of Heat and Mass Transfer*, Vol. 52, 2009, pp. 1690-1700.
- [94] Silveira Neto, A., Grand, D., Metais, O., and Lesieur, M., “A numerical investigation of the coherent vortices in turbulence behind a backward-facing step,” *Journal of Fluid Mechanics*, Vol. 256, 1993, pp. 1-25.
- [95] Hudy, L. M., Naguib, A., and Humphreys, W. M., “Stochastic estimation of a separated-flow field using wall-pressure-array measurements,” *Physics of Fluids*, Vol. 19, 2007.
doi: 10.1063/1.2472507
- [96] Scarano, F., Benocci, C., and Riethmuller, M. L., “Pattern recognition analysis of the turbulent flow past a backward facing step,” *Physics of Fluids*, Vol. 11, 1999.
doi: 10.1063/1.870240
- [97] Schram, C., Rambaud, P., and Riethmuller, M. L., “Wavelet based eddy structure eduction from a backward facing step flow investigated using particle image velocimetry,” *Experiments in Fluids*, Vol. 36, 2004, pp. 233-245.
- [98] Jeong, J., and Hussain, F., “On the identification of a vortex,” *Journal of Fluid Mechanics*, Vol. 285, 1995, pp. 69-94.

- [99] Robinson, S. K., Kline, S. J., and Spalart, P. R., “A Review of Quasi-Coherent Structures in a Numerically Simulated Turbulent Boundary Layer,” *NASA Technical Memorandum 102191*, 1989.
- [100] Robinson, S. K., “Coherent Motions in the Turbulent Boundary Layer,” *Annual Review of Fluid Mechanics*, Vol. 23, 1991, pp. 601-639.
- [101] Adrian, R. J., Christensen, K. T., and Liu, Z.-C., “Analysis and interpretation of instantaneous turbulent velocity fields,” *Experiments in Fluids*, Vol. 29, 2000, pp. 275-290.
- [102] Le, H., “Direct Numerical Simulation of Turbulent Flow Over a Backward-Facing Step,” Ph.D. dissertation, Department of Mechanical Engineering, Stanford University, 1995.
- [103] Christensen, K. T., and Adrian, R. J., “Statistical evidence of hairpin vortex packets in wall turbulence,” *Journal of Fluid Mechanics*, Vol. 431, 2001, pp. 433-443.
- [104] Willmarth, W. W., and Lu, S. S., “Structure of the Reynolds stress near the wall,” *Journal of Fluid Mechanics*, Vol. 55, 1972, pp. 65-92.
- [105] Monty, J. P., Harun, Z., and Marusic, I., “A parametric study of adverse pressure gradient turbulent boundary layers,” *International Journal of Heat and Fluid Flow*, Vol. 32, 2011, pp. 575-585.
- [106] Rani, H. P., Sheu, T. W. H., and Tsai, E. S. F., “Eddy structures in a transitional backward-facing step flow,” *Journal of Fluid Mechanics*, Vol. 588, 2007, pp. 43-58.
- [107] Bernard, P. S., *Fluid Dynamics*, Cambridge University Press, New York, NY, 2015.
- [108] Hess, J. L., and Smith, A. M. O., “Calculation of Potential Flow About Arbitrary Bodies,” *Progress in Aeronautical Sciences*, Vol. 8, 1967, pp. 1-138.
- [109] Saad, Y., and Schultz, M. H., “GMRES: A Generalized Minimal Residual Algorithm For Solving Nonsymmetric Linear Systems,” *SIAM Journal on Scientific and Statistical Computing*, Vol. 7, 1986, pp. 856-869.

- [110] Strickland, J. H., and Baty, R. S., “A Three-Dimensional Fast Solver for Arbitrary Vorton Distributions,” Sandia National Lab, Rept. SAND93-1641, Albuquerque, NM, 1994.
- [111] Greengard, L., and Rokhlin, V., “A Fast Algorithm for Particle Simulations,” *Journal of Computational Physics*, Vol. 73, 1987, pp. 325-348.
- [112] Bernard, P. S., “Vortex filament simulation of the turbulent coflowing jet,” *Physics of Fluids*, Vol. 21, 2009.
- [113] Chorin, A. J., “Hairpin Removal in Vortex Interactions II,” *Journal of Computational Physics*, Vol. 107, 1993, pp. 1-9.
- [114] Bernard, P. S., “Turbulent flow properties of large-scale vortex systems,” *Proceedings of the National Academy of Sciences of the United States of America*, Vol. 103, 2006, pp. 10174-10179.
- [115] Lomax, H., Pulliam, T. H., and Zingg, D. W., *Fundamentals of Computational Fluid Dynamics*, Springer, 2003.
- [116] Moin, P., “Numerical and Physical Issues in Large Eddy Simulation of Turbulent Flows,” *JSME International Journal, Series B (Fluids and Thermal Engineering)*, Vol. 41, 1998, pp. 454-463.
- [117] Beaudan, P., and Moin, P., “Numerical Experiments on the Flow Past a Circular Cylinder at Sub-Critical Reynolds Number,” Ph.D. dissertation, Department of Mechanical Engineering, Stanford University, 1994.
- [118] Carrier, G. F., and Pearson, C. E., *Partial Differential Equations Theory and Technique*, Academic Press, Inc., New York, New York, 1976.
- [119] Williamson, C. H. K., “Vortex Dynamics in the Cylinder Wake,” *Annual Review of Fluid Mechanics*, Vol. 28, 1996, pp. 477-539.
- [120] Roshko, A., “Experiments on the flow past a circular cylinder at very high Reynolds number,” *Journal of Fluid Mechanics*, Vol. 10, 1961, pp. 345-356.
- [121] Bruno, L., Fransos, D., Coste, N., and Bosco, A., “3D Flow around a rectangular cylinder: A computational study,” *Journal of Wind Engineering and Industrial Aerodynamics*, Vol. 98, 2010, pp. 263-276.

- [122] Okajima, A., “Strouhal numbers of rectangular cylinders,” *Journal of Fluid Mechanics*, Vol. 123, 1982, pp. 379-398.
- [123] Bernard, P. S., 2015 Vortex Loop Formation. Private Communication, Professor of Mechanical Engineering, University of Maryland, College Park, MD.
- [124] Batchelor, G., K., *An Introduction to Fluid Dynamics*, Cambridge University Press, New York, 1967.
- [125] Sommerfeld, A., *Mechanics of Deformable Bodies Lectures on Theoretical Physics, Vol. II*, Academic Press, Inc., New York, 1950.
- [126] Pacheco, P. S., *An Introduction to Parallel Programming*, Elsevier.
- [127] Sanders, J., and Kandrot, E., *CUDA By Example An Introduction to General-Purpose GPU Programming*, Pearson Education, Inc., Boston, MA, 2011.
- [128] Harris, M., *Unified Memory in CUDA 6*, <https://devblogs.nvidia.com/parallelforall/unified-memory-in-cuda-6/>, Nov. 18, 2013.
- [129] Bernal, L. P., and Roshko, A., “Streamwise vortex structure in plane mixing layers,” *Journal of Fluid Mechanics*, Vol. 170, 1986, pp. 499-525.
- [130] Wackerly, D. D., Mendenhall III, W., and Scheaffer, R. L., *Mathematical Statistics with Applications*, Duxbury, Pacific Grove, CA, Sixth Edition, 2002.
- [131] Chorin, A. J., *Vorticity and Turbulence*, Springer-Verlag, New York, NY, 1994.
- [132] Bryant, R. E., and O’Hallaron, D. R., *Computer Systems A Programmer’s Perspective*, Prentice Hall, 2011.
- [133] Choi, H., Lee, J., and Park, H., “Aerodynamics of Heavy Vehicles,” *Annual Review of Fluid Mechanics*, Vol. 46, 2014, pp. 441-468.

- [134] Thacker, A., Aubrun, S., Leroy, A., and Devinant, P., “Effects of suppressing the 3D separation on the rear slant on the flow structures around an Ahmed body,” *Journal of Wind Engineering and Industrial Aerodynamics*, Vol. 107-108, 2012, pp. 237-243.